Study of vortex-induced vibrations in off-shore structures

Von der Fakultät für Ingenieurwissenschaften, Abteilung Maschinenbau und Verfahrenstechnik
der
Universität Duisburg-Essen
zur Erlangung des akademischen Grades

eines

Doktors der Ingenieurwissenschaften

Dr.-Ing.

genehmigte Dissertation

von

Mohammed Abdulaziz

aus

Ägypten

Gutachter: Univ.-Prof. Dr.-Ing. Betar Ould el Moctar
Univ.-Prof. Dr.-Ing. Wojciech Kowalczyk

Tag der mündlichen Prüfung: 20.03.2017

Study of the vortex-induced vibrations in off-shore structures

By
Mohammed Abdulaziz

Submitted to Institute of Ship Technology, Ocean Engineering and Transport Systems (ISMT) in partial fulfillment of the requirements for the degree of
Doctor of Philosophy

at the UNIVERSITY OF DUISBURG-ESSEN

Supervisor: Univ. Prof. Dr. –Ing. Bettar Ould el Moctar
Co-supervisor: Univ. Prof. Dr. –Ing. Wojciech Kowalczyk

Acknowledgments

This doctoral thesis is my performed task as a doctoral student at the Institute of Ship Technology, Ocean Engineering and Transport Systems (ISMT) at the university of Duisburg-Essen, Duisburg, Germany.
I would like to introduce my thanks to my supervisor Mr. Prof. Dr. –Ing Bettar Ould el Moctar for continual encouragement and patient guidance throughout the course of this work.

Abstract

The flow around different geometric obstacles is a challenging research topic. The continual change of flow separation points positions on the obstacle surface generates the vortices in downstream flow within a phenomenon called vortex shedding, which was originally discussed by Mr. von Kármán. Because of this continuous relocation of separation points on the obstacle surface, both the pressure and forces differ in an unstable scenario on the obstacle surface. The occurrence of oscillations or so-called vortex-induced vibrations in obstacle therefore takes place. These vortex-induced vibrations may cause real disasters. A well-known example is the Tacoma Narrows Bridge –USA in 1940. Important applications can be found in many parts of the off-shore structures. This dissertation is giving a deep understanding of the phenomenon by simulating different study cases as well as presenting solutions for reducing the effect of it in deep water risers. The dissertation is presenting a numerical tool as well, which is able to predict computationally the behavior of the deep water risers under the mentioned phenomenon. A coupling between a fluid dynamics solver and a structural dynamics solver has been presented based on the available OpenFOAM libraries. A number of fundamental cases had been simulated in the present dissertation for the purpose of validation and deep understanding, while the related theory has also been discussed. The presented solver as well as the design solutions is supposed to be a milestone in an in-depth research regarding this field of deep water risers and off-shore structures. The results of this work may provide more understanding of the presented problems and opened new doors for future work.

Keywords: vortex-induced vibrations, offshore structures, OpenFOAM, strong coupling, fluid-structure interaction, computational fluid dynamics, finite volume method, VIV suppression.

Contents

List of Figures

List of Tables

Abbreviations

CFD — Computational Fluid Dynamics
DNS — Direct Numerical Simulation
FEM — Finite Element Method
FSI — Fluid-Structure Interaction
FIV — Flow-Induced Vibrations
LDV — Laser Doppler Velocimetry
LES — Large Eddy Simulation
OF — OpenFOAM open source software
PIV — Particle Image Velocimetry
RANS — Reynold Averaged Navier-Stocks turbulence model
Re — Reynolds Number
St — Strouhal Number
VIV — Vortex-Induced Vibrations
VR — Velocity Ratio

Chapter 1

Introduction

1.1 Motivation

The phenomenon of vortex-induced vibrations as well as the vortex flow behind an obstacle has been discussed in many research articles from both physical and mathematical views. In the last years the effect of the vortex-induced vibrations on the offshore structures has been considered for a deep understanding. Furthermore, suppression of the evidence of it in deep water risers has been deeply studied.
The prediction of the offshore structures vibrations behavior under the effect of a vortex flow is a challenging topic of research. The experimental prediction is running on time and high cost. As an alternative solution to the costly experimental techniques, numerical prediction tools have been presented. The commercial software are not flexible enough to have several methodes of modelings and therefore make the study of such phenomenon expensive and even not precise. Unlike commercial software, the open-source numerical tools are being presented as a reliable solution especially in research institutes.
As a multi-physics case, the vortex-induced vibrations in offshore structures are studied. The coupling between solid and fluid solvers in an open-source tool is a motivated topic of research.
The following literature review shows that the environmental conditions had mostly not been considered in a good numerical modeling. Most of the presented numerical tools are either tested at laboratory conditions, or were developed not to carry out the real cases under their environmental condi-

tions.
In the reference [35], the researchers performed very robust simulations. The numerical studies in this reference did not present any further help for the reader other than results. From the author's point of view the reference was focused on presenting results and was not helpful.
A helpful start has been presented in the reference [48] for implementing a reliable fluid-structure interaction using an OpenFOAM solver. The reference unfortunately did not include a solver, which can simulate a wide range of real cases.
The experimental research works as [8], [26], [27] and [33] provided a motivation for presenting a numerical tool is able to reduce the experimental efforts and give results with a high dependability and accuracy. Many published research works showed the difficulty of such fundamental experiments.
As mentioned above, the topic of research is important for the field of oil and gas deep water drilling risers as an industrial case. The numerical investigation, as one of prediction methods, has a high potential for being carried out. The advantages of the numerical investigation could be regarded as low cast, time and effort. Furthermore, the numerical investigation can provide more details which are not able to be observed or measured during the laboratory experiments.
OpenFOAM, as an open-source computational mechanics C++ toolbox, gives the chance for researchers to achieve in-depth investigations with reduced efforts and high reliability.
Beside working on understanding the vortex-induced vibrations phenomenon and giving a design solution for the suppression of the resulted vibrations, a reliable numerical prediction tool based on OpenFOAM C++ library has been presented. The presented tool is able to simulate industrial cases and has a high availability and usability. Furthermore, the validation and verification of the presented tool under the enviromental conditions, e.g. high Reynolds number, as well as using it in further investigation and finding solutions are found in the scope of the present work.
The goal of presenting the mentioned computational prediction tool, is the usage of it for testing a vortex-induced vibration suppression device. Finding a practical solution and presenting a suppression device have a high motivation as a practical contribution of the present work.

1.2 Background

The research topic is focused on studying the vortex-induced vibrations in offshore structures by using a numerical simulation tool developed based on OpenFOAM library. The present work therefore presents a number of numerical simulations, a description of the presented tool and its validation as well as introducing a vortex-induce vibrations suppression device as a design solution.
Since deep water structures are subjected to the ocean cross flows, the vortex flow phenomenon takes place. This physical phenomenon results in a change of the forces acting on the structure surfaces. This temporal change of the values and direction of these forces produces a vibration in the deep water structures. In most of the cases, these vibrations are extremely harmful and can cause structure failure.
The underwater part of the offshore structures affects the whole performance of a wide range of large-scale projects, e.g. the oil and gas rigs in deep water. The topic therefore is the subject of extensive research and development. The vortex-induced vibrations play a vital role in the design of offshore structures as well.
The world has witnessed many environmental disasters in the last few years due to cracks in oil pipe lines or drilling risers, caused by vortex-induced vibrations in a long term. Through development and research, oil production firms are motivated to avoid any future problems regarding the present topic. This point of research therefore has a strong motivation to be studied in-depth in the present dissertation.
As mentioned, the numerical studies and simulations form the main part of the present dissertation. Moreover, simulations of a number of experimental cases are taken into regard for validation and extensive understanding. The presented numerical results are compared to experimental ones for the propose of validating and verifying the presented numerical tool.
The vortex-induced vibration (VIV) cases in offshore structures are complex and are not completely understood, particularly in high Reynolds number flows [1]. The present work therefore contributes to the deeper understanding of the topic and presents a reliable tool that has been developed on a mathematical and physical modeling that appropriates to environmental conditions.

1.3 Previous works review

The formation and dynamics of vortex is a very broad scientific topic which is still being studied. Many studies have been made concerning flow around obstacles and the formation of a vortex street or so-called "von Karman vortex street", and these will be discussed in this section. Furthermore, many research topics about the vortex-induced vibrations are taken into regard. The covered topics include vortex formation, fluid-structure interaction in vortex-induced vibrations, vortex-wave interaction and other important topics which are related or have some useful relationship to the present dissertation research topic. This section brought the best knowledge to the author. The review is presented in the form of one-reference-paragraphs to make the literature accessible to the reader. It gives the best knowledge to the author in order to be able to determine the main goals on which the dissertation will be based, as presented in the furthur sections.

The unsteady separation of the fluid flow boundary layer on both sides of obstacle, which are perpendicular to the flow direction, is the main concept of vortex formation in downstream[2]. Durgin and Karlsson have discussed the phenomenon of vortex street breakdown[3], as well as studying vortex formation and the von Karman vortex-street in-depth. They worked on experimental observations of vortex formation by placing a cylinder perpendicular to air flow in two different squire wind tunnels and studying the flow in downstream. Durgin and Karlsson observed that in the case of a large cylinder (0.114 m diameter at 4.85 m/s), the vortex filaments curve around the cylinder and because of the virtue of main flow, the vortex filaments are stretched. Their important observation of the flow in downstream was that the vortices grow closer together as they travel downstream due to the slowing down of the main flow. The observations of Durgin and Karlsson of vortex street formation in downstream provide more understanding of the frequency behavior in downstream. Using the Hamel-Oseen vortex equation, they showed that the vortex shape in downstream will in general be converted into an ellipse, which they also observed experimentally.

Cenedese et al. [6] worked on the analysis of wake behind a cylinder and airfoil in a water tunnel using a laser Doppler velocimeter (LDV) connected to a real-time spectrum analyzer. The airfoil was tested in the range of Reynolds numbers between 4000 and 12000 for various incidence angles. The results of Cenedese gave a good representation of the relationship between Reynolds, Strouhal and Roshko numbers. The results showed that the relationship be-

tween Roshko and Reynolds numbers are linear in the case of constant airfoil at a constant angle. Moreover, he provided a good understanding regarding the behavior of Roshko number versus incidence angle, which is placed side by side with the results of cylinder to give a complete consideration of such cases.
Basdevant et al. [7] worked on an interesting topic – the coupling between vortices in downstream. the so-called vortex couples were studied through laboratory observations. It was observed that by increasing flow Reynold's number, the coupling becomes more observable. The flow in downstream behind the obstacle forms a regular Karmann vortex street, allowing the vortex coupling to be observed, after which the so-called vortex escaping could be seen. In addition to the good visualization of vortex coupling in downstream, Basdevant et al. described the coupling by some correlation of vorticity, stream function and velocity of coupling.

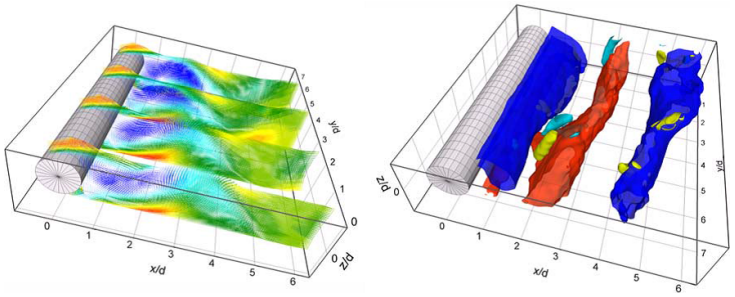

Figure 1.1: [8]:Instantaneous velocity and vorticity fields at Re = 180

Scarano et al.[8] studied the 3D patterns of vorticity in cylinder wake using time-resolved tomographic particle image velocimetry at Reynolds numbers ranging from 180 to 5540. The time-resolved measurements were done at Re=180, 360 and 540, whereas the transitional (Re = 1080) and turbulent regimes (Re = 5540) were investigated by snapshots separated in phase by more than $\pi/4$. The results, achieved using the tomographic PIV technique, provide an excellent visualization of vortex in cylinder wake flow. As shown in the figures, the results were numerically treated to provide more understanding.
Koh [9] worked mathematically on the relationship between the viscous dissipation and the vorticity in incompressible fluids. He formed his mathematical model and derived some equations to establish the relationship between the vorticity and viscosity of an incompressible fluid. The change in fluid

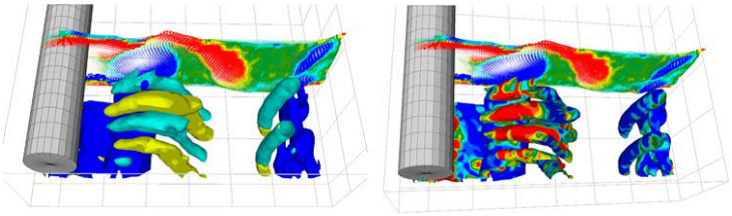

Figure 1.2: [8]: Detail of counter-rotating vortex pairs at Re = 360.

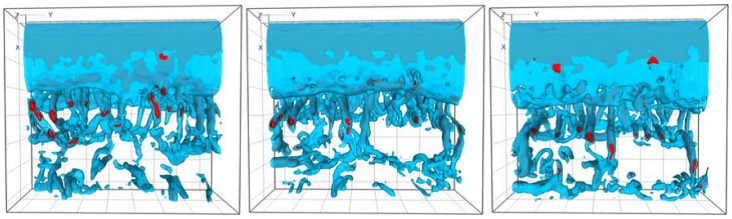

Figure 1.3: [8] Instantaneous vorticity fields at Re = 1080.

kinematic energy is modeled in order to find a right expression of energy dissipation due to viscosity in the case of vorticity. Using his equations, he found a good mathematical representation of viscous dissipation in flow field induced by vortices. Depending on his references, the irrotationality does not mean that the fluid flow is free-vortex. Koh proved mathematically that no-slip condition at boundary can cause so-called free-vortex potential fluid flow. He also discussed the conditions under which the no-slip could be considered.

Lee [10] used a two-step computational method for studying the vortex-induced vibrations of a bridge. Lee considered two- and three-dimensional models of bridge structure under unsteady wind loads to present his proposed method for studying the fluid dynamics and vortex-induced vibrations. Lee's work was focused on bridge structures, which are not relevant to this dissertation but in this section the method which was used will be noted because of its ability to solve vortex-induced vibrations cases. According to his references, Lee had taken one assumption into account, which is that the vortex-induced vibrations of a structure do not significantly modify the fluid flow around it, since the vibration's amplitude is less than 10% of the structure size. Lee used two commercial software products in order to analyze both fluid and structural domains and couple the results between both of them. ALE was not used in his work because of its inability to give better results in such

cases. Lee used the 2D model to calculate the fluid flow domain and the 3D model to calculate the dynamic response of structure using the output results obtained from CFD analysis. Lee's results gave a good representation and more understanding of coupling and FSI calculations in the case of vortex-induced vibrations.

Skaugset et al. [11] tried to reduce the amplitude of vortex-induced vibrations of a cylinder in water by adding water jets on the cylinder side. They obtained the results by using a direct numerical simulation (DNS) code created by them. Moreover, they carried out experimental work in order to validate their work of numerical simulation. The idea of jets has been discussed in many papers starting from Prandlt 1904 right up to the present paper of Skaugest et al., which worked on altering both the 2D effect due to vortex shedding and the 3D effect due to vorticity changing along the cylinder. They modeled a number of jets on different longitudinal positions on the cylinder surface. It is clear from the results that the vibration amplitude is reduced with increasing water jet velocity. More results about drag coefficient were presented as well. The numerical simulation part was done using hybrid mesh to focus on the required details of vortex shedding. Both the numerical and experimental work of Skaugest et al. shows that using hydrodynamic loads, when inserted on a cylinder surface, reduces the amplitude of vortex-induced vibrations . The position of jets on the surface play an important role in modifying the drag coefficients and vibration amplitude, as the results show.

Lucor et al. [12] simulated and studied the vortex shedding behind a cylinder subjected to an oblique flow. The paper is interesting because inline flow is always not the real case. The numerical simulation was done using the direct numerical simulation technique (DNS), in which the turbulence modeling is not considered. They built their numerical model to be a circular cylinder subjected to an inclined fluid flow. The inclination angle was taken with many values to increase the chance of having many conditions of the study case. The results of Lucor et al. were divided into two main parts – forces coefficients and flow visualization. The paper presents a good visualization of the flow behind stationary and vibrating circular cylinders subjected to oblique fluid flow. The paper showed that the independence principle was not valid for a large angle of attack. They found the base pressure to be lower than the value predicted by the IP, and hence, the drag coefficient is higher than the value predicted by the IP. Even large yaw angles (-60° and -70°) produced large cylinder cross-flow amplitude. Moreover, the study noted that the energy in the Strouhal peak disperses and decreases significantly

with increasing inclination.
Gouxing et al. [13] numerically simulated the vortex-induced vibrations of a 2D circular cylinder subjected to a fluid flow. In this simulation the turbulence model of K-ϵ was used. The SIMPLE algorithm was used to solve presser field. A non-orthogonal boundary-fitted grid was used as well. The study is about presenting a numerical approach and proving its feasibility in solving VIV cases. The numerical approach of Gouxing et al. built on the Boussinesq assumption to be enclosed in Reynolds averaged Navier-Stokes equations. The structure dynamic numerical model was presented as well as a cylinder connected to a spring and damper in both dimensions. Finally, the results were reasonable and proved that the presented approach is feasible in such VIV cases.
Su et al. [14] simulated the cases of VIV for a square cylinder. Unlike most other published papers on this topic, a square cylinder is considered. The problem is classified to be fundamental. They used their own code for the simulation. Both rigid and elastic materials are considered at low Reynolds number of 100. The results gave the value of the Strouhal frequency for the rigid cylinder. Additionally, five vibration modes for an elastic cylinder were captured. The study provides a deep understanding of vibration modes. If the results are compared to equivalent study cases of a circular cylinder, it will be useful for understanding the influence of body shape.
Chen and Li [15] worked numerically on a study case of a carbon fiber reinforced Polymer cable with circular cross-section subjected to a fluid flow with profile velocity. The commercial software Ansys CFX 10.0 was used for the numerical simulation. The cable had an inclination angle and was subjected to a water flow at Reynolds number of 100 and 1000. Fluid-structure interaction modeling was used as well to couple the results between structure and fluid dynamics. FEM and FVM methods were used for structure and fluid flow domains respectively. Figure 1.4 shows in 3D the domains of fluid and structure which were used in the study of Chen and Li. The results of this paper show that Cable oscillation can affect the vortex shedding frequencies. Xu et al. [16] suggested a numerical model of four circular cylinders arranged in inline square configuration. The model is two-dimensional and subjected to low Reynolds number in the order of 200. The spacing (L/D) between cylinders has six values between 2.5 to 6.0. The results show that the spacing plays a significant role in vibrating shapes of rare cylinders as shown in figure 1.5. Moreover, they show that the mean drag and fluctuating lift forces as well as the transverse displacements of upstream raw of cylinders

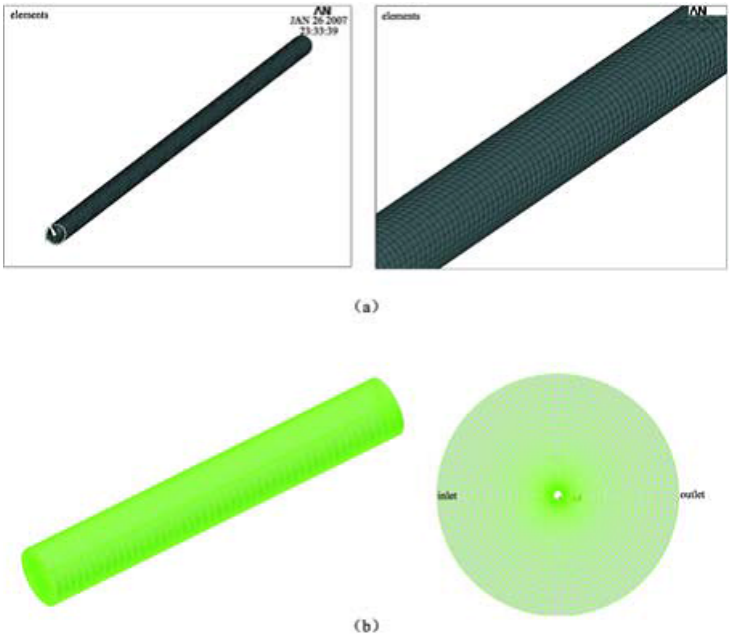

Figure 1.4: [15] both structure (a) and fluid (b) domains.

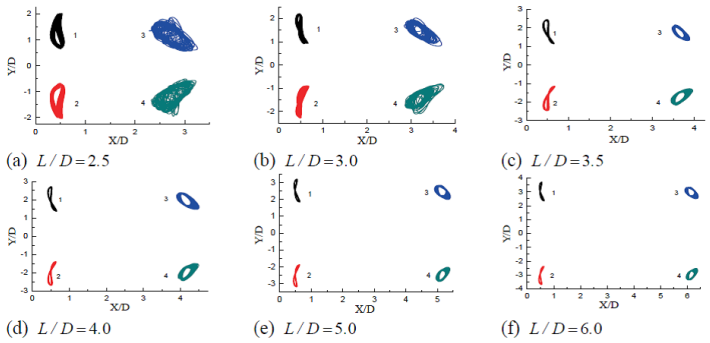

Figure 1.5: [16] X-Y plot of the four vibrating cylinders versus L/D

are larger than those of downstream raw.
Ma and Zhang [17] worked on the effect of Reynolds number and mass ratio on the 2DOF VIV. They used an overlapping mesh in order to achieve more control in such dynamic cases. Remeshing was not required, since overlapping mesh was used. The numerical simulations that were done for a fluid flow had a Reynolds number in the range of $1.0\times10^3<\text{Re}<2.0\times10^4$. In this paper the term "mass ratio" is defined as m*= mass of cylinder/mass of displaced water, and is in the range of 1.0 to 40.0. They concluded that in the lock-in range, the ratios of Y-only displacements to those of X-Y motions maintain about 70%, but remain almost the same outside the range. The ratios of in-line amplitudes to those of cross-flow direction have few relations with Reynolds number. Furthermore the phase angles between X- and Y-displacements decrease as the value of m* has much increased.
Di Silvio et al. [18] studied the fluid elastic vibrations by using both mathematical modeling and experimental work. They described the vortex-induced vibrations as a physical phenomenon by using several mathematical methods. As a first step, they started to get the acting forces on the structure as a function of time. The vortex-origin time concept was studied to determine the control volume on which the momentum equations were to be built. The vortex-origin time is defined as the instant in which the vortex enters the stabilized wake. Then the fluid forces were determined by assuming that the fluid domain deforms in time as well as due to structure vibrations. It is clear that they modeled an oscillated system. The experimental results were analyzed and regarded to be a real application to the determined mathematical model. The experimental work was done with both water and air as working fluid. The model presented in this paper was new at the time because it concerns the physical meaning of the wake width in controlling both the frequency and the amplitude of the alternate driving force.
Diana et al. [4][5] researched on the topic of vibrations of a cylinder due to vortex shedding. The two papers gave results regarding two related cases. It could be said that they complement each other. These papers had been resulted from experimental work, which makes it a good chance to give a real representation and deep understanding of such cases. They started with the case of a circular single cylinder subjected to a fluid flow. In the first case they found that the Strouhal peak force frequency was f=0.2V/D, where V and D are the fluid velocity and cylinder diameter respectively. In the first case the cylinder is supposed to be fixed with no degree of freedom. Afterwards, the experimental work was done for a second case where the cylinder was

allowed to be vibrating. In the second case the value of fluid velocity of the first case was used and then the vortex shedding was synchronous with average vibrating frequency. As a third case, they placed another circular cylinder in the wake of the first one, while the upstream cylinder was not vibrating. If both cylinders have the same diameter, the prevailing harmonic of the force acting on the downstream cylinder, when not vibrating, has a much higher amplitude than in the first case, and when it is vibrating, the range of synchronization is wider than found in the second case. In the last paper they worked on two cases. The first case of the last paper had two cylinders, one of which was not vibrating, and placed in the wake of the vibrating one. Finally they supposed two cylinders with no coupling and each of them was vibrating at a different frequency. They concluded that the vibration of downstream cylinder is strongly influenced by the upstream cylinder vibrations, if both cylinders have the same or very similar natural frequencies.

McConnell et al. [19] worked on a circular cylinder subjected to continuous wave motion. Instead of moving the fluid, the study case was supposed to be a cylinder vibrating in still water. The lift force was measured and plotted in order to give the frequency. The measured lift force as a function of time was compared with the theoretical one. The motion of the cylinder is supposed to be sinusoidal. The results gave more understanding of fluid-structure interaction. The paper presented a parameter called velocity ratio, which could be expressed as $[(A/D)(f_d/f_n)]$, where A is the amplitude of input motion, D is the cylinder diameter, f_d is drag force frequency and f_n is natural frequency. The velocity ratio (VR) can be a significant parameter for characterizing general regions of behavior. Moreover, the lock-on phenomenon is observed to occur when 0.7 to $0.85 <$ VR$<$ 1.05 to 1.15. The flow passing around the cylinder, while it vibrates, had a Reynolds number in the range of 3000 to 25000.

Park et al. [20] did numerical simulations for a cylindrical obstacle in a fluid flow of Re up to 160. The simulations were done using unsteady high resolution calculations and under CFL number around 4. One of the interesting plots of this paper is the presentation of the length of separation bubble as a function of Reynolds number. Whole results of the paper were compared to other papers from numerical and experimental research on the same topic. The results comparison showed good agreement, which proves that the numerical method used is efficient in such cases. The information of flow quantities on the cylinder surface, which are presented in the pa-

per, should be valuable in understanding the flow physics and fluid-structure interaction of similar topics.
Lee and Lee [21] took the usual case of circular cylinder subjected to a fluid flow to be numerically simulated in order to present a computational method, in which both fluid and structural solvers are coupled. The method was tested for Re $<$ 160 and shows good agreement with other published studies. The study case of this paper was simulated for Re = 200, a reduced damping parameter Sg = 0.01, 0.1, 1.0, 10.0 and the mass ratio M* = 1, 10. The cylindrical obstacle was given two degrees of freedom in two-dimensional domains. The tracking of vibration motion shows the eight-shape which is usual for this case, as published in other papers. An unsteady incompressible NS solver was used for simulation. The results show that the cross-flow vibration amplitude is 6D, where D is the cylinder diameter. The mean drag force also increases substantially compared to the fixed cylinder case. Moreover, as it has been shown in other papers, the vibration is strongly dependent on the mass ratio.
Lam and Lin [22] simulated a three-dimensional circular cylinder with different diameters. The cylinders had a wavy shape with regard to diameter. The wavy shape of cylinders was described to be sinusoidal. The Reynolds number of all tested cases had the value of 100˜150. The paper presented a good visualization of the wake behind the cylinder and it was concluded that the ratios of shape wavelength to diameter and of shape amplitude to diameter can significantly modify the tree shear layer development and control the three-dimensional vortices formed behind the wake cylinder. Moreover, the wavy surface of a cylinder can weaken the vortex shedding and hence it increases the base pressure. Furthermore, the optimal range of the wavelength was found to be at wavelength to diameter ratio of 5.5 ˜ 6.0, which would give the greatest effects in drag reduction. Figure 1.6 shows the visualization which was included in the paper. The paper concludes with some of the recommended optimized values which describe the shape, for reducing VIV and vortex in wake.
Lam and Zou [23] numerically and experimentally modeled a four cylinder in inline square configuration. The ratio between cylinder length and diameter varied in range between 1.5˜5.0 along all suggested cases. A three-dimensional numerical modeling using LES technique was used. The paper gave similar conclusions to what Xu et al. [16] had concluded for the same case. If the two papers are compared, then the experimental work of Lam and Zou gives more deep understanding of the case. Moreover, the work of

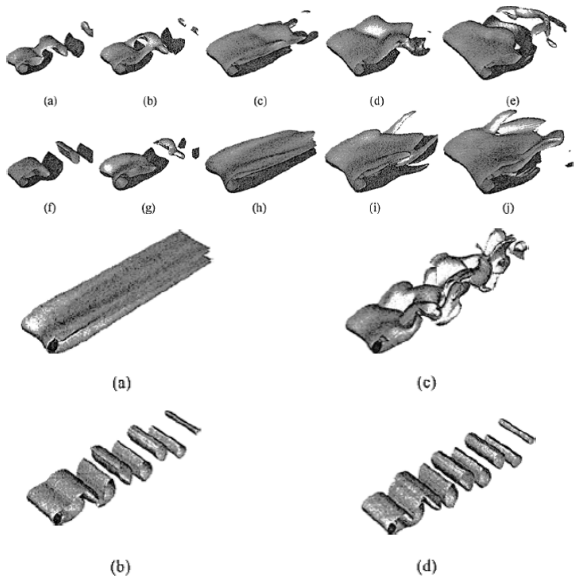

Figure 1.6: [22] Instantaneous vortex structures of wavy (wavelength to diameter = 6 and amplitude to diameter = 0.15) and circular cylinder at Re = 100 (a, b) and Re = 150 (c,d), respectively.

Xu et al. was two-dimensional. The present paper of Lam and Zou compared the experimental results to the numerical one. The comparison between numerical and experimental results shows agreement. The paper does not investigate the vortex-induced vibration but gives more information and conclusions about flow behind and between cylinders. Good visualization of vortices was presented as a part of the experimental results.

Bahmani et al. [24] numerically simulated a single cylinder subjected to a fluid flow. The model used is two-dimensional. They carried out the simulation using their programmed code in order to validate it. The fluid flow had a Reynolds number in the range of $70 < \mathrm{Re} < 170$. The lock-in phenomenon was also captured at low velocities. Navier-Stokes equations in terms of vorticity were numerically modeled to solve the case. The cylinder used was fixed. Their results show agreement with other published ones for the same case. As concluded the algorithm, which had been presented in this paper, is accurate enough to give results are agreed with published ones.

Kim et al. [25] had experimentally studied the FIV of a circular cylinder by attachment of flexible sheets in downstream direction. The sheets angle varied between 90° to -90°. The flexible sheet length varied between 0.5 to

3.0 times cylinder's diameter. The width of sheet varied between 1.0 to and 0.4 times cylinder length. The sheet has a rectangular shape. The results showed a significant influence of the sheet angle on vibration amplitude to cylinder diameter (a/D) ratio. The Reynolds number was 4365 to 74200 in this study. The flexible sheets were attached axially to the cylinder's surface to control flow-induced vibration. The optimal length and minimum width of the flexible sheet that could suppress the flow-induced vibration of the cylinder are 2 to 2.5 times the cylinder diameter and 0.7 times the cylinder length, respectively.

Li et al. [26] experimentally studied the hydrodynamic forces for a VIV case of a flexible circular cylinder. The model used is a 2.6 m steel pipe positioned in a water tank. The mass ratio of this case was 2.62 with Reynolds number range of Re $<$ 9600. The gap ratios (gap to cylinder diameter ratio e/D) at the cylinder ends are 2.0, 4.0, 6.0 and 8.0. The comparison to the published results was performed and showed good agreement. The effect of gap ratio on the force and added mass coefficient is weak for e/D $>$ 2.0, but a significant effect is shown for e/D = 2.0. The study gives the chance for validation of computational work results for the same case.

Stocks et al. [27] worked experimentally on the stability of the Karman vortex street. The study was done on the secondary instability which happens to the fluid flow with Reynolds number in the range of 180˜190. The energy content of four main frequency modes appearing in the wake was measured before and after transition. The energy content remains largely unchanged by the transition process in three of the frequency modes. In the fourth mode of low frequency of turbulent flow (after transition), the energy content became four orders of magnitude higher than before. This amplification mechanism was included here because of transition of the flow wake. Briefly, they carried out some experiments about observing wake behind a cylinder for different frequency modes, after which the energy content of every mode was calculated. Finally, the study provided information about the mode under which the amplification mechanism appears, hence the vortex instability could be observed and studied.

Farge and Sandourny [28] numerically studied the wave-vortex interaction. When the incompressibility constrain is removed, the two-dimensional turbulence is modified, which is what the paper was trying to explain by carrying out some numerical experiments. The full Saint-Venant equations were integrated into the used numerical model. The two flow components, which in this case are inertio-gravitational and potentio-vertical, were found not to

have any energy exchange. The authors observed that the potentio-vortical component of motion behaved as if the fluid is incompressible, in the case of small scales, while on a large scale its energy cascade becomes low. On the other hand, on large scales the inertio-gravitational energy cascade became. Concerning the flow structure in such cases, it was observed that the coherent vortices emerged from such turbulent flow decay. Moreover, the smallest scale vortices kept themselves concentrated inside the vortex core. The study is more mathematical and seems complex work because of the low calculation processing technology at that time compared to today. The paper provides a good understanding of the visualization of such flow interaction.

Deepwater risers are the most known application for VIV. Tang et al. [29] worked on identifying the hydrodynamic coefficients of a slender riser model in the case of VIV. The work is numerical using FSI analysis at the Reynolds number between 2400 and 9600. The riser model has an aspect ratio of 1750. The LES model, which was adopted by Josefsson and Dalton [30], was used. A part of this paper was an experimental study, from which the parameters for structure solver were taken. The hydrodynamic coefficients were measured for both fundamental and higher frequencies. Both the single-mode response and multi-mode response of VIV were considered. The authors concluded that the high-order response frequencies had a significant influence on the root mean square hydrodynamic forces. Moreover, the total hydrodynamic forces at the higher-order frequency components are significantly larger than those at the fundamental frequency. The negative or positive signs of the lift, drag and added mass coefficients are influenced significantly by the phase difference between total hydrodynamic force and response displacement. The meaning of signs in this section could be explained as: the positive lift and drag force coefficients are considered when the dynamic system receives energy from the fluid.

Xu et al. [31] carried out a numerical study with the help of experiments on the in-line VIV of the slender marine structure. Only the in-line vibrations were considered. A wake oscillator model was developed to analyze an in-line VIV of such slender marine structures. Moreover, two different kinds of van der Pol equations were used to describe the near wake dynamics. It was concluded that the presented model is not applicable in the case of non-uniform flows. The results comparison with the experiments concluded that the presented model reproduces some phenomena which are experimentally observed.

Based on a VIV lift force model and the Morison equation, Liu et al. [32]

developed a nonlinear time-dependent VIV model. The developed model considered the fluid-structure interaction and took the in-line vibrations into account. The response-dependent lift force with nonlinear damping was considered to be one of the model characteristics, which makes it different from other published ones. The results showed that the presented model works well for describing the VIV of deepwater risers, because of its agreement with the published papers of the same study case using other models. The model was developed to simulate the cases under non-lock-in condition as a usual condition under which the deepwater risers are operated.

Kumar et al. [33] carried out a number of experiments on a square cylinder subjected to a cross-water flow to study the influence of corner radius on the near wake structure. Five geometries were studied with different r/B ratio of 0, 0.1, 0.2, 0.3 and 0.5, where r is the corner radius and B is the characteristic dimension of the body. The flow velocity on the test point is around 0.2 m/s. The PIV is used to capture the flow field. The results showed an interesting visualization of the wake behind the tested cylinder shapes as shown in figure 1.7. The case of r/B=0.5 did not show any significant dependence of corner radius, however other cases did show such significant dependence. The vortex shedding modes behind the cylinders were characterized by vortex-vortex interactions. At higher r/B ratios, shedding in the near wake was found to be more uniform. Unlike the stationary cylinders, the near wake of cylinders is found to exhibit motion-induced vortex shedding as well as impinging leading edge vortex shedding. The Strouhal number showed nonlinear increasing with respect to r/B ratio in the case of an oscillating cylinder. A so-called passive shedding mechanism was observed in which the vorticity supply to the vortex being shed is not actually cut and the grown vortex is merely pushed downstream by its co-generated vortex. Finally, the results showed that increasing the corner radius can prevent the proneness to the FIV.

As a solution to suppress the VIV, Li et al. [34] supposed controlling the VIV of a cylinder by using a micro actuator. The experiments were carried out for two side-by-side circular cylinders. One of those cylinders was elastically supported and other one was fixed supported at both ends. Both vibrated under the effect of FIV. A micro actuator was placed on the surface of each cylinder in order to control it as explained. What the actuators had done was to perturb the flow boundary layer on the cylinders surfaces. The spacing ratio is fixed at 1.2. The results showed a significant influence of such a method for reducing the response frequency to a value around 2.665 s^{-1}. The results were very sensitive to the actuator excitation frequency and showed

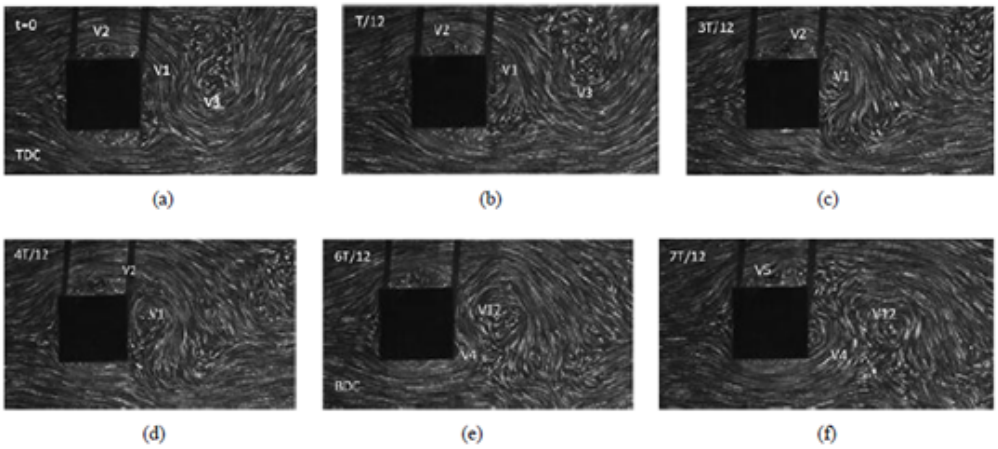

Figure 1.7: [33] Vortex shedding sequence over an oscillatory cycle for r/B=0

that the actuators caused a vibration energy decrease of about 80%. It was found that the most effective position of such an actuator should be near to separation point on the surface cylinder and hence the optimum location was found to be at O=100°. Moreover, it was concluded that the actuator has critical excitation amplitude. Under this critical excitation amplitude, the influence would not be significant and the suppression would be slow.
One of the most interesting references found was the final report of a project at Texas A&M University by Chen et al. [35]. The project aimed to have results from some computational experiments for deepwater risers under real conditions. The simulations were carried out at Reynolds number from $O(10^5)$ to $O(10^7)$, with the aim of modeling the lock-in phenomenon. The authors used both LES and RANS models at different Reynolds numbers. The flexible different types of risers with aspect ratio L/D = 1400 were simulated. In figure 1.8 the mesh used for multi-risers is shown. As shown in the figure, Chimera overset multi-block mesh was used to reduce the time of calculation. A 2D simulation of a flow past a fixed riser at low Reynolds number less than 40 had been also performed as a fundamental simulation. Some results were compared with the previous experiments and showed good agreement. The surface roughness effect was also taken into account. Figure 1.9 shows the X-Y response of a single riser subjected to low Reynolds number flow. As a final conclusion of the project the straked riser, the straked riser gave best performance and less vibrating amplitude.

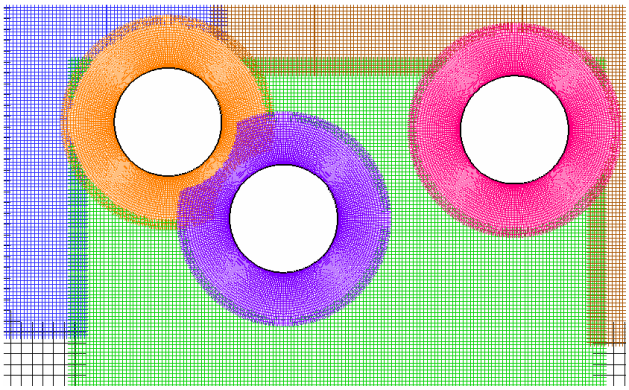

Figure 1.8: [35] Chimera overset mesh used for multi-riser VIV simulation during A&M project.

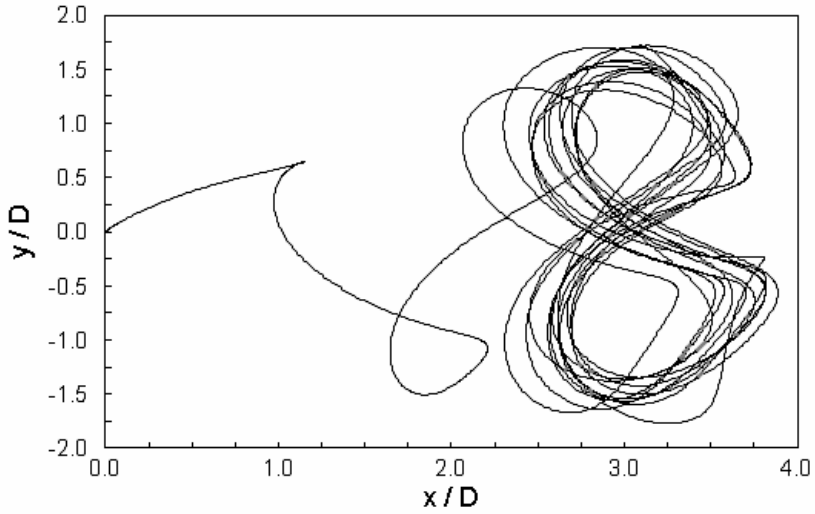

Figure 1.9: [35] the X-Y response of a single riser at low Reynolds number of A&M project.

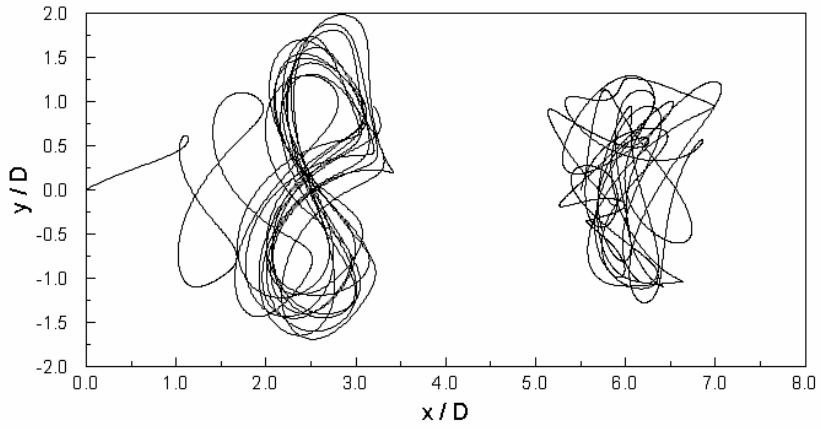

Figure 1.10: [35] the X-Y response of tandem risers at low Reynolds number at spacing of T/D = 5.5(A&M project).

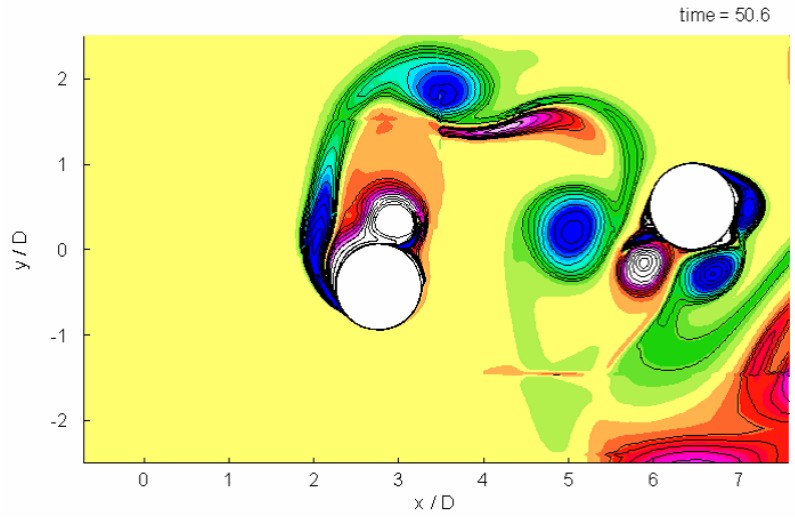

Figure 1.11: [35] the vorticity of tandem risers at low Reynolds number at spacing of T/D = 5.5(A&M project).

1.4 Aim and scope of the research

That dissertation is mainly aimed at studying the vortex-induced vibrations phenomenon and introducing a suppression device for deep water risers. By presenting and validating a developed numerical tool for solving and predicting the behavior of the mentioned vibrations in deepwater risers under the environmental conditions, the phenomenon could be studied computationally. Although the presented computational tool has common basics with the mentioned work of Habchi et al [48], it has a wider range of applicability. The dissertation has furthermore some secondary goals. The main goals can be summarized as follows:

1. Introducing a VIV suppression device.
2. Coupling of two computational solvers in order to get a prediction tool for multi-physics cases.
3. Validation and testing of the presented computational tool.
4. Studying the vortex-induced vibration phenomenon using the presented computational tool.
5. Understanding the effect of design shapes and parameters, e.g. addition of strakes, on the mentioned phenomenon.

The scope of research of the present dissertation is focused on the prediction of the behavior of the deepwater drilling risers under real environmental conditions by using computational simulation, in addition to the evaluation of a presented vortex-induced vibrations suppression device. However the future outlook in chapter 6 recommends that the presented tool should be validated for a wide range of industrial cases.
In chapter 2 the modeling is discussed from both the mathematical and physical viewpoints. This chapter was written mainly based on the references [49], [50], [53], [54], [55], [60] and [72]. The chapter presents the mathematical equations and its implementation into a numerical solver step by step. Furthermore, the coupling between different physics domains is discussed in this chapter from both viewpoints. Moreover, chapter 3 has the scope

of validation and verification of the presented modeling. The validation of the presented fluid-structure interaction tool is carried out by comparing the calculated results by comparable published experiments.
In Chapter 4, the validated tool have been used to study the design and shape parameters on the vortex induced vibrations. By simulating different shapes, the effect of adding strakes to the deep water riser has been investigated. The chapter has introduced to the importance of optimizing the shape of deep water risers as a solution for vortex-induced vibration suppression. From both views of single-physics (rigid submersed bodies) and multi-physics (flexible submersed bodies) the effects of design parameters and shape on the vortex-induced vibrations have been presented.
Chapter 5 is presenting a review on different vortex-induced vibrations suppression devices for the deep water risers. Depending on the understanding, which has been introduced in chapter 5, a vortex-induced vibrations suppression device has been introduced. The suggested design has been investigated using the presented computational tool.
Chapter 6 gives an overview on the contributions of the present work and presents the suggested future work.

Chapter 2

The Computational Modeling

In this chapter, the mathematical modeling of vortex-induced vibration as well as the implementation into an OpenFOAM solver is presented. The theory and nature of the phenomenon will be placed at the beginning to pave the way for mathematical modeling. When the vortex-induced vibrations of flexible bodies is mentioned, the term multi-physics modeling should also be mentioned. In such computational modeling, two domains are present. The fluid model has to be solved to a certain time step and then the information or the output data should be transferred somehow to the solid domain for further solution. Such a loop has to be coupled, so that the coupling in fluid-structure interaction, which is the general title of such cases, has a potential importance. Unlike the usual fluid-structure interaction cases, the vortex-induced vibrations cases have to take into account eddies, and the flow modeling has the significant role in such type of work.

2.1 The Nature of the Vortex-Induced Vibrations

The topic is about two physical domains interacting and influencing each other. The case physics therefore has to deal with both interacting domains as well as the interaction or so-called coupling at the interface. At the interface, a physical modeling of the domains coupling has to be taken into account. The following sections will present and explain these items from the viewpoint of physics. The Fluid-Structure Interaction is a physical phenomenon produced by the pressure difference caused by fluid flow around

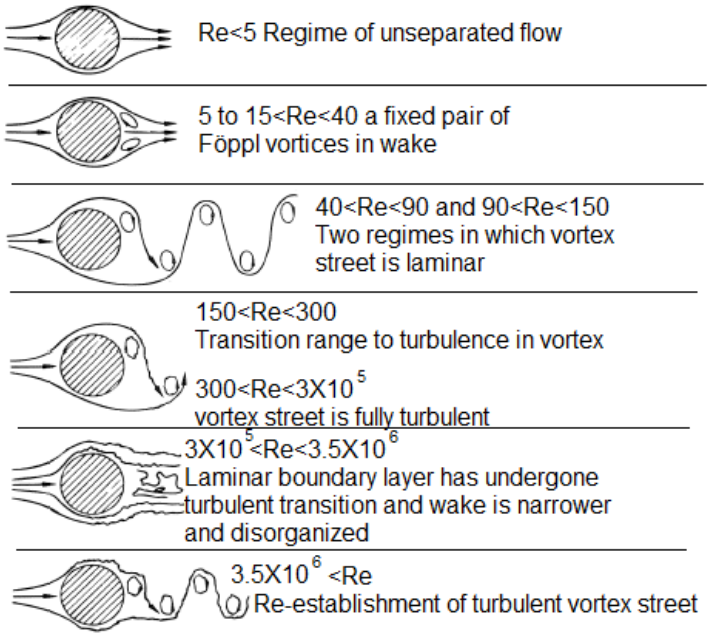

Figure 2.1: The effect of Reynolds number of the flow around a cylinder [43].

a structure. It can be associated by the physical understanding of Flow-Induced-Vibrations and vortex-induced vibrations. The structure in this case is loaded by a static load caused by a pressure difference, which can be occured due to the dynamic instability of the structure. The phenomenon known as Flutter occurs when the damping is less than the energy transferred by the vortex-induced wake and creates a resonance with the structure with negative damping [40, 41].

2.1.1 The Fluid Flow

As per the potential theory of fluid flow, the flow around an obstacle becomes symmetric at low Reynolds number [42]. The fluid flow losses this symmetry as the Reynolds number gets high [2]. Figure 2.1 shows how the flow around a circular cylinder could be affected by increasing the diameter-based Reynolds number.

The concept of the vortex flow basically is about the separation point instability. This instability, which occurs at certain ranges of Reynolds number as mentioned above, generates the so-called vortex shedding in wake flow.

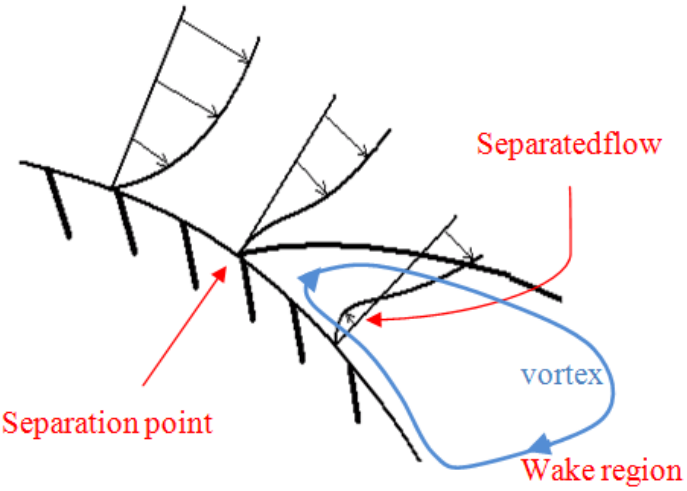

Figure 2.2: The physical meaning of the separation point on cylinder surface [44].

Figure 2.2 shows graphically the physical meaning of the separation point on cylinder surface.
The shape of vortex shedding is not a common property for all cases, but it differs according to some other physical properties of every case. Figure 2.3 shows the different shapes of vortex shedding. As a result of what has been explained above, the pressure and forces on the obstacle surface will be unstable as well. The instability of lift and drag forces will result in body motion, if it has one or more degrees of freedom. Figure 2.4 shows Pressure coefficient radial distributions on a cylindrical obstacle surface subjected to vortex flow conditions. As shown in figure 2.4, the distribution curves seem to be symmetric around 0-point. Because of separation point position instability, this curve loses its symmetry. As a result of this scenario, the drag and lift values on the surface fluctuate. If the solid body is free to move, it will vibrate as a rigid body or be deformed as a flexible obstacle.

2.1.2 The Nature of the Flexible Solid

In this section, a general view on solid deformation physics is presented. It will only be focused on what is related to and covers the vortex-induced

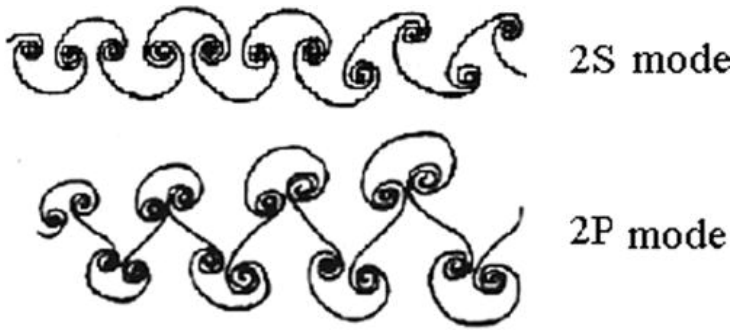

Figure 2.3: The different shapes of vortex shedding [45].

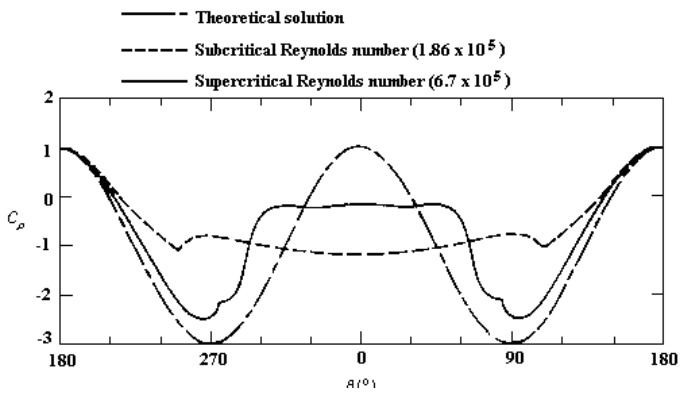

Figure 2.4: Pressure coefficient radial distributions on a cylindrical obstacle surface subjected to vortex flow conditions [46].

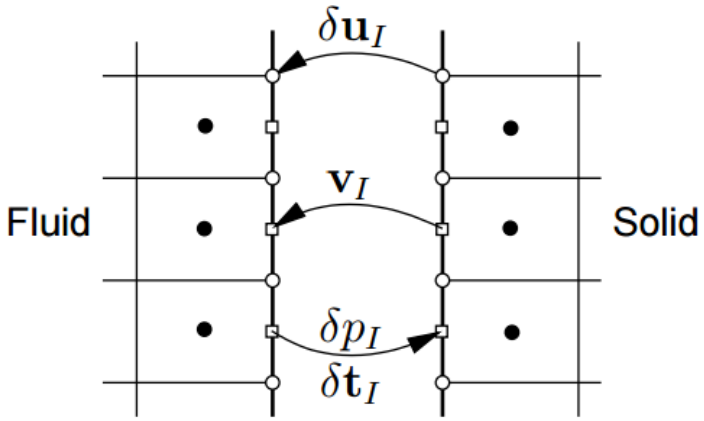

Figure 2.5: A simple graphic shows the quantities exchange at the fluid-solid interface. Where $d\mathrm{u}_I$, v_I are displacement increment and velocity from the solid side respectively and dp_I, $d\mathrm{t}_I$ are pressure viscous force increment from the fluid side [53].

vibrations topic.
Since forces are exerted on a solid surface, the solid will respond physically by presenting deformations according to its given degrees of freedom. The deformations and their properties depend significantly on the material physical properties, e.g. elasticity.
Elastic materials are commonly used for VIV investigations. The present work considers only elastic materials. Moreover, in the following sections 2.2 and 2.4, more information will be presented regarding elasticity of solids and its influence on the VIV investigations.

2.1.3 The Coupling

Under the general title of fluid-structure interaction - FSI coupling, a general meaning of multi-physics interface could be specified to include solid deformation caused by fluid pressure. At the interface between the two physically different domains, the physical quantities such as pressure are transferred. Moreover, the deformation of the interface must be transferred from the solid domain to the fluid domain. In addition to physical quantities exchange, the fluid domain has to be updated to adopt the solid deformation. The coupling therefore is a main issue to be considered at physical and mathematical

modeling for any FSI case and not only VIV. Figure 2.5 shows graphically the exchange between solid and fluid regions.

2.2 Mathematical Interpretation

As for any other mechanical system, the fluid flow is usually governed by conservation laws. Three common laws of conservation are usually applied to the fluid flow system. Unlike any other mechanical system, the fluid flow is difficult to track through a specific set of particles. The so-called Eulerian system is therefore commonly used in this case. The Eulerian system means that the equations are written for a fixed volume in space, which does not move. The used total time derivative D/Dt could be expressed as the following:

$$\frac{D}{Dt} = \frac{\partial}{\partial t} + \nabla.U = \frac{\partial}{\partial t} + U_i \frac{\partial}{\partial x_i} \tag{2.1}$$

2.2.1 Fluid Domain

In this section the mathematical modeling is represented [72]. Consider an isothermal continuum element in an arbitrary volume V bounded by a surface S at a time t. The continuum is then governed by the fundamental conservation laws for mass.

$$\frac{\partial \rho}{\partial t} + \nabla.\left(\rho \mathbf{U}\right) = 0 \tag{2.2}$$

Where ρ is the continuum density (whether it is a fluid or solid constituent), U is the constituent velocity, which is represented to a Cartesian coordinate system with basis vectors, taken on the components $[\mathrm{v}_i]_{i=x;y;z}$. The subscript *"i"* refers in this equation to the element numbering in one dimensional space. Since the flow is incompressible, the equation 2.2 could be written as follows:

$$\nabla.\mathbf{U} = 0 \tag{2.3}$$

The conservation of momentum is basically driven by Newton's second law, which could be expressed mathematically as follows:

$$\mathbf{F}{=}m\frac{\mathbf{D}U}{\mathrm{D}t} \tag{2.4}$$

Where F represents the vectorial force acting on the Eulerian volume, where m represents the mass of fluid in the Eulerian volume. This vectorial force also includes the surface forces, i.e. pressure and viscous force.
Equation 2.4 includes a total time derivative, which could be used along with equation 2.1 to express the conservation of momentum per unit volume as follows:

$$\rho\frac{\partial(\mathbf{U})}{\partial t}+\nabla\rho.\,(UU) = -\nabla p + \nabla.\tau \tag{2.5}$$
$$\rho\frac{\partial(U_i)}{\partial t} + \rho\frac{\partial(U_iU_j)}{\partial x_j} = -\frac{\partial p}{\partial x_i} + \frac{\partial \tau_{ij}}{\partial x_j}$$

Where p, τ and q represent pressure, viscous stress tensor and body acceleration of the element i (i.e. external term of momentum) respectively.
The convective term $\rho\nabla.\,(\mathrm{UU})$ has a total of nine components corresponding to three convective terms in each of the three equations, from which the unnumbered equation is derived. Even if the term with the divergence of velocity is zero in an incompressible case, it must be included in the equations when an iterative procedure is used for solving a steady-state case. The reason is that mass conservation is not guaranteed during the solution process.
The viscous stress tensor"τ" is defined as:

$$\tau_{ij} = \mu\left(\frac{\partial \mathrm{u}_i}{\partial x_j} + \frac{\partial \mathrm{u}_j}{\partial x_i}\right) + d_{ij}\lambda\ (\nabla.\mathrm{U}) \tag{2.6}$$

$$\tau_{ij} = \begin{bmatrix} \tau_{xx} & \tau_{xy} & \tau_{xz} \\ \tau_{yx} & \tau_{yy} & \tau_{yz} \\ \tau_{zx} & \tau_{zy} & \tau_{zz} \end{bmatrix}$$

Where d_{ij} represents the unit tensor for the element with position i and j, while d_{ij} is 1 for $i{=}j$ and is 0 for $i{\neq}j$. The term λ is so-called $\lambda - viscosity$ which is disappeared, since the term $(\nabla.\mathrm{U})$ is equal to zero according to the equation 2.3. It means:

$$\tau_{xx} = 2\mu\frac{\partial \mathrm{u}_i}{\partial x}, \tau_{yy} = 2\mu\frac{\partial \mathrm{u}_j}{\partial y}, \quad \tau_{zz} = 2\mu\frac{\partial \mathrm{u}_k}{\partial z}$$

$$\tau_{xy} = \tau_{yx} = \mu(\frac{\partial \mathrm{u}_i}{\partial y} + \frac{\partial \mathrm{u}_j}{\partial x}),$$

$$\tau_{xz} = \tau_{zx} = \mu(\frac{\partial \mathrm{u}_i}{\partial z} + \frac{\partial \mathrm{u}_k}{\partial x}),$$

$$\tau_{zy} = \tau_{yz} = \mu(\frac{\partial \mathrm{u}_k}{\partial y} + \frac{\partial \mathrm{u}_j}{\partial z})$$

Where μ is the dynamic viscosity.
By defining the term *shear stress tensor* as $\frac{\tau}{\rho} = 2vS$, where v is the kinematic viscosity, which could be related to the dynamic viscosity as $v = \frac{\mu}{\rho}$, the equation 2.6 can be rewritten as follows:

$$\frac{\tau_{ij}}{\rho} = v\left(\frac{\partial \mathrm{u}_i}{\partial x_j} + \frac{\partial \mathrm{u}_j}{\partial x_i}\right) \tag{2.7}$$

Since the density is a constant value, the momentum equation 2.5 in its final form for every incompressible Newtonian fluid could be rewritten as follows:

$$\frac{\partial \mathbf{U}}{\partial t} + \nabla.(\mathbf{U}U) = -\nabla(\frac{p}{\rho}) + \nabla.(2v\mathrm{S}) + \mathbf{q} \tag{2.8}$$

$$\frac{\partial \mathrm{U}_i}{\partial t} + \frac{\partial}{\partial x_j}(\mathrm{U}_i\mathrm{U}_j) = -\frac{\partial}{\partial x_j}(\frac{p}{\rho}) + \frac{\partial}{\partial x_j}(2v\mathrm{S}_{ij}) + q_i$$

The foregoing equation is more commonly known as the Navier-Stokes equation. The fluid flow is governed by unsteady Navier-Stocks equations for viscous incompressible fluids. Since these equations are only valid for static meshes [48], the so-called Arbitrary Lagrangian–Eulerian mapping must be used. This kind of mapping is very commonly used in fluid-structure interaction solvers.
The mapped governing equations could be written in the following form:

$$\frac{\partial U}{\partial t} + (U - U_m)\nabla U = -\frac{\nabla p}{\rho} + \nu\nabla^2 U \tag{2.9}$$

Where U, U_m, p, υ and ρ are fluid velocity in static fluid domain at time zero $\Omega(f, 0)$, mesh velocity in fluid domain $\Omega(f, t)$, pressure and fluid density respectively. The difference between fluid velocity and mesh velocity is called the convective term.

Finite volume discretization

The presented solver mainly discretizes the fluid and solid domains into finite volumes, which are commonly called cells. The presented tool uses the finite volume method in both solid and fluid domains. The values are basically

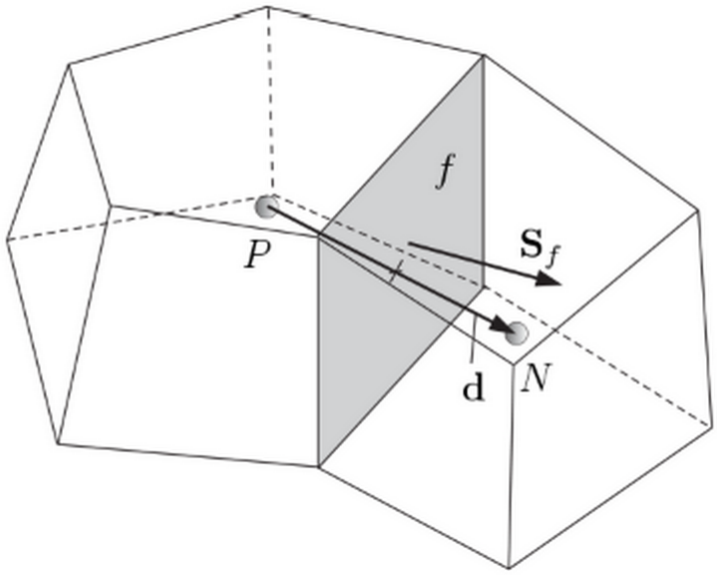

Figure 2.6: Cells in OpenFOAM (reprint from [72])

restored in the center of cells. The finite volumes must be always positive, while they fill the entire domain. On faces, the results or values must be mapped by using a cell-to-face mapping. Figure 2.6 shows two cells, as OpenFOAM understands [72]. The figure shows P and N cells at center-to-center distance of d and cell common surface vector S_f . Every cell therefore has a neighbor and a surface vector towards the neighbor called n, while the common surface f has an area of $\mid S_f \mid$. The surface vector therefore has a value equal to the multiplication of both vector n and surface area S_f.
The distance vector d, which connects the center of owner cell P to the neighbor cell N, could be formulated as $d = PN$. The owner surface vector can be likewise expressed as P_f,which connects the center of owner cell to the common face center. The vector N_f could be expressed in the same way. Such space discretization is general and based on so-called unstructured mesh. For structured mesh, the discretization will be more mapped because the distance vector in this case will usually be co-lineared to the surface vector.
Discretization of governing equations according to the finite volume approach requires that they should be integrated over a control volume [72]. As men-

tioned, the general governing equation could be expressed as follows:

$$\frac{\partial \Phi}{\partial t} + \nabla \cdot (\mathbf{U}\Phi) = \nabla \cdot (\alpha \nabla \Phi) + \mathbf{q}_\Phi \tag{2.10}$$

After integration over control volume, it becomes:
time derivative convection term diffusion term source term

$$\overbrace{\int_V \frac{\partial \Phi}{\partial t} dV} + \overbrace{\int_V \nabla \cdot (\mathbf{U}\Phi)\, dV} = \overbrace{\int_V \nabla \cdot (\alpha \nabla \Phi) dV} + \overbrace{\int_{\mathbf{V}} \mathbf{q}_\Phi dV} \tag{2.11}$$

Since the time derivative and source term are straightforward integrations, the implicit Euler method could be used for the approximation. The implicit Euler method is used in the present work for the fluid domain discretization. For more accuracy, it could be written in its second order form as follows:

$$\int_V \frac{\partial \Phi}{\partial t} dV \approx \frac{3(\Phi V)^{n+1} - 4(\Phi V)^n + (\Phi V)^{n-1}}{2\Delta t} \tag{2.12}$$

Where the superscript n as well as *n+1* represent the time marching levels. The so-called Gauss divergence theorem [73] could be expressed in the following form:

$$\int_V \nabla * \Phi dV = \int_S \Phi * dS \tag{2.13}$$

Where Φ is a (smooth) tensor field, $\nabla *$ represents any of the derivatives $\nabla \cdot$ (divergence), $\nabla \times$(curl) or ∇(gradient). It is considered that the surface S is closed and encloses the volume V_p and dS is a surface vector pointing out of the volume. Applying this expressed theorem to convective term will turn the volume integral to surface integral as follows:

$$\int_V \nabla \cdot (\mathbf{U}\Phi)\, dV = \int_S \Phi \mathbf{U}\ dS \tag{2.14}$$

By applying a summation over finite discrete parts, S_f, of surface S, the convection term can be approximated as follows:

$$\int_V \nabla \cdot (\mathbf{U}\Phi)\, dV = \int_S \Phi \mathbf{U}\ dS \approx \sum_f \Phi \mathbf{U} \cdot \mathbf{S_f} \tag{2.15}$$

By applying the same scenario on the diffusion term, the discrete form of the general equation is finally written as follows:

$$V_P \frac{\partial \Phi}{\partial t} + \sum_f \Phi \mathbf{U} \cdot \mathbf{S_f} = \sum_f (a \nabla \Phi) \cdot \mathbf{S_f} + V_P \mathbf{q}_\Phi \tag{2.16}$$

The variables in this equation are stored in finite volume center and need to be expressed on surfaces *(since the integral form is turned into surfaces as well).* The interpolation should be used to carry out this task. Many types of interpolation could be used for such a task, e.g. linear interpolation [72].

Turbulence and eddies

For VIV cases the large eddy simulation – LES is mostly used. In this section, the LES turbulence model will be explained. For removing the small scales from Navier–Stokes equations, the LES filter has to be applied, allowing the numerical solution to be carried out more quickly. The LES filter can be applied on a field $\Phi(x,t)$which is spatial and temporal, e.g. velocity field of a fluid flow. The LES filter operation could be temporal, spatial or both. The resulting field after filtering can be expressed as follows [49, 50]:

$$\overline{\Phi(\mathrm{x},\mathrm{t})} = \int_{-\infty}^{\infty}\int_{-\infty}^{\infty} \Phi\left(\mathrm{r},\mathrm{t}'\right) \mathrm{G}\left(\mathrm{x}-\mathrm{r},\mathrm{t}-\mathrm{t}'\right) \mathrm{dt}'\mathrm{dr} \tag{2.17}$$

The upper bared symbols represent the filtered variables, while $\mathrm{t}'$and r are spatial and temporal steps values.
G is the filter convolution kernel, where: $\overline{\Phi} = G * \Phi$
The filtered Navier-Stokes equations for incompressible fluid flows could be expressed as follows:

$$\frac{\partial \overline{u}_i}{\partial t} + \frac{\partial}{\partial x_j}\left(\overline{u_i u_j}\right) = -\frac{1}{\rho}\frac{\partial \overline{p}}{\partial x_i} + \nu\frac{\partial}{\partial x_j}\left(\frac{\partial \overline{u_i}}{\partial x_j} + \frac{\partial \overline{u_j}}{\partial x_i}\right) = -\frac{1}{\rho}\frac{\partial \overline{p}}{\partial x_i} + 2\nu\frac{\partial}{\partial x_j}S_{ij} \tag{2.18}$$

Where $\overline{\mathrm{p}}$ is the filtered pressure field and S_{ij} is the rate-of-strain tensor.
The nonlinear filtered advection term $\overline{u_i u_j}$could be expressed as follows [51]:

$$\overline{u_i u_j} = \tau_{ij}^r + \overline{u_i}\,\overline{u_j} \tag{2.19}$$

Where τ_{ij}^r is the residual stress tensor, so that the filtered Navier-Stokes equations become:

$$\frac{\partial \overline{u}_i}{\partial t} + \frac{\partial}{\partial x_j}\left(\overline{u_i u_j}\right) = -\frac{1}{\rho}\frac{\partial \overline{p}}{\partial x_i} + 2\nu\frac{\partial}{\partial x_j}S_{ij} - \frac{\partial \tau_{ij}^r}{\partial x_j} \tag{2.20}$$

Beside the foregoing filtering of the mass and momentum equations, the kinetic energy equations should be filtered as well. The total filtered kinetic

energy could be expressed as follows:

$$\overline{E} = \frac{1}{2}\overline{u_i u_i} \tag{2.21}$$

The total filtered kinetic energy $\overline{E}$ could be decomposed into two terms: the kinetic energy of the filtered velocity field E_f and the residual kinetic energy k_r, which can be expressed as follows:

$$E_f = \frac{1}{2}\overline{u_i u_i} \tag{2.22}$$

$$k_r = \frac{1}{2}\overline{u_i u_i} - \frac{1}{2}\overline{u_i u_i} = \frac{1}{2}\tau_{ii}^r \tag{2.23}$$

While

$$\overline{E} = E_f + k_r \tag{2.24}$$

By multiplying the filtered momentum transport equation by$\overline{u_i}$, the conservation equation for E_f can be expressed as follows:

$$\frac{\partial E_f}{\partial t} + \overline{u_j}\frac{\partial E_f}{\partial x_j} - \frac{1}{\rho}\frac{\partial \overline{u_i p}}{\partial x_i} + \frac{\partial \overline{u_i} t_{ij}^r}{\partial x_j} - 2\nu\frac{\partial \overline{u_j}\,\overline{S_{ij}}}{\partial x_j} = -\epsilon_f - \Pi \tag{2.25}$$

Where $\epsilon_f = 2\nu\overline{S_{ij}S_{ij}}$ is the kinetic energy dissipation of the filtered velocity field by viscous stress, and $\Pi = -\tau_{ij}^r\overline{S_{ij}}$ is the sub-filter scale (SFS) dissipation of kinetic energy.
The left-hand side terms represent transport, and the right-hand side terms represent the dissipated kinetic energy sink [52].
The so-called one-equation LES model solves one turbulent transport equation, usually the turbulent kinetic energy.

2.2.2 Solid Domain

In the present study, a finite volume structural solver employing an incremental strain-updated Lagrangian approach is used for solving the solid domain. This section will explain the mathematical modeling for this part of the solver.
This mathematical modeling allows strains in a good range, which is needed in the field of deep risers engineering as well as the validation study case of the present study. This part of the solver had been developed as explained

in the research paper of Tukovic et al. [54]. The motion of an isothermal continuum in an arbitrary volume V bounded by a surface S is governed by the mass and linear momentum conservation laws, which is mathematically presented in the equations 2.26 and 2.27, which could be somehow considered as a rewrite of equation 2.2 but in its solid domain mathematical suitable formulation [54].

$$\frac{d}{dt}\int_V \rho \; dV + \oint_S n \cdot \rho \left(\vec{\mathrm{v}} - \vec{\mathrm{v}}_s\right) \; dS = 0 \tag{2.26}$$

$$\frac{d}{dt}\int_V \rho \mathrm{v} \; dV + \oint_S n \cdot \rho \left(\vec{\mathrm{v}} - \vec{\mathrm{v}}_s\right) \; dS = \oint_S n \cdot \sigma \; dS \tag{2.27}$$

where ρ, n, v, v_s and σ are the continuum density, the outward pointing unit normal to the surface S, the velocity of the continuum, the velocity of the surface S and the Cauchy stress tensor respectively.
The rate of change of the volume V and the velocity v_s could be written in a mathematical relationship expressed in the following equation 2.28. This relationship is commonly defined by the space conservation law.

$$\frac{d}{dt}\int_V dV - \oint_S n \cdot \mathrm{v}_s \; dS = 0 \tag{2.28}$$

The presented solver is assumed to deal with elastic and isothermal structures. The behavior of such structures is usually described by only the linear momentum conservation law in its Lagrangian formulation, which is expressed as the following equation 2.29.

$$\frac{\mathrm{D}}{\mathrm{D}t}\int_V \rho \mathrm{v} dV = \oint_S n \cdot \sigma \; dS \tag{2.29}$$

For the initial configuration, at which the structure is unreformed, the foregoing equation 2.29 could be rewritten as follows:

$$\int_{V_0} \rho \frac{\partial \mathrm{v}}{\partial t} \; dV_0 = \int_{S_0} n_0 \cdot \left(\Sigma \cdot F^T\right) dS_0 \tag{2.30}$$

Where the subscript 0 expresses the initial configuration quantities, while u and v are displacement vector and velocity vector respectively. The quantity F expresses the deformation gradient tensor, which could be defined in the following equation 2.31.

$$F = I + (\nabla u)^T \tag{2.31}$$

The Σ in this context represents the second Piola-Kirchhoff stress tensor. The relationship between Cauchy and Piola-Kirchhoff stress tensors could be written as follows:

$$\sigma = \frac{1}{\det F} F \cdot \Sigma \cdot F^T \tag{2.32}$$

The displacement vector u is defined as the difference between the initial position of the particle set and its current configuration value u = r - r_0.
The incremental from the equation 2.30, which represents the total Lagrangian description of the linear momentum conservation law, could be mathematically expressed as follows:

$$\int_{V_0} \rho_0 \frac{\partial \delta \mathrm{v}}{\partial t}\, dV_0 = \int_{S_0} n_0 \cdot \left(\delta\Sigma \cdot F^T + \Sigma \cdot \delta F^T + \delta\Sigma \cdot \delta F^T\right) dS_0 \tag{2.33}$$

Where the symbol δ represents the increment of the attached quantity.
As mentioned, the updated Lagrangian formulation is used in the presented solver mathematical modeling. By identifying that F=I in the foregoing equation 2.31, the updated Lagrangian formulation could be mathematically presented as follows:

$$\int_{V_u} \rho_u \frac{\partial \delta \mathrm{v}}{\partial t}\, dV_u = \int_{S_u} n_u \cdot \left(\delta\Sigma_u + \Sigma_u \cdot \delta {F_u}^T + \delta\Sigma_u \cdot \delta {F_u}^T\right) dS_u \tag{2.34}$$

The subscription u represents the quantities related to the updated configuration. The foregoing equation 2.34 is supposed to be the main form on which the final formulation of the presented mathematical modeling is based. The update configuration namely performs a tensor transfer of the accumulated second Piola-Kirchhoff stress. Such tensorial transformation is identical to Piola-Kirchhoff into Cauchy stress tensor transfer.
By implementing the relationship between Piola-Kirchhoff stress and Green-Lagrangian strain tensor, the foregoing equation 2.34 becomes:

$$\int_{V_u} \rho_u \frac{\partial \delta \mathrm{v}}{\partial t} \mathrm{d}V_u - \oint_{S_u} \mathrm{n}_u \cdot (2\mu + \lambda) \nabla d \mathrm{ud}S_u = \oint_{S_u} \mathrm{n}_u \cdot \mathbf{q}\ \mathrm{d}S_u \tag{2.35}$$

Where the diffusivity term $(2\mu + \lambda)$ contains the Lame's coefficients μ and λ. Moreover, the normal derivative of the displacement increment at boundaries with specified traction and pressure increment depending on the basis of

equation 2.35 could be mathematically expressed as follows:

$$\begin{aligned}\mathrm{n}_u \cdot \nabla d\mathrm{u} = & \\ & \left[(dt - dp\mathrm{n})\,\frac{dS}{dS_u} - \mathrm{n}_u \cdot \Sigma_u \cdot \delta {F_u}^T\right] \\ & \cdot \frac{(F_u^{-1})^T}{(2\mu+\lambda)} - \frac{\mathrm{n}_u \cdot \left[\mu(\nabla d\mathrm{u})^T + \lambda\ \mathrm{tr}\,(d\mathrm{u})\,\mathrm{I} - (\mu+\lambda)\,\nabla d\mathrm{u}\right]}{(2\mu+\lambda)} - \\ & \frac{\mathrm{n}_u \cdot \left[\mu \nabla d\mathrm{u} \cdot (\nabla d\mathrm{u})^T + 0.5\ \lambda\,(\nabla d\mathrm{u} : \nabla d\mathrm{u})\,\mathrm{I}\right]}{(2\mu+\lambda)}\end{aligned} \tag{2.36}$$

Where t and p represent the traction and pressure respectively.

Finite volume discretization

In the present work, the dynamic behavior of the considered structure is being described by the linear momentum conservation law written in its incremental updated Lagrangian form. The computational mesh therefore must be moved at each time step by using the displacement increment vector obtained in the previous time step. In the applied cell-centered finite volume method, the unknown displacement increment is calculated at the control volume center. In order to move the mesh, the displacement increment must be interpolated from the control volume centers to the control volume points. This procedure can be done using the the following weighted averaging interpolation (see [54]):

$$\delta u_p = \frac{\sum_c \omega_{pc}\left[\delta u_c + (r_p - r_c)\cdot(\bigtriangledown \delta u)_c + \frac{1}{2}(r_p - r_c)^2 : (\bigtriangledown \bigtriangledown\, \delta u)_c\right]}{\sum_c \omega_{pc}} \tag{2.37}$$

where δu_p is the point displacement increment, δu_c is the cell center displacement increment and the summation is preformed over all cells, which are sharing the point p. The weighting factor ω_{pc} can be expressed as following:

$$\omega_{pc} = \frac{1}{|r_p - r_c|} \tag{2.38}$$

where r_c is the cell center position vector and r_p is the point position vector. The spatially discretized form of the equation 28 for the updated control

volume V_{Pu} is expressed as following:

$$\rho_{P_u} V_{P_u} \frac{\partial \delta V_P}{\partial t} - \sum_f (2\mu_f + \lambda_f) n_{fu} \cdot (\bigtriangledown \delta u)_f S_{fu} = \sum_f n_{fu} \cdot q_f S_{fu} \qquad (2.39)$$

where the subscripts P and f represent the cell and face values. The face values of all dependent variables are calculated by linear interpolation of the neighboring cell values.

Degree of freedoms and frequency

Both definitions need to be mentioned in this context. The vibration frequency of the studied structure has important physical and mathematical relationships which required to be clearly explained in this section of dissertation.
As mentioned in the reference [54] and as understood mathematically from the foregoing equations 2.29, 2.30, 2.31 and 2.35, the finite volume in the solid domain can move in 6 degrees of freedom (since the domain is supposed to be discretized into finite volumes, as discussed). The mentioned finite volume can namely translate into the three Cartesian coordinates and rotate around them. This condition is trivially applicable if the studied case is basically three-dimensional. In the present work, all considered cases are three-dimensional, which means that every solid in these considered cases has basically 6 degrees of freedom.
Avoiding lock-in phenomena is an important topic when studying VIV. The phenomenon of lock-in happens when the vortex shedding frequency becomes close to the natural frequency of vibration of the structure. Because of this, checking the frequencies and possibility of lock-in occurring should be mentioned in this scope.
Calculating the Strouhal number gives a dimensionless value, which relates the vortex shedding frequency f to obstacle diameter d and flow velocity u as written in the following expression:

$$St = \frac{fd}{u}$$

Measuring or calculating the natural frequencies in both conditions wet and dry is therefore recommended. In the present ,study the natural frequencies of the studied structures were calculated numerically using “ANSYS Modal”.

Xu et al. [74] studied mathematically the frequencies in fluid structure interaction. A mathematical modeling and analysis were clearly done in this reference. Although the presented solver cannot give a direct frequency analysis, the mentioned reference provided the best knowledge to the author regarding this topic.

2.2.3 Coupling

The coupling in fluid-structure interaction cases is always an important issue. Fernandez [71] made a comparative study of every type of coupling and their formulation, providing the author with a good overview of the existed coupling techniques.
Usually the solution of coupled problems has two main categories of coupling, i.e. monolithic and partitioned. In the following text, the difference between these will be discussed. Moreover, the reasons under which the presented solver coupling was chosen will be explained.
The monolithic approach represents the strong coupling algorithm for the fluid-structure interaction problems [53]. It is recommended and considered when the interaction is very strong. It has the advantage of good stability and convergence. However, in some cases it can lead to ill-conditioned matrices or sub-optimal discretization. In other cases sub-optimal solution procedure in fluid or solid region can be expected. Because of its suitability and the disadvantages mentioned, this technique was not used in the presented solver.
The partitioned approach can represent both weak and strong coupling of fluid-structure interaction problems [53]. This technique has a wider range of flexibility than the monolithic regarding coupling strength. Although the coupling is commonly used for weakly coupled problems, it can also be modified to suit the strongly coupled ones. The strong coupling can occur by implementing an additional iteration loop over partial solvers, which requires a convergence acceleration method. Using this technique, the coupling is achieved by enforcing the kinematic and dynamic conditions on the interaction interface. The main features of this technique can be summarized in the following main points:

1. Sequential solution of solid and fluid solvers only once per time step.

2. Implicit coupling.

3. Preservation of 2nd order time accuracy needs special attention.

For weakly coupling techniques, the solution in stability occurs in the cases in which incompressible fluids (e.g. water) and a light or highly flexible structure (e.g. flexible rubber) exist. The density ratio in such unstable cases is usually about 1. The experiments of Tukovic et al. [54] show that the instability for such weakly coupled problems grows with decreasing time step size, density ratio, fluid viscosity or solid stiffness. Appendix A gives an overview of the standard weakly coupled fluid-structure interaction solver of OpenFOAM.
The selected coupling approach in the present study has a partitioned approach with strong coupling algorithm. Moreover, an updated Lagrangian finite volume solver for elastic solids is used. The selected coupling technique is therefore the adaptive under-relaxation and the strong coupling of Aitken. The formulation and concept of the selected coupling technique will now be explained.
The adaptive iterative under-relaxation algorithm of Aitken and a partitioned strong coupling are selected to be implemented and used in order to achieve the best results for the case study of deepwater risers [53]. Figure 2.7 shows the coupling loop as a part of the presented solver.

2.3 Stability

The stability of a fluid-structure interaction partitioned coupling using Aitken under-relaxation algorithm was investigated in some research papers. Some research works have concluded that the number of coupling iterations increases as the time step decreases or along with increasing the solid flexibility, which can play a role increasing the strain of structure [55].
As concluded by Degroote et al. [55] as well as the present study, the unstable components of coupling usually appear in the first coupling iterations. Moreover, the large deformations have a significant influence on the whole coupled solver. Such large deformations will be transferred through coupling to the fluid mesh, which could crash the whole process. Unlike the work of Degroote, the present solver shows more influence of mesh refinement, with large deformations able to be overcome by finer meshes. This point will be discussed in more detail in the next chapter under the validation topic.
Wong et al. [56] agreed with the point of view of Degroote as well as the present study regarding the flexibility of structure and density ratio. Furthermore, they agreed with the present study and paid more attention to the

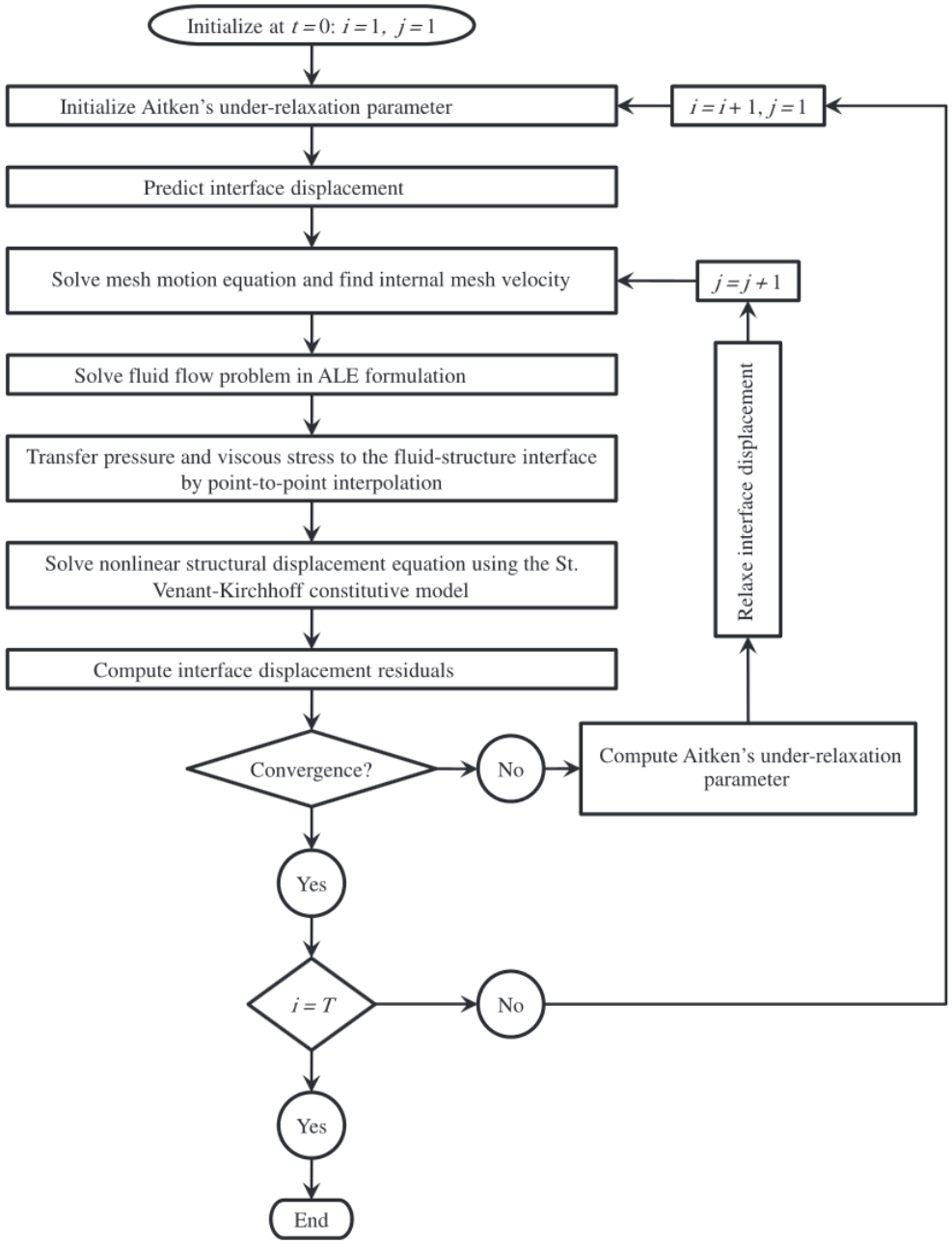

Figure 2.7: A simplified flow diagram of the presented solver includes the coupling loop.

coupling relaxation factor.

2.4 Main Parameters

Some physical parameters have a significant influence on the numerical solution of FSI cases, especially the cases concerning the deep water risers. These parameters will be presented in the following paragraphs.
Density ratio is one of the main parameters to be considered when an FSI case is investigated. The density ratio in this context means the ratio between fluid and structure densities. When this ratio is about 1, the strong coupling is needed and large deformation is expected, i.e. rubber and water. A term called mass ratio sometimes can be used instead or along with the density ratio. In the case of fully submerged bodies, there will be no value difference between either of the quantities.
Young's modulus of a structure is the parameter on which the initial expectations of the strain are made. Young's modulus can be determined by dividing the tensile stress by the extensional strain in the linear portion of the stress–strain curve. Poisson's ratio is an important parameter, which showed an influence during the numerical investigations of the present work. Poisson's ratio is defined by the ratio between the axial to transverse strains of the solid. The input of this quantity has an influence on considering the strain direction of a solid. Most of the used materials in the field of deepwater risers have a Poisson's ratio between 0.3 and 0.4. Decreasing such a ratio may bring stability to the numerical solution of an FSI case, but the results will not be valid.
Fluid physical properties have a major influence on the solution. The fluid viscosity is an important property which should be discussed. The initial influence which could be caused by fluid viscosity is on the value of Reynolds number. Furthermore, the most significant influence of such a physical quantity is on the value of shear forces of the fluid, which are transferred through the fluid-structure interface to the solid.

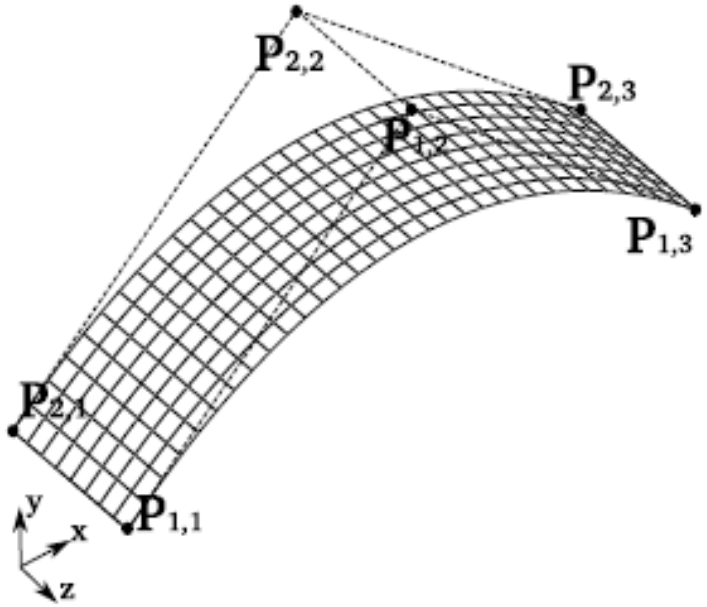

Figure 2.8: Reprinted from Becker et al. [57] shows the use of NURBS control points for surface optimization instead of using all the grid points.

2.5 Shape optimization and mesh-morphing dynamics

The interface surface is deformed at every time step and needs to be optimized in order to get the optimum solution time for both solvers participating in an FSI case solution.
Becker et al. [57] introduced a study on FSI shape optimization, depending on the main concept that the FSI shape optimization is a result of shape optimization of higher order surfaces accompanied by efficient time dependent optimization.
The obvious discrete approach which depends on the grid points as design variables costs more computational time for surface optimization than the developed approaches (e.g. the basis vector approach, CAD-based methods, polynomial and spline approach) which can reduce these design points in order to decrease optimization efforts. Instead of using whole grid points to relocate in order to optimize the surface, NURBS curves can be used which

depend on fewer design points, in other words they can be optimized using the so-called control points. According to Piegl [58] they are vector-valued piecewise rational polynomial functions.
Figure 2.8 shows the shape optimization using the location of control points only as a fast way. Becker's study concludes that this way is not only fast but gives high accuracy as well.
The velocity-based method of Laplacian smoothing was used for moving the mesh in the present study. This part of the presented solver was built based on the formulation of Laplacian smoothing in both papers of Tukovic et al. [59] and Lohner et al. [60].
To explain the fundamentals of finite volume FV mesh motion, the conservation mathematics of the static FV should be introduced as well. The static mesh FVM is mainly based on the integral form of the conservation equation over a control volume fixed in space. Figure 2.9 shows a graphical representation of a general finite volume cell [59].
The second-order finite volume discretization of the conservation law carries out a transformation of the surface integrals into sums of face integrals and makes an approximation of them to the second order by using the so-called mid-point rule [59]. The resulting mathematical formulation could be written as follows:

$$\frac{(\rho_P \Phi_P V_P)^n - (\rho_P \Phi_P V_P)^o}{\Delta t} + \Sigma_f \rho_f \left(F - F_s\right) \Phi_f = -\Sigma_f s_f \cdot \rho \mathrm{q}_\Phi + S_\Phi V_P \quad (2.40)$$

Where the subscripts P and f represent cell and face values respectively, and superscripts n and o represent the new and old time level respectively, while V is the volume, F is the fluid flux and F_s is the mesh motion flux. In this equation the F value is supposed to be obtained as a part of the solution algorithm. The obtained F value therefore must satisfy the conservation laws applied to its domain.

2.6 Linear systems solvers

The linear systems solvers are an input data in the OpenFOAM solvers. In the following subsections, the focus will be on those kind of solvers which are used in the processing of the study cases discussed in the present work.
GAMG solver: Geometric agglomerated algebraic multi grid solver (also named Generalized geometric-algebraic multi-grid in the manual) [75] can

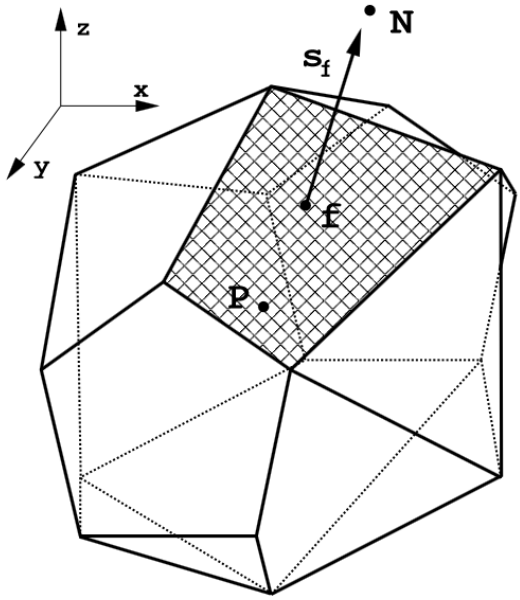

Figure 2.9: A finite volume cell (reprint from reference [59])

be the optimal choice for pressure field calculations [76]. GAMG uses the principle of: generating a quick solution on a mesh with a small number of cells; mapping this solution onto a finer mesh; using it as an initial guess to obtain an accurate solution on the fine mesh. Its aim is to be faster than standard methods when the increase in speed by solving first on coarser meshes outweighs the additional costs of mesh refinement and mapping of field data. The switching from a coarse mesh to the fine mesh is handled by the agglomeration of cells, either by a geometric agglomeration where cells are joined together, or by an algebraic agglomeration where matrix coefficients are joined.

smoothSolver solver: this uses a smoother for both symmetric and asymmetric matrices and is recommended for velocity field calculations.

PBiCG solver: this is a preconditioned bi-conjugate gradient solver for asymmetric matrices.

PCG solver: this is a preconditioned conjugate gradient solver for symmetric matrices.

A preconditioned iterative solver solves the system

M-1Ax = M-1b

where M is the preconditioner. The chosen preconditioner should make sure that convergence for the preconditioned system is much faster than for the original one. This leads to M (mostly) being an easily invertible approximation to "A".
All operations with M-1 should be computationally cheap. For multiplications with vectors the matrix-matrix multiplication M-1A does not have to be calculated explicitly, but can be substituted by two matrix-vector calculations. The above example was a left preconditioning, but central and right precondition also exist. In simple terms the preconditioner leads to a faster propagation of information through the computational mesh.
DIC solver: this is a simplified diagonal-based incomplete Cholesky smoother for symmetric matrices.

Chapter 3

The Numerical Code

In this chapter, a numerical solver for fluid-structure interaction is presented. Furthermore, some benchmark cases are computationally simulated and hence the results are analyzed in the sense of validation.
Pure water was considered to be the working fluid in all of the 3D simulations, while no other exceptions were written. The slandered physical properties of pure water are therefore considered.

3.1 Code Methodology and Implementation

This section focuses on the platform as well as the FSI solver. The platform (or in other words openFOAM C++ toolbox), on which the presented FSI solver was developed, has many facilities to be a good environment for the presented FSI numerical solution.

3.2 OpenFOAM Platform

OpenFOAM (***Open*** *Source* ***F****ield* ***O****peration* ***a****nd* ***M****anipulation*) is a C++ platform or toolbox for the numerical solvers of quantum mechanics problems, i.e. computational fluid mechanics. The platform has a wide range of utilities which are helpful for processing the preprocessing a computational case. It has an open-source license, which gives a good chance for developing specific solvers for special study cases.
By using the object oriented programming and the operator overloading, the implementation of the differential equations becomes easy enough to be

solved and enables the developers to establish or modify a solver.
Working on this platform is dependent on the concept of "low cost and high effort", so that many industrial firms and more scientific institutions world-wide use it for solving some specific cases.

3.2.1 Solver Implementation

This section will explain the main parts of the FSI solver, by which the cases in the present study were numerically investigated. The algorithms of solid and fluid domains as well as coupling are described.

Pressure and Velocity algorithms

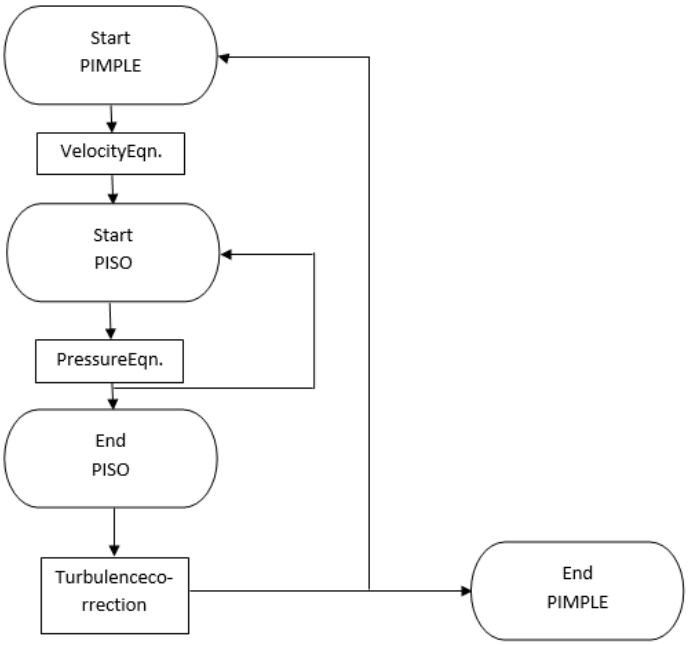

Figure 3.1: PIMPLE algorithm flow diagram.

The PIMPLE algorithm is used for coupling the pressure and velocity fields. It is a hybrid algorithm on which PISO and SIMPLE algorithms are merged. Figure 3.1 has a flow diagram showing the procedure of the PIMPLE loop, which is implemented in the solver.

Solid domain algorithm

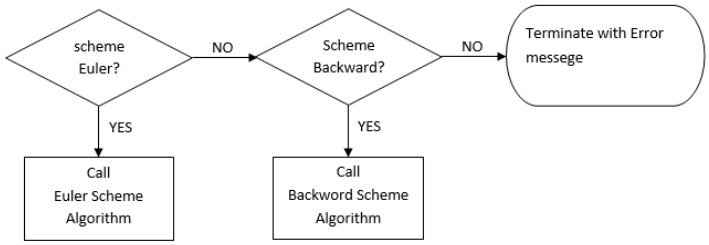

Figure 3.2: Solid solver algorithm flow diagram.

By using a finite volume method, the solution of the solid domain is determined. The solid solver has to obtain both solid domain deformations and velocities. The main file of solid solver will initially check the closed temporal derivation scheme. The solid solver algorithm then calls either the Euler or backward scheme solver. Both solver algorithms are typically the same but they differ in the way they deal with the results of the previous time-iteration. The main header algorithm of the solid solver is written as follows and figure 3.2 shows the flow diagram.

```
if (solidDdtScheme == fv::EulerDdtScheme$<$vector$>$::typeName)
{
   #   include "solveSolidEuler.H"
}

else if (solidDdtScheme ==
    fv::backwardDdtScheme$<$vector$>$::typeName)
{
   #   include "solveSolidBackward.H"
}
else
{
   FatalErrorIn(args.executable())
   << "Wrong temporal (ddt) scheme for solid solver. "
   << "Possible schemes are: "
   <<fv::EulerDdtScheme$<$vector$>$::typeName$<$$<$ " and "
   <<fv::backwardDdtScheme$<$vector$>$::typeName
   <<abort(FatalError);
```

```
}
```

Coupling

The most important part of any FSI or multi physics numerical solver is that part carrying out the information exchanges between the different physics domains, which is called coupling.
After calculating the needed values from the fluid solver, a code is used to set the forces for further transfer to the solid solver. The code part is written inside a header file called *setInterfaceForce.H*, which has also the task of calculating and writing out the total traction force, and is implemented as follows:

```
Info <<" Setting traction on solid patch "<<endl;
   vectorFieldfluidPatchTraction = -rhoFluid.value()*nu.value() *
       U.boundaryField()
   [fluidPatchID].snGrad();
   scalarFieldfluidPatchPressure =
       rhoFluid.value()*p.boundaryField()[fluidPatchID];
   vectorFieldfluidZoneTraction
   (
      mesh.faceZones()[fluidZoneID].size(),
      vector::zero
   );
   const label fluidPatchStart =
       mesh.boundaryMesh()[fluidPatchID].start();
   forAll(fluidPatchTraction, i)
   {
      fluidZoneTraction
          [mesh.faceZones()[fluidZoneID].whichFace(fluidPatchStart
          + i)
      ]=fluidPatchTraction[i];
   }
// For parallel processing: collecting pressure field on all
    processors
   reduce(fluidZoneTraction, sumOp<vectorField>());
   scalarFieldfluidZonePressure
   (
      mesh.faceZones()[fluidZoneID].size(),
```

```
      0.0
   );
   forAll(fluidPatchPressure, i)
   {
      fluidZonePressure
      [mesh.faceZones()[fluidZoneID].whichFace(fluidPatchStart + i)
         ]=fluidPatchPressure[i];
   }
// For parallel processing: collecting pressure field on all
    processors
   reduce(fluidZonePressure, sumOp<scalarField>());
   vectorFieldsolidZoneTraction =
       interpolatorFluidSolid.faceInterpolate
   (
      fluidZoneTraction
   );
   scalarFieldsolidZonePressure =
       interpolatorFluidSolid.faceInterpolate
   (
      fluidZonePressure
   );
   const label solidPatchStart =
       stressMesh.boundaryMesh()[solidPatchID].start();
   forAll(solidPatchTraction, i)
   {
      solidPatchTraction[i] =
      solidZoneTraction
   [stressMesh.faceZones()[solidZoneID].whichFace(solidPatchStart +
       i)];
   }
   forAll(solidPatchPressure, i)
   {
      solidPatchPressure[i] =
      solidZonePressure
   [stressMesh.faceZones()[solidZoneID].whichFace(solidPatchStart +
       i)];
   }
   if (fsi)
   {
      tForce.traction() = solidPatchTraction;
```

```
      tForce.pressure() = solidPatchPressure;
   }
   vectortotalTractionForce = gSum
   (
      solidPatchTraction
      *stressMesh.magSf().boundaryField()[solidPatchID]
   );
Info <<" Total traction force = "
   <<totalTractionForce<<endl;
```

Similarly, the header *setInterfaceDisplacement.H* sets the displacement on the interface. According to the preselected scheme of coupling, the code carries out its job. As mentioned, the presented mathematical modeling mainly depends on the Aitken scheme coupling method, but the solver can also work on a fixed relaxation coupling scheme. This header has been implemented as follows:

```
Info <<"\nTime = " <<runTime.timeName()
<< ", iteration: " <<outerCorr<<endl;
if (outerCorr< 3 ||couplingScheme == "FixedRelaxation")
{
   Info << "Current fsi under-relaxation factor: "
   <<fsiRelaxationFactor<<endl;
   fluidPatchPointsDisplOld = fluidPatchPointsDispl;
   fluidPatchPointsDispl += fsiRelaxationFactor*fsiResidual;
}
else
{
   if (couplingScheme == "Aitken")
   {
      fsiRelaxationFactor = -fsiRelaxationFactor
         *(gSum(fsiResidualOld &(fsiResidual -
      fsiResidualOld))/(gSum((fsiResidual -
         fsiResidualOld)&(fsiResidual - fsiResidualOld))));
      fsiRelaxationFactor = mag(fsiRelaxationFactor);
      Info << "Current fsi under-relaxation factor (Aitken): "
      <<fsiRelaxationFactor<<endl;
      fluidPatchPointsDisplOld = fluidPatchPointsDispl;
      fluidPatchPointsDispl += fsiRelaxationFactor*fsiResidual;
   }
```

```
}
```

Because of mesh issues and its dynamic nature, the values around the interface have to be interpolated to achieve the proper motion. The header *createZoneToZoneInterpolators.H* has the task of creating such interpolators.

3.3 Validation

Unlike the previous sections, this section discusses the numerical results when compared with the published experimental and numerical benchmarks. The validation cases were simulated under the environmental conditions to give a reasonable and fair comparison. The presented fluid-structure interaction solver as well as fluid part of it with respect to the turbulence different models were validated and compared.

3.3.1 Validation of the fluid structure interaction solver

In this section two benchmarks have been used for preforming the validation. As it had been discussed by Ricardo et al.[77], a validation of an numerical solver could be carried out by several methods. In This dissertation, two different validation methods have been used. A well-known numerical benchmark of a lid-driven cavity attached with a flexible bottom was considered. Furthermore, a fundamental flexible cantilever fluid-structure case have been compared with published experimental results.

Validation using an experimental benchmark

In this section a computational simulation of a flexible vertical cylindrical cantilever had been carried out. The following figure 3.3 shows the geometry of the cantilever and the boundary conditions. The main dimensionless parameters of design and material are listed in table 3.1. The values and geometry have been determined depending on the experiment of Franzini, which is described in details in his published paper [66]. Two values of reduced velocity had been considered for validation. The reduced velocities of 3.69 and 6.03 had been selected for the mentioned benchmark case experiments.
According to figure 3.3 the following design parameters were considered.

$S[mm]$	$D[mm]$	$L/D[-]$	$m*[-]$	$f1[Hz]$	$EI[Nm^2]$
305	25.4	35.5	1.2	1.17	5.20

Table 3.1: The design and material parameters of the flexible cantilever validation case. Where S, D, L, $m*$, f1 and EI are the distance between cantilever moving end and the bed of the water tank, the cantilever diameter, the cantilever length, the mass ratio $m*$ = the mass of oscillating body divided by the mass of displaced fluid, the first natural frequency and the bending stiffness respectively.

Mesh and discretization

For avoiding the discretization error, a mesh dependency test had been carried out. The maximum value of displacement of the cantilever tip midpoint had been regarded for the test. The fluid domain had been divided into 404752 *hexahedrons* and 38720 *polyhedrons*. The OpenFOAM meshing tool *snappyhexmesh* had been used for the meshing of the fluid and solid domains. The following figure 3.4 shows the used mesh in some sectional views.

Results

As mentioned, the results are compared to the experimental work of Franzini for the aim of validation. The following tabels 3.2 and 3.3 are showing that comparison. Furthermore, following figure 3.5 is showing the status of fluid flow around the flexible cantilever.

	$v* = 3.69$	$v* = 6.03$
Present work	0.13	0.54
Franzini[66]	0.11	0.52

Table 3.2: The present results of the ratio Y/D between the maximum displacement of the cantilever tip in y-direction Y and the cantilever diameter D (see figure 3.3) with respect to the reduced velocity compared to the Franzini experimental results.

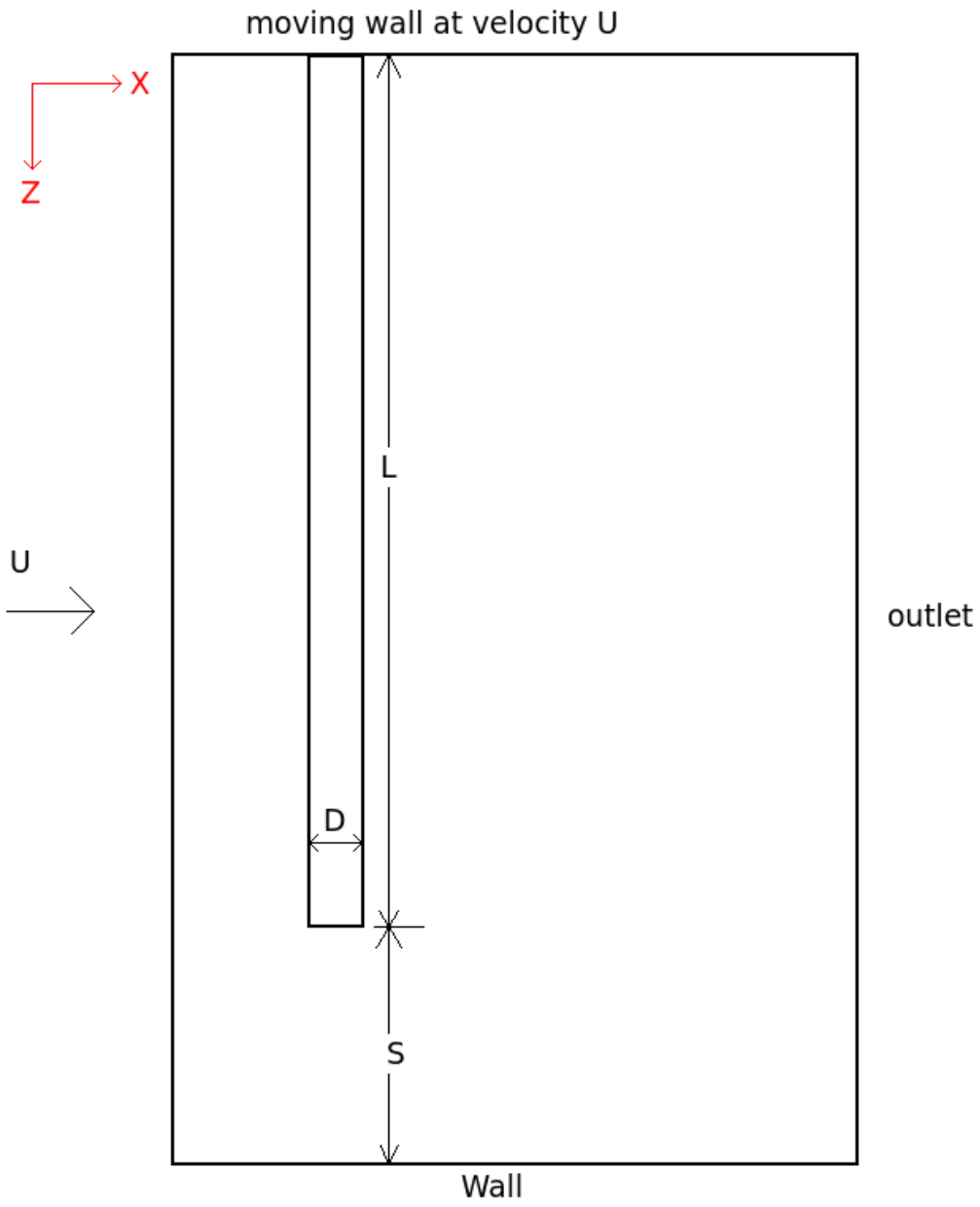

Figure 3.3: The geometrical representation of the validation case of a flexible circular cantilever subjected to a water cross flow at velocity U. The size of the computational domain was considered to be 1.5S, S and L+S in x, y and z directions respectively.

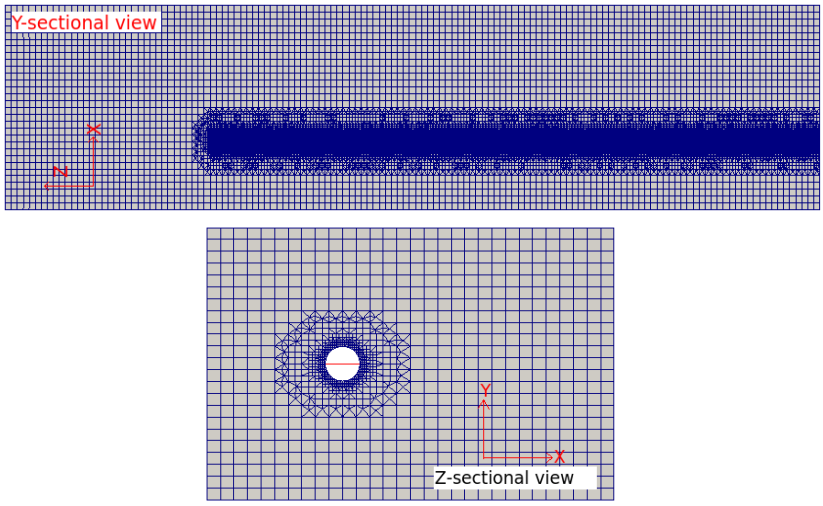

Figure 3.4: The used meshing for the validation case of a flexible cantilever at different sectional views.

	$v* = 3.69$	$v* = 6.03$
Present work	0.11	0.31
Franzini[66]	0.09	0.28

Table 3.3: The present results of the ratio X/D between the maximum displacement of the cantilever tip in x-direction X and the cantilever diameter D (see figure 3.3) with respect to the reduced velocity compared to the Franzini experimental results.

The reduced velocity is expressed as $v* = \frac{U}{f1D}$, where U is the flow velocity at inlet , f1 is the first natural frequency of the cantilever and D is the cantilever diameter.

Validation using a numerical benchmark

Case setup

One of the most common cases for fluid-structure interaction solvers validation is the 2D lid-driven cavity with flexible membrane at the bottom side.

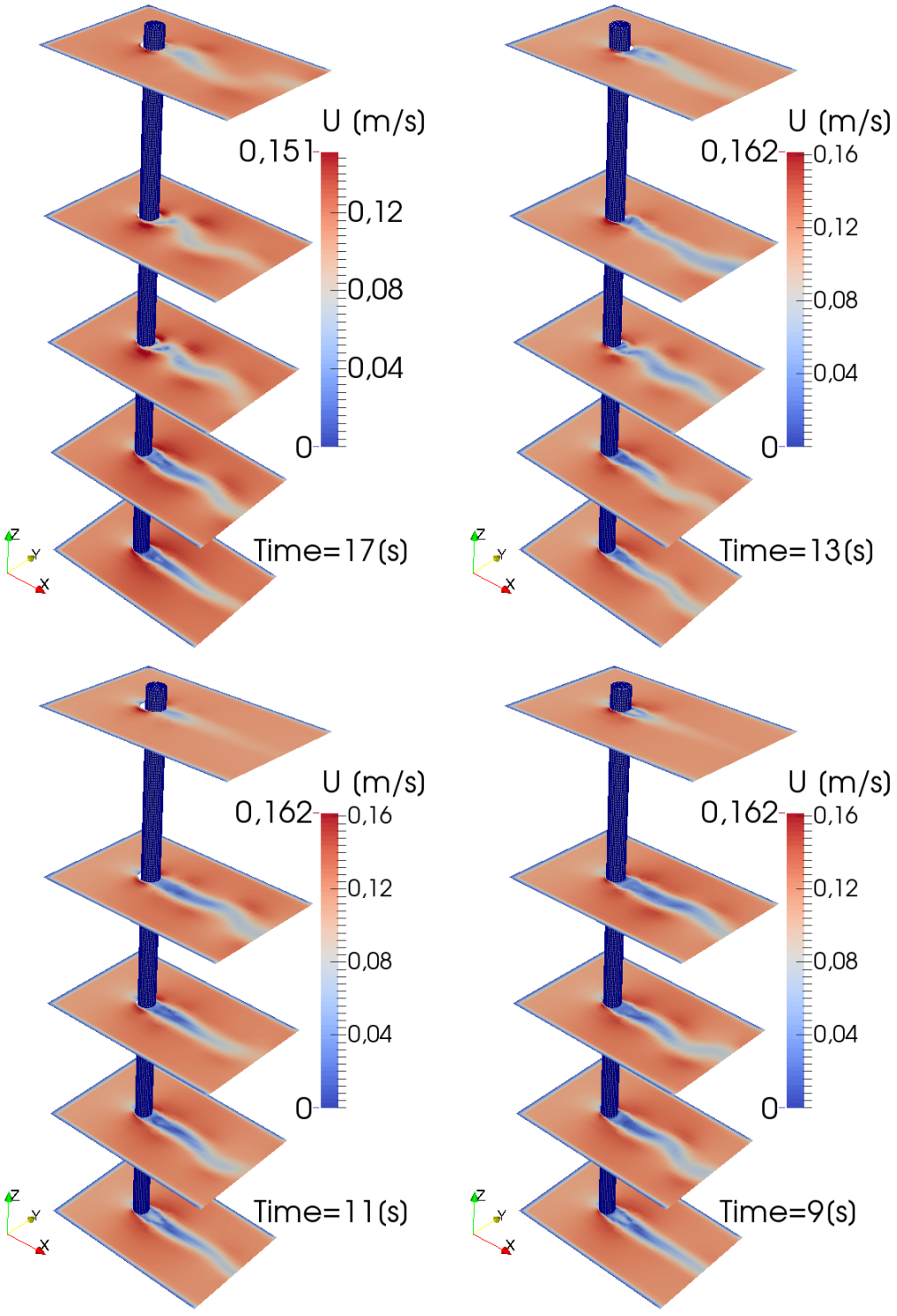

Figure 3.5: The velocity contours at different section and times of the validation case of flexible cantilever

Figure 3.6 shows the fluid and solid domains and gives information about boundary conditions and dimensions.
The case could be described as a square cavity filled with air and has an elastic membrane at its bottom. This membrane is excited by a fluctuating velocity at the upper moving wall. The velocity of the upper wall is governed by the following relation:
$u_x\,(t) = 1 - \cos(\frac{2\pi}{5}\ \mathrm{t})$

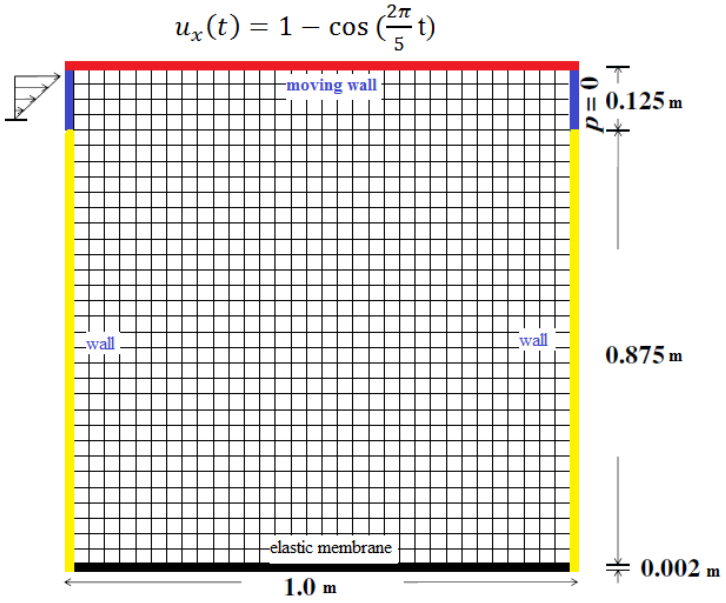

Figure 3.6: The geometry and mesh of lid-driven cavity validation case.

This shafted cosines velocity function in time will lead to the velocity fluctuation value between 0 and 2 m/s, which gives a Reynolds number fluctuation between 0 and 200.
The material of membrane has a density of 500 kg/m^3, a Poisson ratio of zero and a Young's modulus of 250 Pascal. Air is used for the fluid domain and has a density of 1 kg/m^3 and a kinematic viscosity of 0.01 m^2/s.
During the solution the time step was fixed to 0.01 seconds, which gives an average CFL number (Courant–Friedrichs–Lewy number) of one. It is observed that the mentioned time step and the CFL resulting number gave the best stability to the solver for this test case.
The pressure equation was solved using a generalized geometric-algebraic multi-grid (GAMG) solver and its convergence criterion was fixed to 10^{-7},

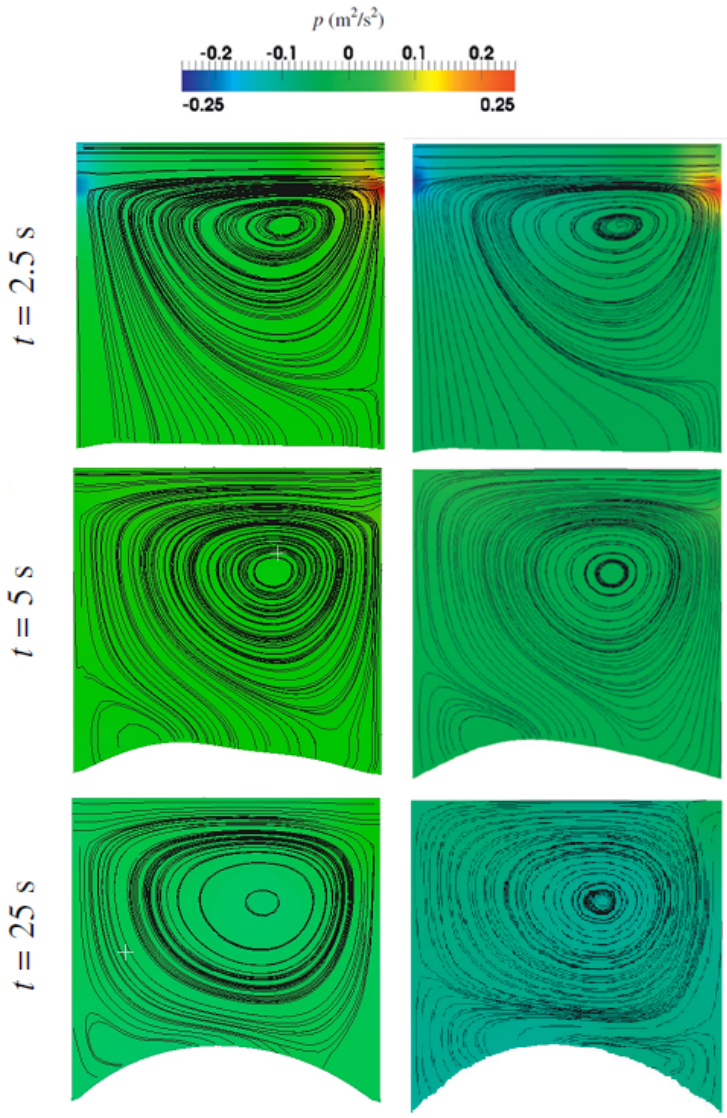

Figure 3.7: Stream lines results on pressure contours of lid-driven cavity test case. Present work (right) and Habchi et al. [48] (left).

while the velocity equation used the same solver and convergence criterion. The outer corrector loops of PIMPLE algorithm were set to 20. The mesh motion solver was GAMG as well, and used convergence criterion of 10^{-8}. Moreover, the Incomplete Cholesky Conjugate Gradient (ICCG) solver was used for the solid displacement equation solution with a convergence criterion of 10^{-8}.

Mesh and discretization

The mesh dependency test led to a 32×32 cells mesh for the fluid domain and 64×1 cells mesh for the solid domain. The mesh independence check was carried out with regard to med-point displacement in the direction perpendicular to the moving plate.
The following table 3.4 presents the results of the fluid domain mesh independence check and the considered mesh.

Mesh size	*Max. displacement of the membrane med-point in the y-direction [m]*
16×16	0.11
28×28	0.18
30×30	0.19.5
32×32	0.21
40×40	0.21

Table 3.4: The results of the fluid domain mesh independence check for the case of lid-driven cavity with flexible bottom

Results

Figure 3.9 represents a comparison between present results and the published results of Habchi et al. [48]. The results indicate the stream lines at different time steps on the pressure contours. As shown in the figure, both results give a good visual agreement, when the deformation of mesh is also observed. As the figure 3.9 shows, the time history of displacement in y-direction of the mid-point of the elastic bottom shows a good agreement with the other published results. Moreover, figure 3.8 shows the moving wall velocity time history along with y-displacement.

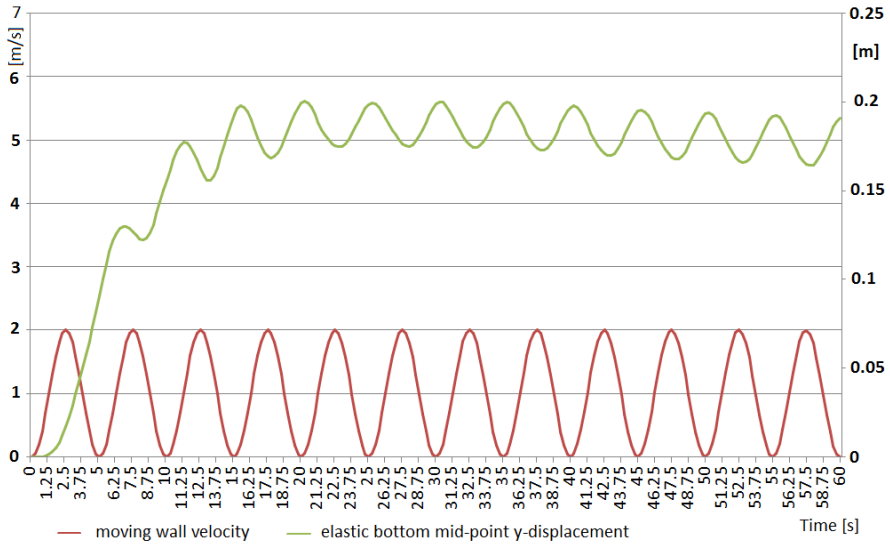

Figure 3.8: Time history of moving wall velocity as well as elastic bottom mid-point y-displacement.

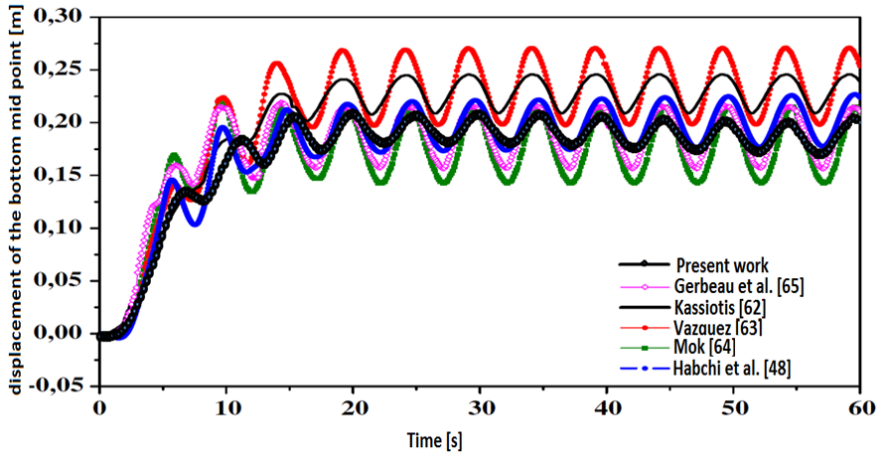

Figure 3.9: A comparison between the results of lid-driven cavity with flexible bottom and the published benchmark[48].

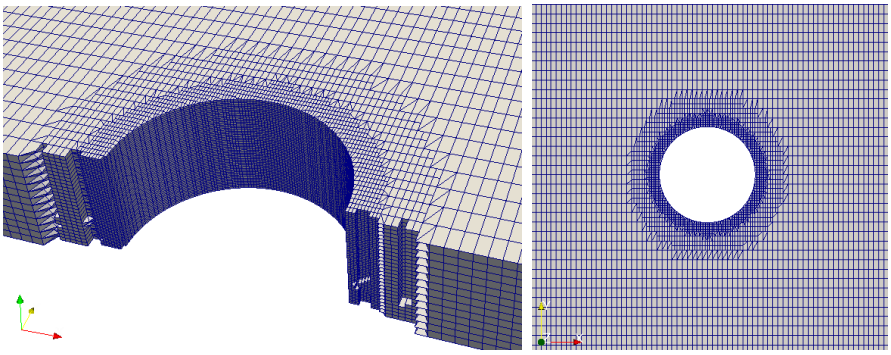

Figure 3.10: Different sectional views of the mesh used for all simulations.

3.3.2 Validation of the fluid part of the solver

The main goal of this section is validating the fluid part of the presented solver by using different turbulence models. A fair comparison of the results with each other and versus the published works has preformed the aimed validation and hence justifies the selection of the LES turbulence model. As the short aspect ratio principle has been successfully simulated and validated in the work of Chen et al. [67], the current cases were also modeled based on a short aspect ratio under the same conditions of the mentioned reference. Despite considering a short aspect ratio, the flow changes in axial direction of the cylinder could be captured (see figure 3.17).

Case setup

This section has a study case of a stationary circular cylinder with aspect ratio L/D=0.5, while the diameter D=0.025 meters is subjected to a cross-water flow at Reynolds number of $0.85X10^5$ based on the cylinder diameter. Regarding the aspect ratio of L/D = 0.5, it is considered to be sufficiently large to capture relevant spanwise wake effects. The only available access to computational resources is limited, which precludes simulations with a larger spanwise length with adequate spanwise resolution.
The computational domain, boundary conditions and meshing are common for the considered turbulence models, which are LES, S-A and S-A IDDES.

Mesh and discretization

Figure 3.10 shows the meshing used in different sectional views. The mesh consists of 449488 cells and 437406 nodes. The simulation was carried out on 16 processors in parallel. The number of nodes showed acceptable mesh independence check results. Figure 3.11 shows the results of the mesh independence check and shows that the mesh independence investigation was carried out on the mean value of the drag coefficient of LES results.

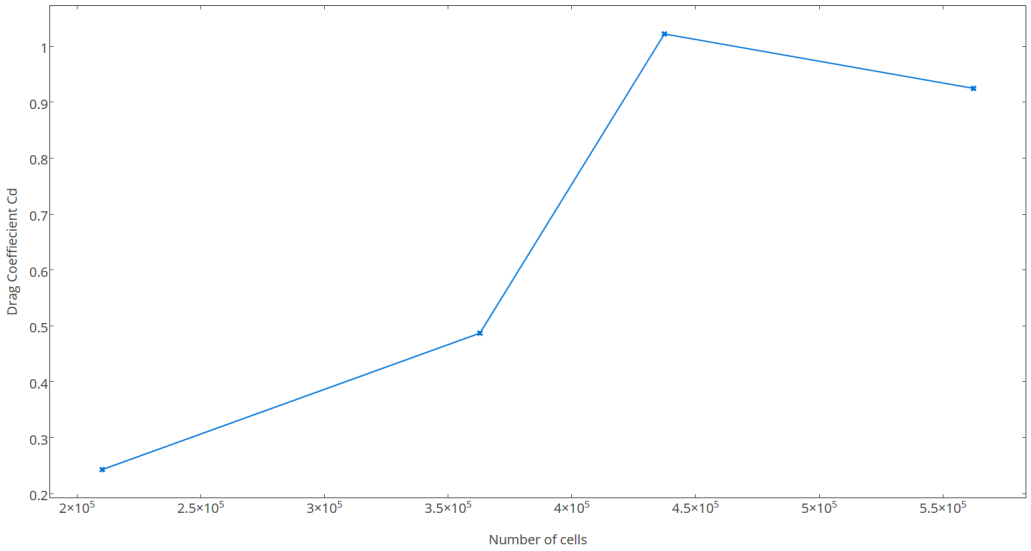

Figure 3.11: The results of the mesh independence check of the validation case of the fluid part of the solver depending of the mean value of drag coefficient $C_D = \frac{2F_D}{\rho U^2 A}$.

Results

Figures 3.14, 3.15 and 3.16 show the pressure coefficient according to the angular position on the cylinder surface at aspect ratio L/D=0.25 for the turbulence models LES, S-A IDDES and Spalart-Allmaras respectively. The figures present the results at different dimensionless time values D/U. The pressure coefficient has been calculated as $C_p = \frac{p-p_\infty}{\frac{1}{2}\rho_\infty U^2}$ where p is the pressure on the cylinder surface, p_∞ is the free stream pressure, ρ_∞ is the free stream density.
As expected, the large-eddy simulation shows an unsteady high 3D changing

flow. Unlike large-eddy simulation, the SA-IDDES and SA show a semi-steady flow and much less vorticity compared to LES. Figure 3.17 shows the flow as computed by LES. Figure 3.13 presents the time history of drag and lift coefficients of LES simulation. The drag and lift coefficients have been calculated as $C_D = \frac{2F_D}{\rho U^2 A}$ and $C_L = \frac{2F_L}{\rho U^2 S}$ respectively, where F_L is the lift force,F_D is the drag force, A is the reference area of the obstetrical, and S is the relevant plan area of the obstetrical.
A fair comparison and overview could be achieved by presenting graphical results. Figure 3.12 therefore presents graphically a comparison of the published results versus the present study.

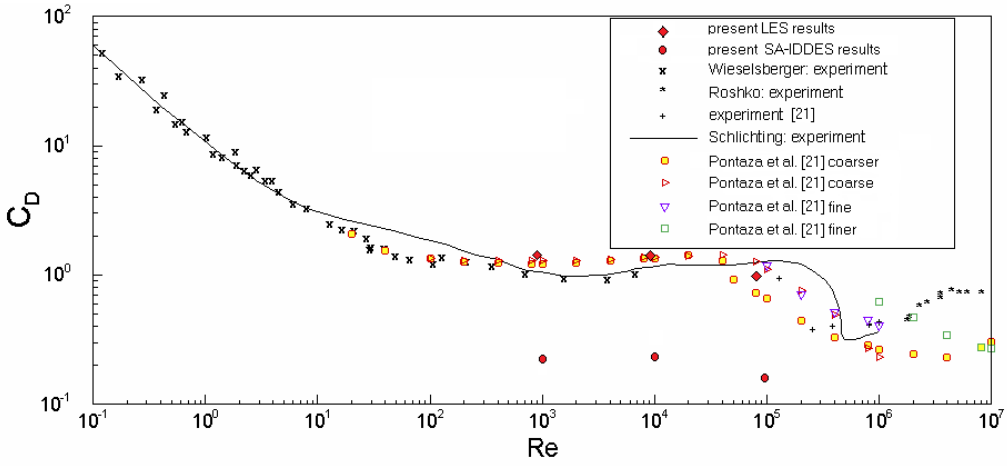

Figure 3.12: Time-averaged drag coefficient vs. Reynolds number curve of the published numerical and experimental results [67] compared with the present results.

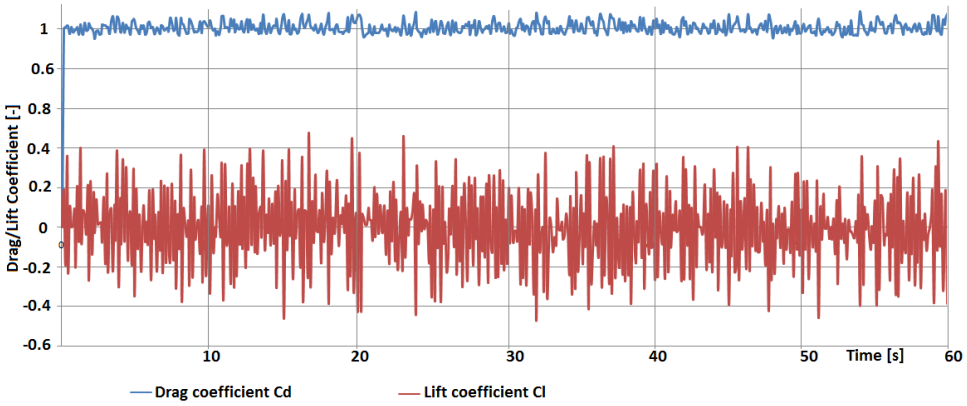

Figure 3.13: Drag and lift coefficients time history for LES results.

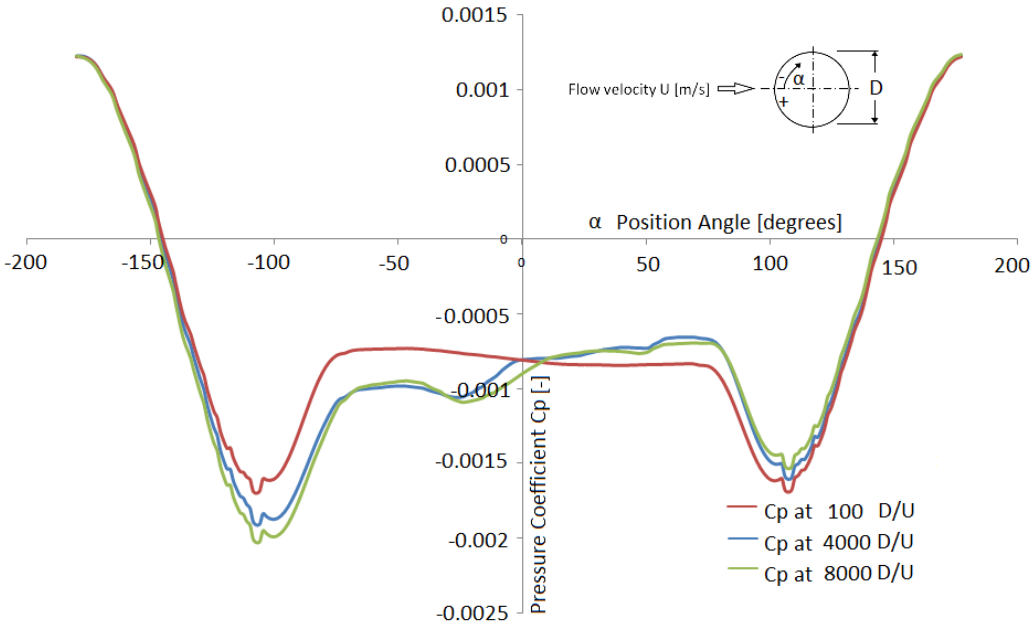

Figure 3.14: Large-eddy simulation results of pressure coefficient on surface at L/D=0.25 at different dimensional time values D/U.

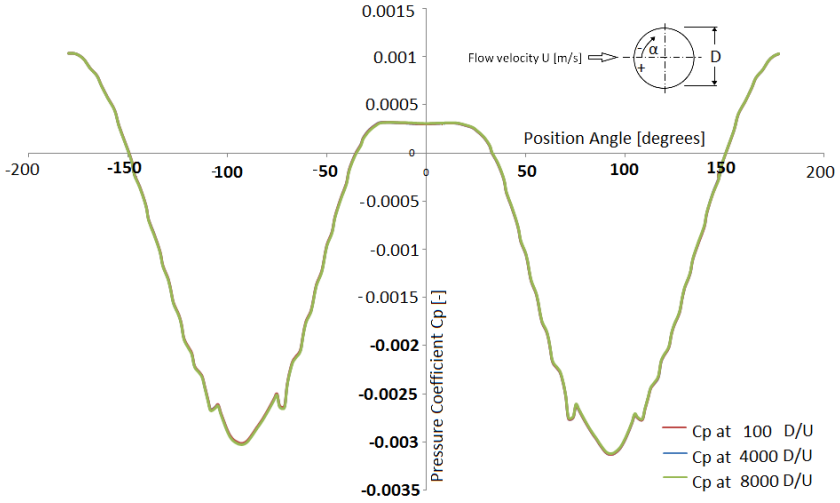

Figure 3.15: S-A simulation results of pressure coefficient on surface at L/D=0.25 at different dimensional time values D/U.

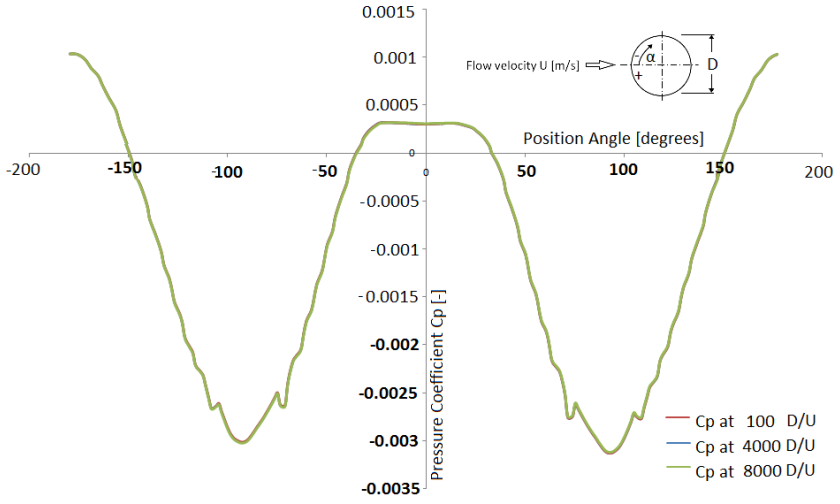

Figure 3.16: Spalart-Allmaras improved delayed detached eddy simulation results of pressure coefficient on surface at L/D=0.25 at different dimensional time values D/U.

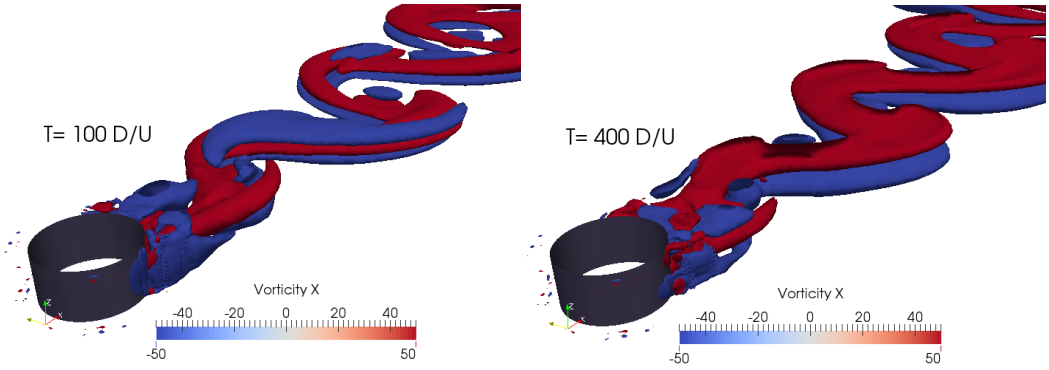

Figure 3.17: Vorticity iso-surfaces for the flow past the cylinder at different time steps. D and U are the cylinder diameter and velocity at inlet respectively.

3.4 Discussion

In this section the results which were presented in the foregoing sections are discussed. The conclusions regarding these results are namely mentioned in this section.

3.4.1 Results of fluid-structure interaction solver validation

As a validation case, the presented solver was used to investigate an elastic cantilever subjected to cross-flow at high Reynolds number of 10^4. The results showed the details of the vortex shedding in the downstream. The results were compared to the published experimental benchmark and demonstrated good agreement. The VIV amplitude responses showed good agreement with the published experimental results of Franzini et al. [66] (Tables 3.2 and 3.3).
A selected numerical benchmark of a lid-driven cavity attached to elastic membrane at the bottom side and upper moving wall was considered for validation. The results of this validation case were compared to some of the published numerical results and showed good agreement (figure 3.9).

3.4.2 Results of fluid part validation

Three turbulence models were subjected to fair comparison to each other and versus the published experimental results (figures 3.14, 3.15 and 3.16). The same meshing and numerical domains were used over all three simulations. The following observations were able to be made:

1. It was clear that the LES model expresses good agreement with experimental results (figures 3.12 and 3.14).

2. Both SA-IDDES and SA did not result in good agreement for the same conditions under which the LES had been solved (figures 3.12, 3.15 and 3.16).

3. The simulation time of SA-IDDES is much higher than SA and LES, while the same number of processors was used for all.

4. An observable difference did not exist between SA and SA-IDDES, in terms of results (figures 3.15 and 3.16).

The LES therefore is highly recommended for solving deepwater risers' cases using OpenFOAM.
The LES gave a 60 seconds averaged drag coefficient C_D=1.02 which shows good agreement with Pontaza et al. [67] and fair agreement with the experimental results of Schewe [68] and Achenbach [69]. Furthermore, the root mean square of lift coefficient $C_{L,RMS}$=0.2 shows fair agreement with the experimental results of Norberg [70]. Figure 3.13 shows the drag and lift coefficients time history of LES.
Unlike LES, both SA-IDDES and SA showed bad agreement to the published numerical and experimental results. Figure 3.12 presents a comparison of published numerical and experimental results versus the present study.
Because of the limited resources for performing the computational effort, a small sized computational domain had been used. A mesh dependency test had been carried out to ensure that the considered low number of cells had given results with good quality.

Chapter 4

The Effect of Geometry on VIV

This chapter is going to present numerical investigations about the phenomenon of vortex-induced vibrations. The presented results give more understanding about the effect of design shapes and parameters on the suppression of the resulted vibrations and forces acting on the obstacle.

4.1 Adding strakes

Adding strakes to a cylindrical shape obstacle may reduce the vortex-induced vibrations. The main function of the straked shape is that it reduces the continual flow separation points relocation. As a wide used solution for vortex-induced vibrations in deep water risers, the straked shape was presented.
Two study cases have been investigated to prove this fact and bring more understanding to the effect of the shape on the vortex-induced vibrations suppression. The presented tool of fluid-structure interaction has been used to preform the both simulations. The operating conditions are set to be identical for both cases.
The mentioned cases have a cantilever geometry. The considered cantilevers are cylindrical with free end and subjected to a water cross flow. One of the cases has straked cantilever with the design parameters shown in the table 4.1, which additionally contains the information about material and flow conditions. As shown in the following table, the only difference between the two present modelings is the adding of strakes. This procedure brings a fair comparison and presents understanding to the shape influence on vortex-induced

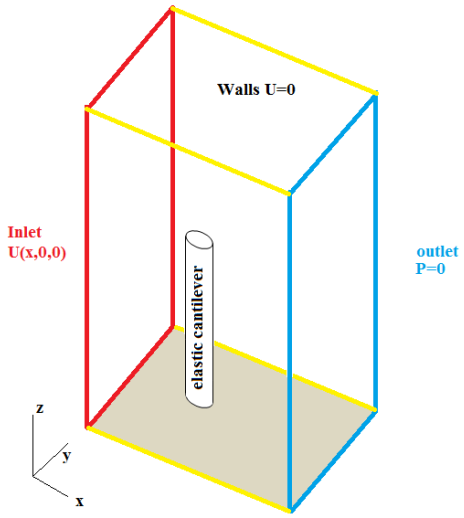

Figure 4.1: An isometric view of the elastic cantilever study case, showing both fluid and solid domains as well as the considered boundary conditions.

vibrations suppression.

-	material	Reynolds number	Pitch	number of strakes	Height of strakes
plain shape	PVC	10^4	-	-	-
straked shape	PVC	10^4	15D	3	0.2D

Table 4.1: The design parameters and operating conditions of the two considered cantilevers. D is the diameter of the considered cylindrical cantilever.

4.1.1 Plain Shape

Case setup

This study case was considered to be an elastic circular cantilever subjected to a cross pure water flow. The elastic cantilever is made from Polyvinylchloride (PVC). Figure 4.1 shows the geometry used for both solid and fluid computational domains in an isometric view. It also shows the considered boundary conditions. The height of the elastic cantilever is 0.45 meters, while its radius is 0.0127 meters and it is considered to have a completely fixed bottom,

which means that the aspect ratio L/D is 17. Moreover, the fluid domain is 0.3 meters long in x-direction, 0.2 meters wide in y-direction and 0.7 meters height in z-direction. The center line of the elastic cantilever is mounted at 0.1 meters in x-direction from inlet and on the exact mid-point between side walls in y-direction. Figure 4.2 shows the meshing used in both sections at z=0.15 meters from the bottom wall and at y=0.1 meters from the side wall.

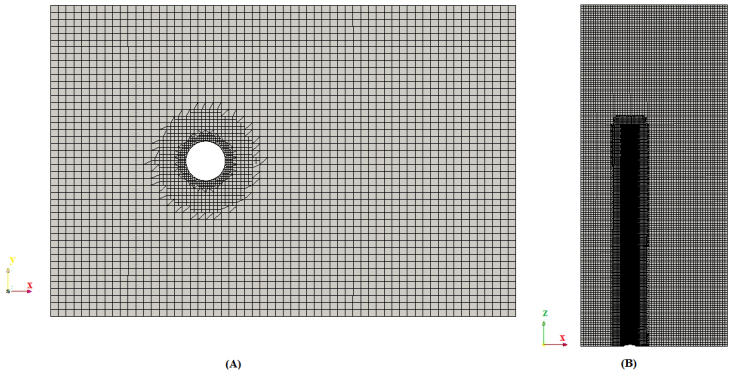

Figure 4.2: Sections at z=0.15 meters from the bottom wall (A) and at y=0.1 meters from the side wall (B) in the mesh of the fluid domain.

The fluid is pure water with a density of 1000 kg/m^3 and a kinematic viscosity of 10^{-6} m^2/s flows at 0.34 m/s, which results in a flow of Reynolds number 10^4 around the elastic circular cantilever. The elastic cantilever is made from Polyvinylchloride of Young's modulus 1.5X10^9 Pascal and density 1500 kg/m^3 as well as a Poisson's ratio of 0.4. The numerical solution of all equations used the same configurations as the foregoing validation case of lid-driven cavity. The fluid domain was solved using one equation unsteady large eddy simulation (LES).

Mesh and discretization

Because of the available limited computing unit, a relatively small fluid domain was considered. Moreover, the computational model was discretized to have 641598 cells in the fluid domain and 4800 cells in the solid domain. This mesh size produces a small change in results after more refinement. Figure 4.3 gives the results of a fluid mesh independence check, which was done depending on maximum dimensionless displacement of the mid-point on the cantilever free end in y-direction. Furthermore, figure 4.2 presents

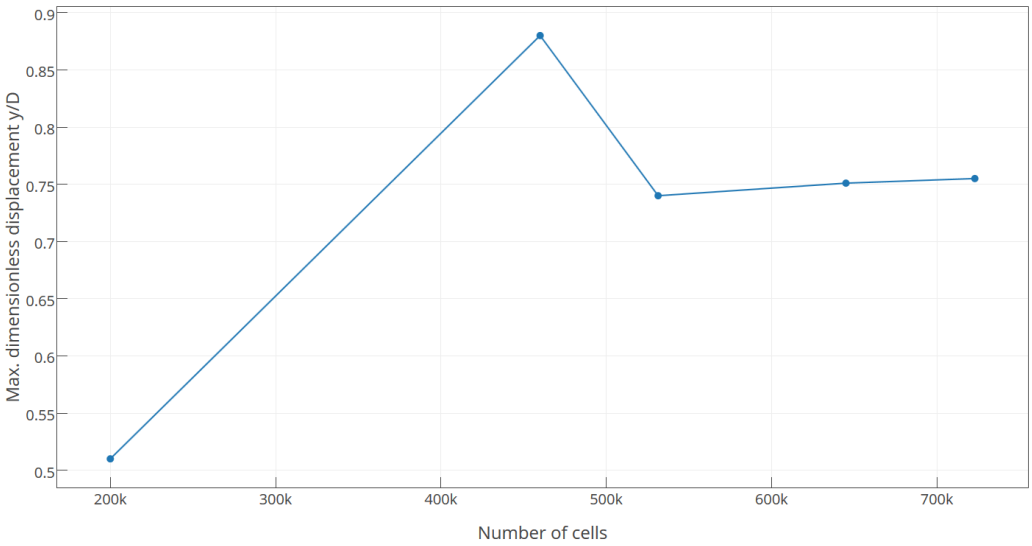

Figure 4.3: Mesh dependency test results for the fluid-structure interaction simulation of the plain shape.

some sectional views to the fluid mesh.
The tools *snappyhexMesh* and *blockMesh* were used for mesh generation depending on the imported STP file.

Results

Figure 4.4 shows three-dimensional contours of pressure in wake zone. The contours results at different time steps show the vortex shedding behind the

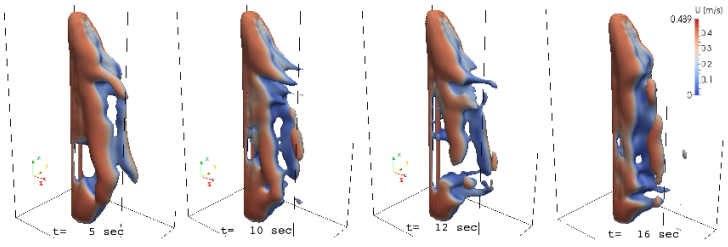

Figure 4.4: Three-dimensional pressure contours in wake zone at different time steps and colored by velocity values for the bar cantilever case.

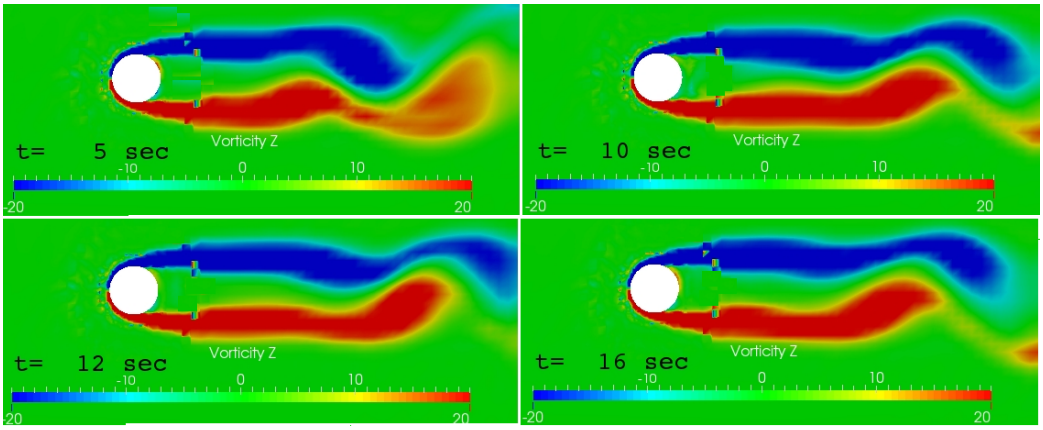

Figure 4.5: Vorticity contours at z=0.2 meters from the bottom wall at different time steps.

elastic cantilever and colored by velocity values. Moreover, figure 4.5 shows the two-dimensional vorticity contours at z=0.2 meters from the bottom wall. The 2S vortex pattern could be observed from both mentioned figures.

4.1.2 Straked shape

Case setup

The considered case of a straked flexible cantilever subjected to a water cross flow has the same design and operational parameters as the foregoing case of a bar cantilever. The only difference between both designs is adding the strakes to the cantilever. The geometry of the cross sectional shape of the staked cantilever is showed in the figure 4.6. Same to the foregoing case, the straked cantilever has a free and fixed ends as well.

Mesh and discretization

As done in the foregoing cases, a mesh independence test has been carried out to ensure the accuracy of results in terms of discretization error. The considered fluid domain consists of 548085 tetrahedral cells. The mesh dependence test has been carried out depending on the value of y/D, which shows the stable value of 0.21 at the mentioned number of cells. The following figure 4.7 shows the used mesh in different cross sectional views.

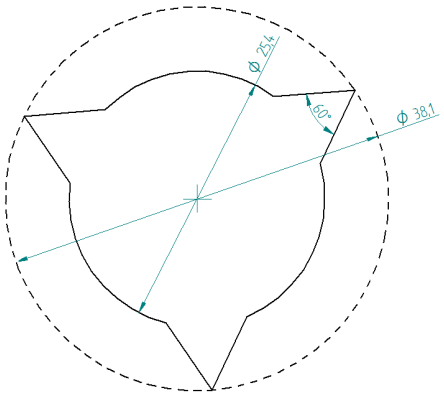

Figure 4.6: A cross sectional view of the considered geometry of the staked flexible cantilever case (all dimensions in [mm]).

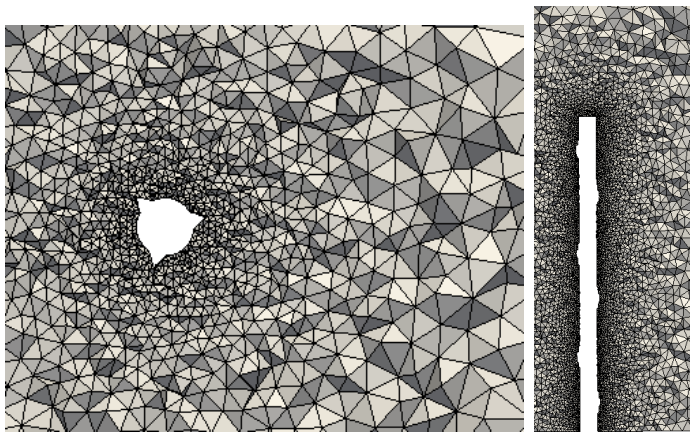

Figure 4.7: Different cross sectional views of the considered mesh of the staked flexible cantilever case.

Results

In the following figures, the comparable results are showed. In figure 4.8, the three dimensional pressure contours of the flow around the cantilever at different times are presented and colored with velocity values. The mentioned three dimensional pressure contours give a good visualization of the wake

zone in down stream.
In the figure 4.9, the vorticity contours at different times are showed. The vorticity around z-direction is considered, as it represents the more important parameter regarding the topic of research and to give the chance for fair comparison.
The results of both cases of plain and straked shaped cantilevers are post processed in the same way to give the reader a suitable ability for a visual comparison.

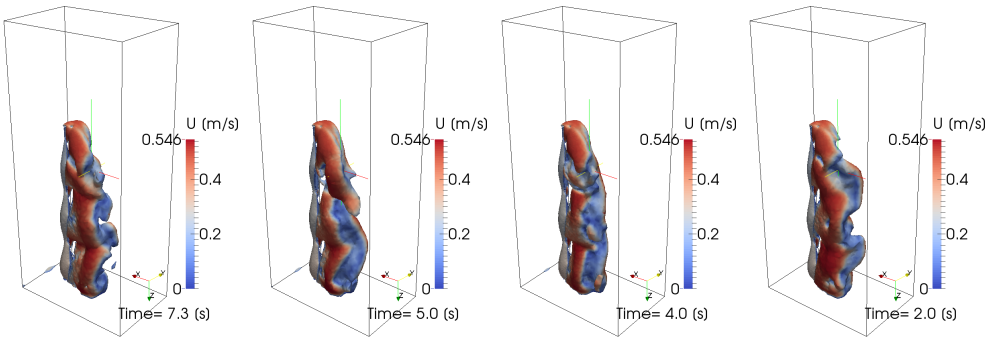

Figure 4.8: Three-dimensional pressure contours in wake zone at different time steps and colored by velocity values for the straked cantilever case.

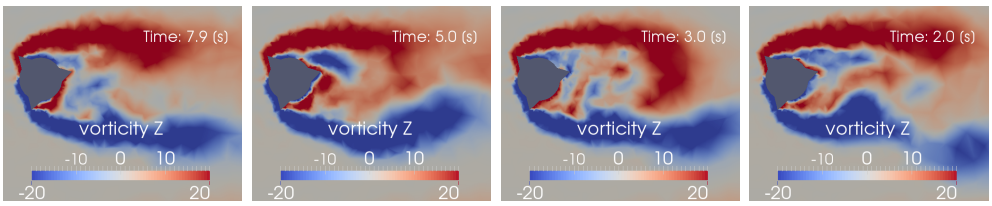

Figure 4.9: Vorticity contours at z=0.2 meters from the bottom wall at different time steps for the straked cantilever case.

4.2 Strakes design parameter

As discussed in the foregoing part of the present chapter, adding strakes to an obstacle is helping to reduce the vortex-induced vibrations. Changing a design parameter of the considered design may help as well. In the present section, a straked shape of a rigid obstacle is considered. By using the fluid

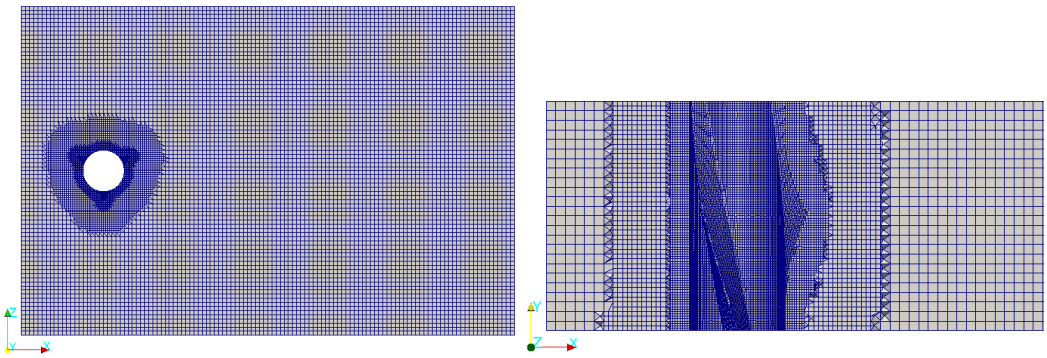

Figure 4.10: Different cross sectional views of the considered mesh of the staked rigid cylinder case at pitch=15D.

dynamics part of the presented tool, the forces and wake as well as the shape of down stream flow are discussed. The selected design parameter is the pitch of the helical shape of strakes.

Case setup

A straked shaped cylindrical obstacle has been subjected to a water cross flow. The operational conditions are same as the foregoing flexible cantilever case. The strakes geometry is identical to the described shape in figure 4.6. The pitch of strakes varied between 1D to 17D with an increment of 2D.

Mesh and discretization

All cases have been subjected to a mesh independence test. Depending the maximum value of lift coefficient, the mesh independence test has been carried out. The used meshes have a number of cells around 0.5 million, which are determined by performing a mesh dependency tests for each case. The figure 4.10 shows the used meshing in different views.

Results

Figure 4.11 shows the change of the both time averaged drag and lift forces with respect to pitch of strakes. For better visual conclusion, a linear values

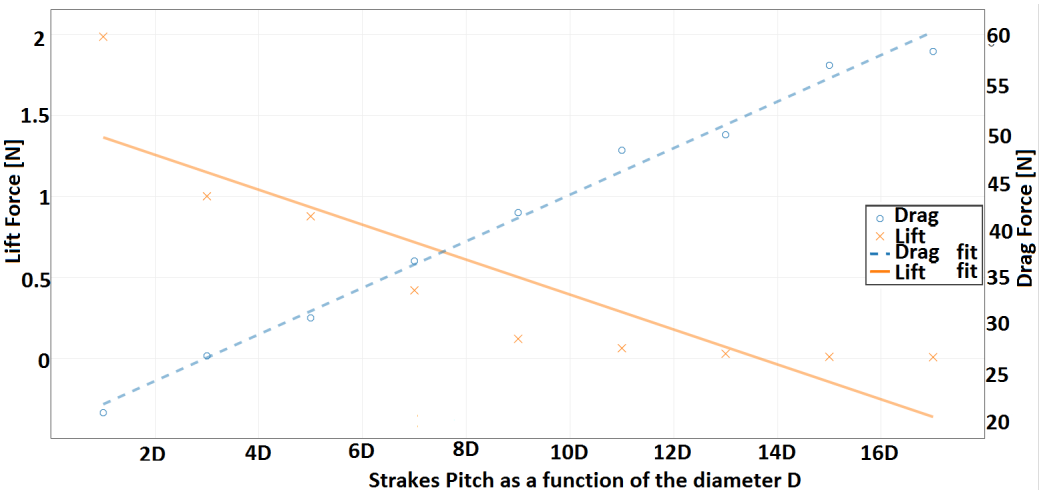

Figure 4.11: The time averaged drag and lift forces in Newtons with respect to stakes pitch.

fitting has been added to the diagram.
Figure 4.12 shows the velocity contours at different pitches values. The results were taken at the time step, which represents the steady state of wake flow behind the obstacle.
Figure 4.13 shows the vorticity around y-direction, which is the the perpendicular direction to the figure. The shown contours are taken at the time step, which represents the steady state of wake flow behind the obstacle. The results give a good visual representation to the vortex shedding of downstream flow.

4.3 Conclusions

In the foregoing sections, two study cases were numerically investigated. The two considered cases were modeled to be similar in terms of operating conditions. The addition of strakes to the surface of a flexible cantilever was modeled to give the chance for evaluating the effect of geometry on the vortex-induced vibrations.
The results are shown in the way to be easy for a visual comparison. The main measurements are showed in several graphical representations.
The straked cantilever showed a reduced y/D value. By comparing the max-

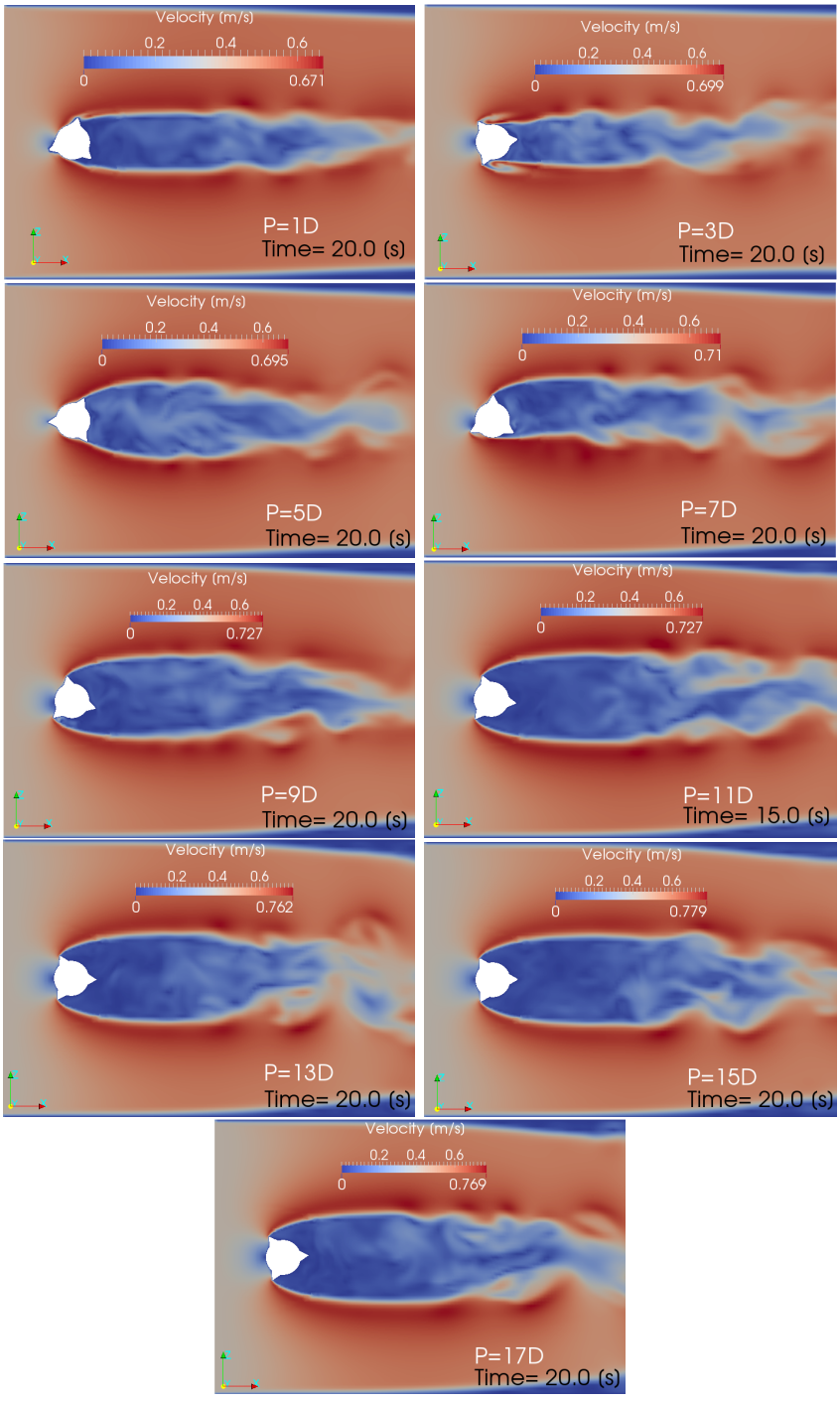

Figure 4.12: The flow velocity contours at different stakes pitches taken at a slice on the mid point y-direction.

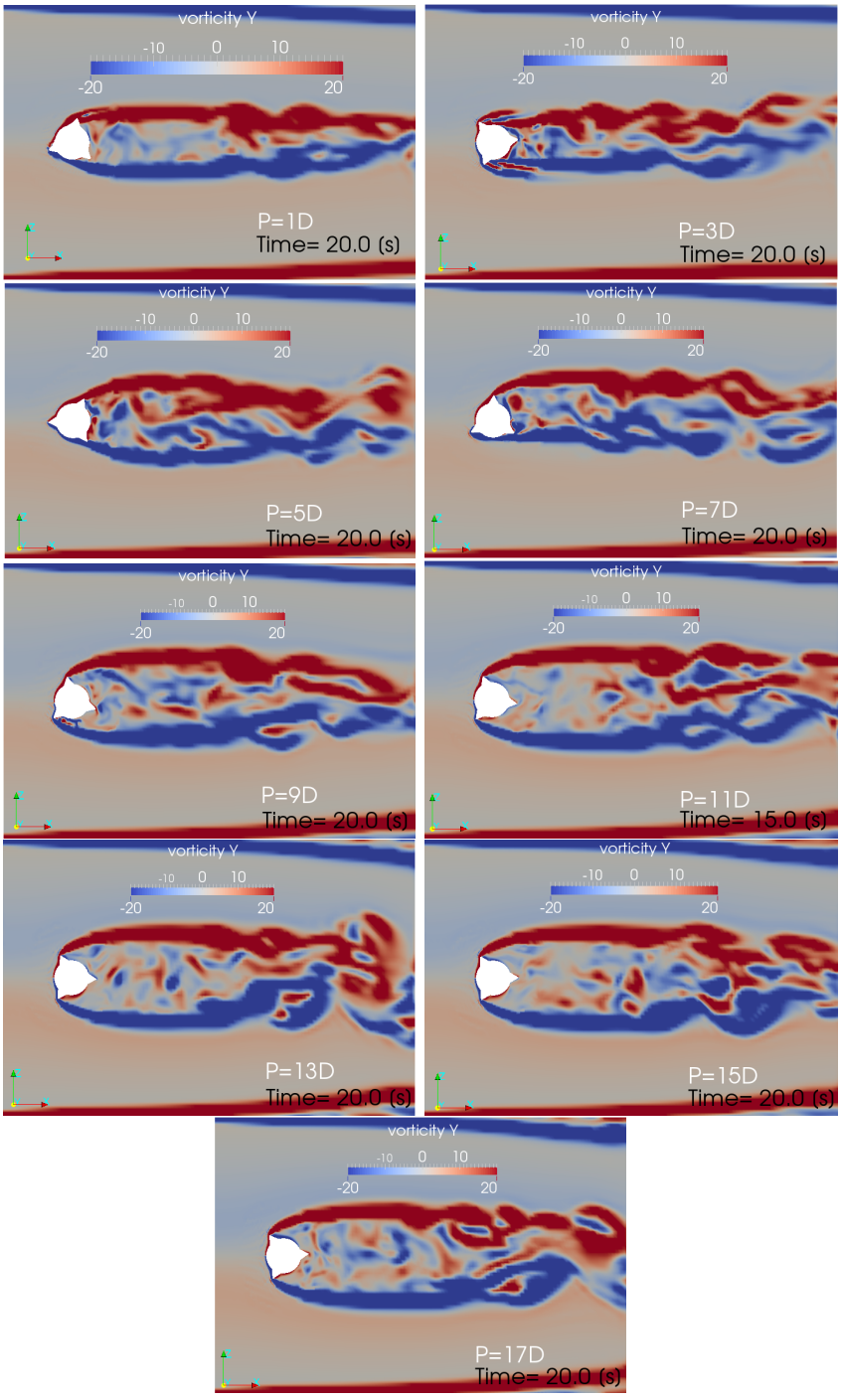

Figure 4.13: The y-vorticity contours at different stakes pitches taken at a slice on the mid point y-direction. The vorticity was calculated as the curl $\vec{\omega} = \vec{\nabla} \times \vec{u}$ of the velocity field $\vec{u}$ and defined as a measure of the amount of angular rotation of a fluid point about a particular position in a flow field.

imum y/D calculated values of both cases, it is observed that the straked shape has reduced the cross-directional vibrations by 73 percent. The plain and straked shapes gave a y/D values of 0.76 and 0.21 respectively.
The Both figures 4.4 and 4.8 shows that the vortex-shedding has been developed in a clear form behind the cylinder, which means that the strakes on the surface of the cantilever has successfully minimized the formation of vortices in down stream.
By visually comparing both figures 4.5 and 4.9, it would be observed the clear understanding of the difference between both geometries in terms of vortex shedding in down stream.
The chapter including the mentioned numerical investigations has presented a clear and simple view on vortex-induced vibrations with regarding to different geometries.
Furthermore, the presented fluid-structure interaction numerical tool has been used for both cases. The usage of the presented tool could be considered as a work of verification.
Furthermore, the effect of the pitch of strakes attached to a cylindrical obstacle, as a design parameter, was investigated. A rigid body subjected to a cross water flow has been numerically simulated. Figure 4.10 shows that effect graphically in terms of drag and lift forces. The results show that increasing the pitch value has reduced lift and increased drag. Figures 4.12 and 4.13 give a visual representation of the flow in downstream.

Chapter 5

Vortex-Induced Vibrations Suppression

The main goal of every study on a specific problem is to present a real solution. Presenting a solution should contain a testing and discussion of it. About finding a solution to the problem of vortex-induced vibrations many research works were carried out.
The foregoing chapter has discussed how the suppression of the vortex-induced vibrations can be realized by optimizing the design an shape of an obstacle. This chapter is going to present a different design of the cylindrical obstacles, by which the suppression of vortex-induced vibrations can be preformed. The presented design was tested and investigated by using the presented numerical tool.

5.1 Overview on suppression devices

The suppression of vortex-induced vibrations in offshore structures becomes an important research topic in last years. In order to to reduce the accidents, in which failure in offshore structures had been occurred due to flow-induced vibrations, the research on suppression techniques had been focused on. Under passive controlling, the vortex-induced vibrations suppression in this context may be categorized. A passive control device is defined as that device realizes the aimed controlling without giving feedback. Figure 5.1 shows different passive control devices for suppressing vortex-induced vibrations used in deep water risers.

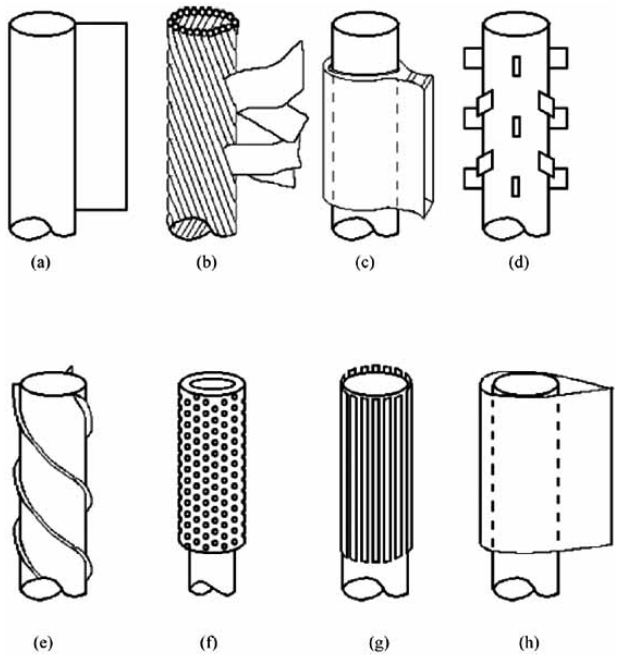

Figure 5.1: Passive control devices for suppressing VIV [78].

5.1.1 Using damping

A good way to weaken or suppress the vortex induced vibration is to damp it. In this context, Scruton number definition should be mentioned. The Scruton number is mathematically expressed as, $k_s = 2.m.\delta/\rho D^2$, where m is the mass per unit length of the structure,δ is the logarithmic decrement, ρ is the fluid density and D is the cross stream dimension of the body. Increasing Scurton number for the fluid-structure system can reduce the vibrations amplitude. If the reduced damping is greater than a value of 64, then the peak amplitudes at resonance decreases to within 1% of the cross stream dimension of the body [79]. Another type of damping is the fluid damping. The fluid damping becomes significant at low reduced velocities below 0.3 [78].

One of the most known method is modification of the material properties. By increasing the riser material strength, the so-called material internal damping becomes significant. The main goal of such technique is to avoid the

resonance under the operating conditions. The damage is often occurred, when the riser reaches its resonance. The modification of natural frequency of the riser material therefore plays the main role in this VIV suppression technique.

5.1.2 Using Geometry modification

As discussed in the previous chapters, the vortex shedding is a results of the continues flow separation points relocation. A well known type of vortex-induced vibration suppression methods is to avoid or minimize this relocation of flow separation.
This technique is usually realized by two main ways, which are modification of the outer shape of a riser to suit the flow stream lines or attaching some additional parts to it.
The most known and wide used stream-lining technique is airfoil shaped risers or in practical way adding fairings. The figure 5.1-h and 5.2 show usual and ultra-short fairings respectively.
The wide used add-on VIV suppression device is the straked shape of riser. This technique has been taken as the topic of research in the previous chapter and investigated deeply for further understanding. This common VIV suppression device is realized by attaching strakes to the riser outer surface in helical shape as shown in figure 5.1-e. The strakes have the task to disturb the formation of vortex shedding and separation points continual relocation.
Another add-on VIV suppression device is the shroud which bounded the riser from outside. As shown in figure 5.1-f the shroud add-on device is realized by bounding the riser by a holed plate of metal or another rigid material. The figure 5.3 shows the partial shroud VIV suppression device. Figure 5.1-g shows a modified shroud suppression device called *axial slats*.
Figure 5.1-a shows the wake splitter, which is another efficient way to weak VIV in the deep water risers. The design is simple and efficient, specially in low speeds water flow. In this technique, the suppression depends on the length of the tail plate.
Figure 5.1-b shows the suppression device of ribbons. In this technique, a flexible ribbons are added on the downstream side of the obstacle or riser to disturb the formation of vortex shedding. The main advantage of this design is simplicity and low cost. Figure 5.4 shows how that ribbons could be efficient in reduction of vortex shedding in the wake zone.

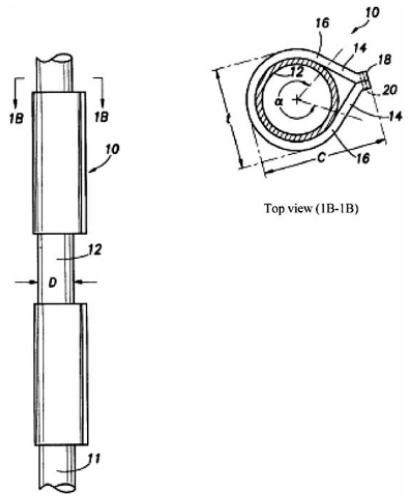

Figure 5.2: Ultra-short streamline fairing invented by D.W. Allen and D.L. Henning [80]. Part 10-fairing, 11-marine riser, 12-cylindrical marine element (D-diameter), 14-sides of fairing, 16-point of departure of fairing from the cylindrical surface,18-tail ends of fairing connected with fasteners, 20- fasteners; α-angle of fairing.

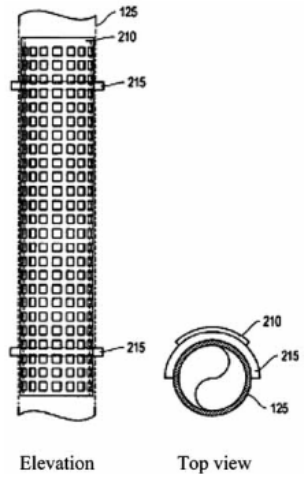

Figure 5.3: Partial shroud invented by Allen and Henning [81]. Part 125-cylindrical riser, 210- perforated partial shroud, 215-separation ring (separating shroud from riser).

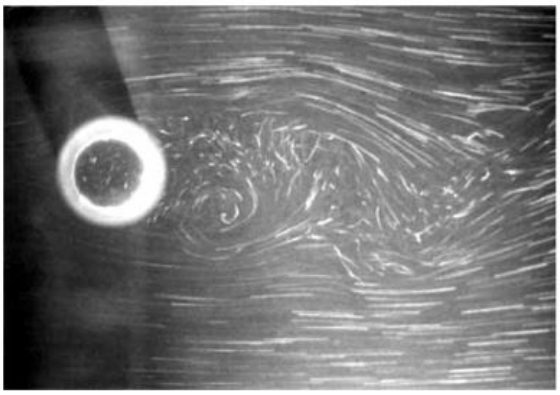

(a)

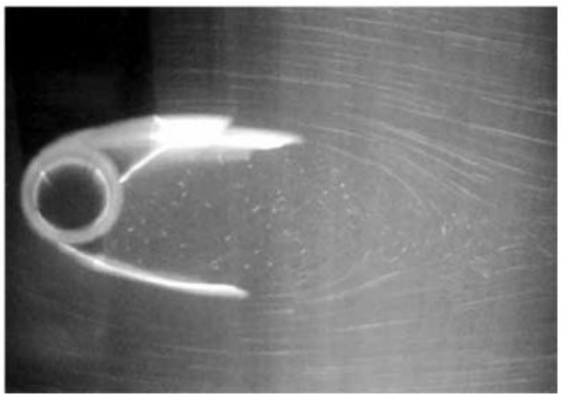

(b)

Figure 5.4: Flow field behind a cylindrical obstacle (a) without ribbon (b) with ribbons (Kwon et al [82]).

Stansby et. al [83] have found that adding spoiler on the outer surface of a deep water riser can suppress the vortex-induced vibrations by about 70%. Figure 5.1-d and 5.5 show that spoiler suppression device.
Adding guide vanes to a cylindrical obstacle in cross water flow, i.e. deep water riser, could reduce the vortex-induced vibrations. Figure 5.1-c show this technique. It is optical similar to the stream line fairing. The design of a typical guide vane would include a plate length of 1D with a lateral separation between trailing edges of 0.9D. Such guide vanes are effective in complete suppression of vortex-induced vibrations [78].

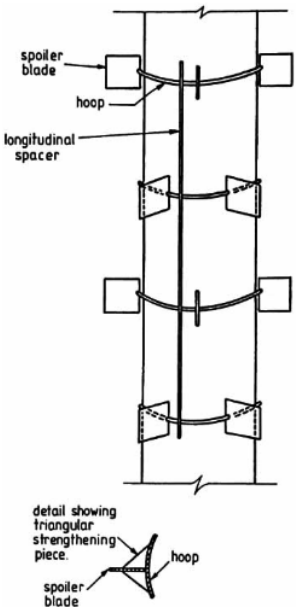

Figure 5.5: VIV Suppression device by adding spoilers [83].

5.2 An off-shore riser VIV suppression device

In this section, a new concept for the vortex-induced vibrations suppression in the off-shore risers is presented and numerically evaluated. The setup of the considered case was done depending of the experimental work of Franzini [66], which is used for validation in the foregoing chapter 3.
The concept of the mentioned device depends on attaching vortex generators on the both sides of the riser. The vortex generators are placed where the separation points are relocating. Adding such vortex generators are aiming to prevent the continues relocation of the flow separation points and hence the vortex shedding.
The following figure 5.6 shows the used concept of the presented suppression device. The showed geometry has a number of design parameter, e.g. the height of vortex generators, which had been chosen depending on the observation and analysis of the presented results of chapter 3.
The material properties of the obstacle as well as flow parameters are taken exactly as described in chapter 3 and as mentioned in the reference of Franzini [66].

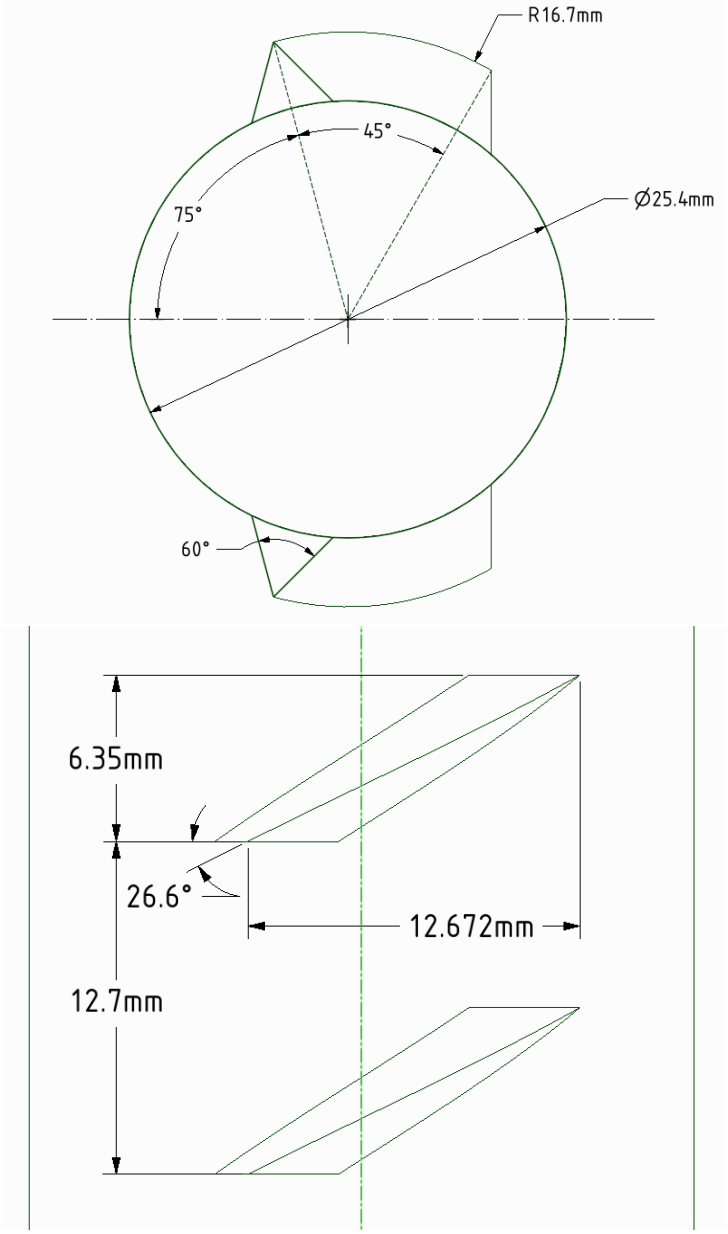

Figure 5.6: The geometry and design parameter of the presented VIV suppression device.

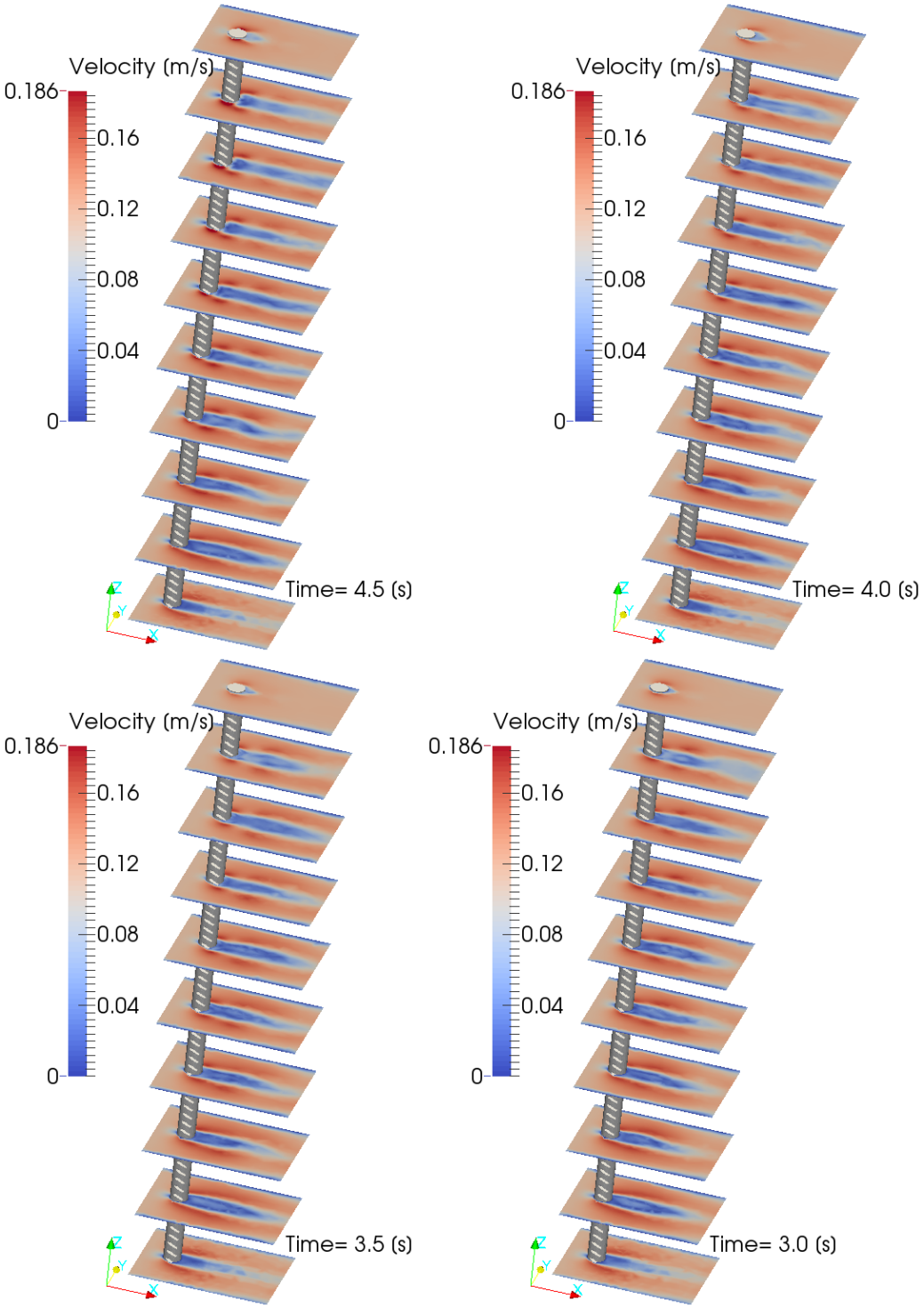

Figure 5.7: The velocity results at different sections and time steps of the presented VIV suppression device.

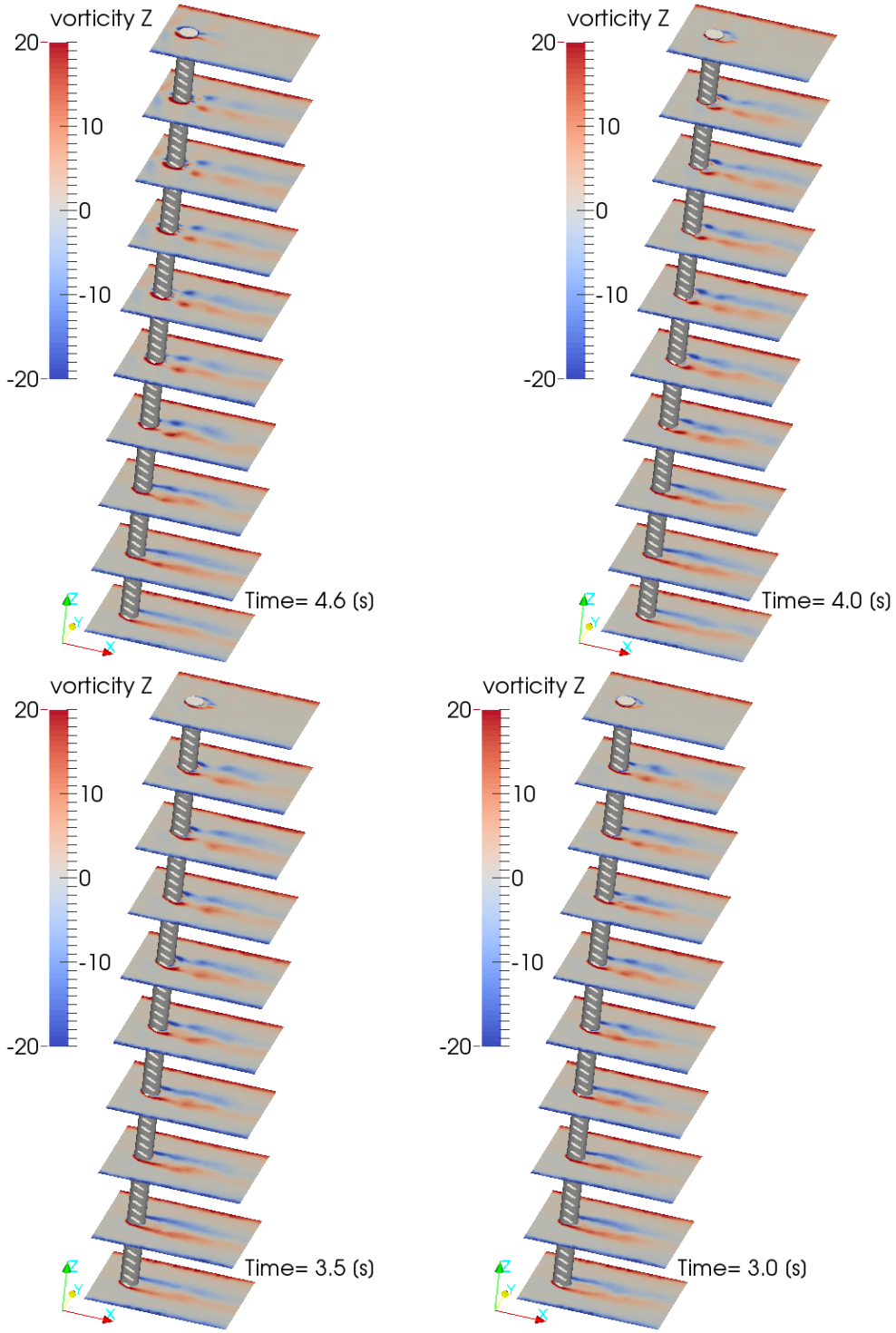

Figure 5.8: The Z-vorticity results at different sections and time steps of the presented VIV suppression device.

5.2.1 The numerical results

The presented device was investigated numerically by the OpenFOAM fluid-structure interaction solver, which was mentioned in the chapter 2. A fluid domain has been divided into 544039 tetrahedral cells. A mesh independence test has been carried out depending on the maximum value of deformation amplitude. Furthermore, the same simulation parameters, which considered in chapter 3 for the bar cylindrical obstacle validation case, have been adopted also here.
The results gave a maximum drag coefficient of 1.61, while the VIV suppression efficiency was 88.72%. The suppression efficiency *SE* can be obtained by using the equation 5.1. The value of A/D for bar obstacle has been taken from the experimental work of Franzini.

$$SE = \frac{(A/D)_{bar} - (A/D)_{modified}}{(A/D)_{bar}} \times 100\% \tag{5.1}$$

In the figures 5.7 and 5.8, the velocity and vorticity contours are given at different sections and time steps. The two mentioned figures are giving the chance for understanding the flow in down stream behind the obstacle.

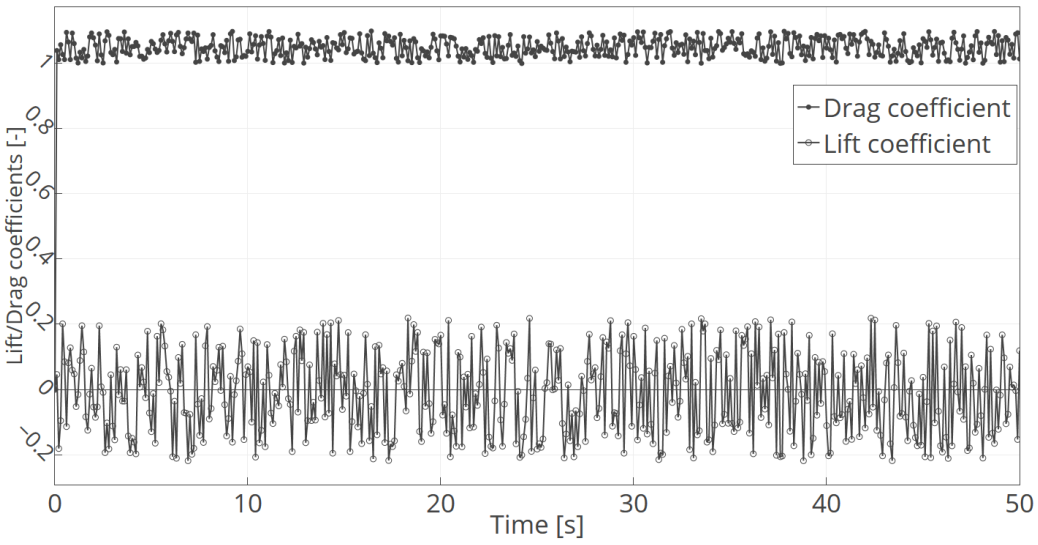

Figure 5.9: Both lift and drag coefficients time history of the presented VIV suppression device.

5.2.2 Conclusions

A VIV suppression device has been introduced. The presented design has been test using an OpenFOAM fluid-structure interaction solver, which had been presented and validated in the present dissertation.
The value of vibration amplitude has been used for the calculation of suppression efficiency, which shows a good value if compared to the published devices. The published experimental amplitude value has been considered for efficiency calculation.
Furthermore, the resulted drag coefficient of 1.05 is considered reduced value if compared to the previous published experimental value of Franzini et al[66].
As shown in both figures 5.7 and 5.8, the formation of vortex shedding has been weakened as a result of adding the side vortex generators. Furthermore, the figure 5.9 shows the time history of both lift and drag coefficients.

Chapter 6

Contributions and Future Study

The present study had paved the way for more lengthy research. This chapter presents an outlook on future research. The following sections discuss the guidelines on which future research should proceed.

6.1 Contributions

The dissertation has some contributions, which are summarized in the following points:

1. ***Design solution for suppression device of vortex-induced vibrations in deep water risers*** have been introduced and numerically investigated. Depending on what had been presented about understanding the phenomenon and coupling of numerical solvers for its numerical investigation, the solutions for suppression were the expected output of the dissertation *(chapter 5).*

2. ***Cheap and easy-to-use tool*** to solve and simulate the deepwater risers study cases under environmental conditions. The presented multiphysics numerical solver is selected to be built on OpenFOAM platform to give more availability. Since the platform used is open-source, there is a chance for future research as well as modification. The presented tool also has a wide range of usability, as it will be mentioned and explained in the following sections *(chapters 2 and 3).*

3. ***Deep understanding*** of the vortex-induced vibration phenomenon was presented with a focus on deepwater risers. The present dissertation discussed the vortex flow and its induced vibration. Through some numerical investigations, the phenomenon was discussed *(chapter 3).*

4. ***Evaluation of different turbulence models*** and discussing its effect on the vortex flow. Different numerical experiments were carried out on a fundamental case to investigate the performance of every turbulence model in order to give a clear view and to present a fair comparison of these models *(chapter 3)*

6.2 Future work

The experimental work of a fundamental case will be very helpful and valuable. The experiment should be about vibrating a cantilever in water cross-flow. The following points are suggested to be taken into account in the future study:

1. Experiment conditions are the same as the environmental conditions
2. The case is suitable for numerical simulation
3. It is precise enough to be a benchmark
4. The flow in downstream is captured
5. Other unwanted effects must be avoided because of sensitivity of vortex flow to wall effects (as discussed in chapter 1)

The experimental work will be a part from a trustable solver validation. Moreover, this kind of work with high precision is very important for understanding the phenomenon better.
Furthermore, a validation for the introduced VIV suppression device is highly recommended. Such experimental validation will play two main rolls in terms of validation of the presented solver as well as the introduced VIV suppression device.

6.2.1 Incompressible Fluid Flow Analysis

The wake of the cantilever is crucial. The flow analysis gives important information about the behavior of the experiment. Furthermore, the flow analysis is one of the front-line indications during numerical validation.
The flow is strongly recommended to be captured by a device such as PIV, which can give robust results. As mentioned in chapter 1, the PIV results are visually very similar to those numerical ones. The validation is therefore more precise.
The information and results about vortex frequency as well as its form and temporal behavior are highly recommended.

6.2.2 Fluid-structure interaction static analysis

It is axiomatic in such a field of research to observe the interaction between both solid and fluid. As discussed in the present study, the validation about this behavior could deviate and give near-to-reality results in its best case. Fair agreement could be the result of the discretization errors or other well-known numerical errors.
The observation of such behavior in experimental work should be carried out by using high-precision devices. The precision is recommended in order to avoid having an uncounted parameter, which could strongly affect the validation process.

6.2.3 Fluid-structure interaction dynamic analysis

One of the most important areas for future research is the dynamic validation. Carrying out dynamic fluid-structure interaction simulations is highly recommended to give a clear conclusion about the usability range of the presented solver.
The solver is built to be suitable for a wide range of industrial cases. The validation cases which were presented in the present dissertation are focused on the deepwater risers field. The other validation cases are therefore highly recommended.
The solver, as part of OpenFOAM platform, is very sensitive to the Courant (CFL) number, so that the implicit algorithm is used to minimize this effect and give the solver the chance to simulate at high Courant numbers. The validation of dynamic cases is recommended to achieve profound understanding

of this part as well.

6.2.4 Solver usability improvement

After the foregoing recommended validations, it may be the case that the solver will need to be improved to suit some industrial conditions which are not covered in present study. In this case, improving the solver parts and reprogramming it will be recommended.

6.2.5 Full reality validation

Simulation of a full scale deep \water riser under real industrial conditions is the main guide and best validation case. In most cases it is not possible because of a lack of facilities.
As concluded in the foregoing chapter, OpenFOAM solvers are always needed for high computational capacity. It may not be possible to achieve a full real simulation without high-performance processing clusters.

References

1. C.K. Morooka, R.I. Tsukada, "Dynamic Behavior of Pipelines and Risers Due to Vortex-Induced vibrations in time domain", 4^{th} international workshop on applied offshore hydrodynamics, 2009.

2. T. von Kármán, "Aerodynamics", McGraw-Hill, 1963.

3. W. W. Durgin, S. K. Karlsson, "On the phenomenon of vortex street breakdown", journal of fluid mechanics, vol. 48, part 3, pp. 507-527, 1971.

4. G. Diana, M. Falco, M. Gasparetto, "on vibrations due to vortex shedding induced on two cylinders with one in the wake of the other", Meccanica, 1976.

5. G. Diana, M. Falco "On the forces transmitted to a vibrating cylinder by a blowing fluid", Meccanica, 1971.

6. A. Cenedese, G. Cerri, S. Iannetta, "L.D.V. analysis of wakes behind circular cylinders and airfoils", Meccanica, 1981.

7. C. Basdevant, Y. Couder, R. Sadourny, "vortices and vortex-coupling in two dimensional turbulence", Macroscopic modelling of turbulent flows; Proceedings of the Workshop, Valbonne, France, December 10-14, 1984.

8. F.Scarano, C. Poelma," Three-dimensional vorticity patterns of cylinder wakes", Exp Fluids (2009) 47:69–83, 2009.

9. Y. Koh, "Vorticity and Viscous Dissipation in an Incompressible Flow", KSME Journal, Vol. 8, No. I, pp. 35-42, 1994.

10. J. S. Lee,"A Two-step Computational Method for the Analysis of Vortex-induced Oscillation of the Bridge", SCE Journal of Civil Engineering, Vol. 4, No. 4 / December 2000, pp, 191-199.

11. K. Skaugset, C. Larsen," Direct Numerical Simulation and Experimental Investigation on Suppression of Vortex Induced Vibrations of Circular Cylinders by Radial Water Jets", Flow, Turbulence and Combustion71:35–59, 2003.

12. D. Lucor, G. Karniadakis, "Effects of oblique inflow in vortex-induced vibrations", Flow, Turbulence and Combustion 71**:** 375–389, 2003.

13. W. Gouxing, W. Shuqing, L. Huajun, "Numerical Investigation of Vortex-induced Vibrations for Flow past a Circular Cylinder", Journal of ocean university of China, Vol.5, No.2, pp 174-180, April 2006.

14. Z. Su, Y. Liu, H. Zhang, D. Zhang, "Numerical Simulation of Vortex-induced Vibrations of a Square Cylinder," Journal of Mechanical Science and Technology 21 – 1415 ˜ 1424, 2007.

15. W. Chen, H. Li, "Vortex-induced Vibration of stay cable under profile velocity using CFD numerical simulation method", Front. Archit. Civ. Eng. China, vol. 3, pp 357 – 363, 2009.

16. F. Xu, J. Ou, Y. Xiao, "Numerical Study on Vortex Induced Vibrations of Four Cylinders in an In-Line Square Configuration", Computational structural engineering, pp. 553-567, 2009.

17. W. Ma, J. Zhang, "A Conscientious Investigation into the Effect of Re and Mass-Ratio on Two-Degree-of-Freedom Vortex-Induced Vibrations**",** China Ocean Eng.,Vol. 27, No. 4, pp. 537 – 548, 2013.

18. G. Di Silvio, F. Angrilli, A. Zanardo, "Fluid-elastic vibrations: mathematical model and experimental results", Meccanica December 1975.

19. K.G. McConnell and Y.-S. Park, "The Frequency Components of Fluid-lift Forces Acting on a Cylinder Oscillating in Still Water ", Experimental mechanics, vol. 217, 1982.

20. J. Park, K. Kwon, H. Choi, "Numerical Solutions of Flow Past a Circular Cylinder at Reynolds Numbers up to 160", KSME International Journal, Vol. 12, No. 6, pp. 1200˜ 1205, 1998.

21. M. Lee, S. Y. Lee, "Vortex-Induced Vibrations of a circular cylinder at low Reynolds Numbers", KSME International Journal, Vol. 17 No. 11, pp. 1628˜1637, 2003.

22. K. Lam, Y. F. Lin, "Drag Force Control of Flow over Wavy Cylinders at Low Reynolds Number", Journal of Mechanical Science and Technology 21, pp. 1331-1337, 2007.

23. K. Lam, L. Zou, "Experimental and Numerical Study for the Cross-flow around Four Cylinders in an In-line Square Configuration", Journal of Mechanical Science and Technology 21, pp. 1338-1343, 2007.

24. M. H. Bahmani, M. H. Akbari, "Response characteristics of a vortex-excited circular cylinder in laminar flow", Journal of Mechanical Science and Technology 25 (1), pp. 125˜133, 2011.

25. S. Kim, S. C. Lee, "Suppression of flow-induced vibration of a circular cylinder by means of a flexible sheet", Journal of Mechanical Science and Technology 26 (6), pp. 1773˜1779, 2012.

26. X. Li, G. Wang, Y. Wang, M. Jiang, X. He," Identification of Hydrodynamic Forces on a Flexible Pipe Near Plane Boundary Subjected to Vortex-Induced Vibrations", J. Shanghai Jiaotong Univ. (Sci.), 18 (1): 44-53, 2013.

27. N. G. Stocks, C. T. Shaw, G. P. King, "Low frequency instability of the Karman vortex street: An experimental study of the secondary wake instability", 2nd International Symposium on Ultrasonic Doppler Methods for Fluid Mechanics and Fluid Engineering, Paul Sherrer Institut-Switzerland, September 20-22, 1999.

28. M. Farge, R. Sandourny, "wave-vortex dynamics in rotating shallow water", Journal fluid mechanics vol. 206, pp. 433-462, 1989.

29. G. Tang, L. Lu, B. Teng, H. Park, J. Song, J. Zhang," Identification of hydrodynamic coefficients from experiment of vortex-induced vibration of slender riser model", science China, Vol.54 No.7: 1894–1905, July 2011.

30. Josefsson P M, Dalton C., "Vortex-induced vibration of a variable tension riser", Proc Int. Conf. Offshore Mech. and Archt. Eng., California, USA, pp. 215–227, 2007.

31. W. H. Xu, X. F. Gao, J. Du, "The prediction on in-line vortex-induced vibration of slender marine structures", Acta Mechanica Sinica 28 (5), pp. 1303–1308, 2012.

32. J. Liu, W. Huang, "A Nonlinear Vortex Induced Vibration Model of Marine Risers", Journal of ocean university of China 12, pp. 32-36, 2013.

33. R. A. Kumar, C. H. Sohn, B. L. Gowda," Influence of corner radius on the near wake structure of a transversely oscillating square cylinder", Journal of Mechanical Science and Technology 23, pp. 2390˜2416, 2009.

34. B. Li, Y. Liu, J. Chu, "Vortex-induced Vibration Control by Micro Actuator", Journal of Mechanical Science and Technology 21, pp. 1408-1414, 2007.

35. H. C. Chen, C. R. Chen, R. S. Mercier, "CFD simulation of risers VIV: final project report", Texas A&M University 12. 2006.

36. www.ansys.com/products/simulation+technology/fluid+dynamics/fluid+dynamics+products/ansys+cfx (access 08.01.2014)

37. openfoamwiki.net/index.php/openfoam_guide/the_piso_algorithem_in_openfoam (access 08.01.2014)

38. hpclab.iitgn.ac.in/doc/lec_starccm_foundationtrainingv2.0.pdf (access 08.01.2014)

39. M. Abdulaziz, "Analysis of the numerical fluid-structure interaction solver implemented in OpenFoam", Master thesis, University of Duisburg Essen, chair of mechatronics and robotics, 05.2012.

40. Raghavan A. Kumar, Chan-Hyun Sohn and Bangalore HL. Gowda, "Passive control of Vortex- induced vibrations: An overview." Recent Patents on Mechanical Engineering vol.1, 2008, pp. 1-11.

41. Johan Lorentzon, "Fluid-Structure Interaction (FSI) case study of a cantilever using OpenFOAM and DEAL.II with application to VIV", master thesis, 2009.

42. G.K. Batchelor, "An introduction to fluid dynamics", Cambridge University Press, 1973.

43. R. D. Blevins, "Flow Induced Vibration", 2nd Edn., Van Nostrand Reinhold Co, 1990.

44. http://hmf.enseeiht.fr/travaux/CD0102/travaux/optmfn/gpfmho/01-02/grp1/phy_know.htm (access 06.03.2015)

45. http://offshoremechanics.asmedigitalcollection.asme.org/data/Journals/JMOEEX/28394/021801_1_9.jpeg (access 06.03.2015)

46. J. J. Bertin, M. L. Smith, "Aerodynamics for Engineers" , Prentice Hall, 1989.

47. Patrik Andersson& Johan Pilqvist, "Fluid-Structure Interaction analysis of the forces causing stent graft migration", master thesis, 2011.

48. C. Habchi, S. Russeil, D. Bougeard, J. Harion, T. Lemenand, A. Ghanem, D. Valle, H. Peerhossaini, "Partitioned solver for strongly coupled fluid–structure interaction", Computers & Fluids 71 (2013) 306–319.

49. P. Sagaut, "Large Eddy Simulation for Incompressible Flows", Third Edition, Springer, 2006.

50. S. Pope, "Turbulent Flows", Cambridge University Press, 2000.

51. A. Leonard, "Energy cascade in large-eddy simulations of turbulent fluid flows". Advances in Geophysics A 18: 237–248, 1974.

52. S. Pope, "Turbulent Flows", Cambridge University Press, 2000.

53. http://www.tfd.chalmers.se/˜hani/kurser/OS_CFD_2009/FSIslides.pdf (access 06.03.2015).

54. Ž. Tukovic, H. Jasak, "Updated Lagrangian Finite Volume Solver for Large Deformation Dynamic Response of Elastic Body", Transactions of FAMENA XXX-1, 2007.

55. J. Degroote, P. Bruggeman, R. Haelterman, J. Vierendeels, "Stability of a coupling technique for partitioned solvers in FSI applications", Computers and Structures 86, pp. 2224–2234, 2008.

56. K. Wong, P. Thavornpattanapong, S. Cheung, J. Tu, "Numerical Stability of Partitioned Approach in Fluid-Structure Interaction for a Deformable Thin-Walled Vessel", Computational and Mathematical Methods in Medicine, Article ID 638519, 2013.

57. G. Becker, U. Falk, M. Schäfer, "Shape Optimization with Higher-Order Surfaces in Consideration of Fluid-Structure Interaction", Fluid-Structure Interaction. Theory, Numerics and Applications, pp. 7-20, 2008.

58. L. Piegl, "On NURBS: a Survey", IEEE Computer Graphics and Applications, Volume 11 Issue 1, pp. 55-71, January 1991.

59. Ž. Tukovic, H. Jasak, "Automatic Mesh Motion for the Unstructured Finite Volume Method", Elsevier Science, 2004.

60. R. Lohner, C. Yang, "Improved ALE mesh velocities for moving body", CommunNumer Methods Eng;12(10), pp. 599–608, 1996.

61. http://foam.sourceforge.net/docs/cpp, (access 06.03.2015).

62. Kassiotis C, Ibrahimbegovic A, Niekamp R, Matthies H., "Nonlinear fluid structure interaction problem. Part I: implicit partitioned algorithm, nonlinear stability proof and validation examples", Comput. Mech. 2011;47:305–23.

63. Vazquez J-G-V, " Nonlinear analysis of orthotropic membrane and shell structures including fluid-structure interaction" Ph.D. thesis, Escola Tecnica Superior d'Enginyers de Camins, Universitat Politecnica de Catalunya, Barcelone, Espagne, 2007.

64. Mok DP.,"Partitioniertelosungsansatze in der strukturdynamik und der fluidstruktur- interaktion", Ph.D. thesis, Universitat Stuttgart, Holzgartenstr. 16, 70174 Stuttgart; 2001.

65. Gerbeau J-F, "Vidrascu M, Frey P. Fluid–structure interaction in blood flows on geometries based on medical imaging", Comput. Struct. 2005; 83(2–3):155–65.

66. G. R. Franzini, C. P. Pesce1, R. T. Gonçalves, A. L.C. Fujarra, A. P. Pereira, "Concomitant Vortex Induced Vibration Experiments: a Cantilevered Flexible Cylinder and a Rigid Cylinder Mounted on a Leaf-spring Apparatus", Proceedings of the XIV International Symposium on Dynamic Problems of Mechanics (DINAME 2011), Brazil, March 13th - March 18th, 2011.

67. P. Pontaza, H. Chen, C. Chen," final project report: CFD Simulation of Riser VIV", MMS Project Number 481, December 2006.

68. G. Schewe, "On the Force Fluctuations Acting on a Circular Riser in Crossflow from Subcritical up to Transcritical Reynolds Number," J. Fluid Mechanics, Vol. 133, pp. 265-285, 1983.

69. E. Achenbach, "Distribution of Local Pressure and Skin Friction around a Circular Riser in Crossflow up to Re=5×10^6," J. Fluid Mechanics, Vol. 34, pp. 625-639, 1968.

70. C. Norberg, "Flow around a Circular Riser: Aspects of Fluctuating Lift," J. Fluids and Structures, Vol. 15, pp. 459-469, 2001.

71. M. A. Fernandez, "Coupling schemes for incompressible fluid-structure interaction: implicit, semi-implicit and explicit", SeMa Journal, Springer-Verlag, 2011, pp.59-108.

72. F. M. White, "Viscous fluid fow", Singapore:McGraw-Hill Book Co.,3rd ed.,2006 - ISBN 007124493-X.

73. P. Farrel, J. Maddison, "Conservative interpolation between volume meshes by local Galerkin projection", Comput. methods Appl. Mech Engrg, vol. 200, 2011, pp. 89-100.

74. Y. Xu, D. Johnston, Z. Jiao, A. Plummer, "Frequency Modeling and Solution of Fluid-Structure Interaction in Complex Pipelines", Journal of Sound and Vibration, 333 (10). pp. 2800-2822, 2014.

75. Webpage: http://foam.sourceforge.net/docs/cpp, Access 05.2012 27-Tim Behrens, "OpenFOAM's basic solvers for linear systems of equations",(2009).

76. Webpage: http://www.openfoam.com/features/linear-solvers.php, Access 05.2015

77. R. Jauregui and F. Silva, "Numerical Validation Methods", Numerical Analysis - Theory and Application, Prof. Jan Awrejcewicz (Ed.), InTech, DOI: 10.5772/23304, 2011.

78. R. Kumar, C. Sohn, B. Gowda, "Passive Control of Vortex-Induced Vibrations: An Overview", Recent Patents on Mechanical Engineering 2008, 1, 1-11.

79. Blevins, "Flow-Induced Vibration", Van Nostrand Reinhold Company, New York, 1990.

80. D.W. Allen and D.L. Henning, Patent: US20016223672B1, 2001.

81. D.W. Allen and D.L. Henning, Patent: US20046685394B1, 2004.

82. S. Kwon, J. Cho, J. Park, H. Choi, "The effects of drag reduction by ribbons attached to cylindrical pipes", Ocean Eng 2002; 29: 1945-1958.

83. P. Stansby, J. Pinchbeck, T. Henderson, "Spoilers for the suppression of vortex-induced oscillations", (Technical Note). Appl. Ocean Res. 1986; 8(3): 169-173.

CURRICULM VITAE

Der Lebenslauf ist in der Online-Version aus Gründen des Datenschutzes nicht enthalten.